

IVW - Schriftenreihe Band 164

Leibniz-Institut für Verbundwerkstoffe GmbH
Kaiserslautern

Julia Corinna Jungbluth

Analysis of the effect of selective electrochemical etching of the shape memory alloy surface on the micromechanical interfacial behavior between the shape memory alloy wire and the epoxy polymer matrix

Bibliografische Information Der Deutschen Bibliothek

Die Deutsche Bibliothek verzeichnet diese Publikation in der Deutschen Nationalbibliografie; detaillierte bibliografische Daten sind im Internet über <<http://dnb.dnb.de>> abrufbar.

Bibliographic information published by Die Deutsche Bibliothek

Die Deutsche Bibliothek lists this publication in the Deutsche Nationalbibliografie; detailed bibliographic data is available in the Internet at <<http://dnb.dnb.de>>.

Herausgeber: Leibniz-Institut für Verbundwerkstoffe GmbH
Prof. Dr.-Ing. Ulf Breuer
Erwin-Schrödinger-Straße 58
67663 Kaiserslautern
<http://www.ivw.uni-kl.de>

Verlag: Leibniz-Institut für Verbundwerkstoffe GmbH

Druck: pri-me Printservice & Medienservice
Barbarossastraße 1
67655 Kaiserslautern
D-386

© Leibniz-Institut für Verbundwerkstoffe GmbH, Kaiserslautern 2024

Alle Rechte vorbehalten, auch das des auszugsweisen Nachdrucks, der auszugsweisen oder vollständigen Wiedergabe (Photographie, Mikroskopie), der Speicherung in Datenverarbeitungsanlagen und das der Übersetzung.

Als Manuskript gedruckt. Printed in Germany.
ISSN 1615-021X
ISBN: 978-3-944440-61-3

**Analysis of the effect of selective electrochemical etching of the
shape memory alloy surface on the micromechanical interfacial
behavior between the shape memory alloy wire and the epoxy
polymer matrix**

Vom Fachbereich Maschinenbau und Verfahrenstechnik
der Rheinland-Pfälzischen Technischen Universität Kaiserslautern Landau
zur Verleihung des akademischen Grades

Doktor-Ingenieur (Dr.-Ing.)

genehmigte

Dissertation

von

Dipl.-Ing. Julia Corinna Jungbluth

geb. Vogtmann

aus Ehningen

2024

Tag der mündlichen Prüfung: 18.06.2024

Dekan	Prof. Dr. rer. nat. Roland Ulber
Vorsitzender	Prof. Dr.-Ing. Joachim Hausmann
1. Berichterstatter	Prof. Dr.-Ing. Ulf Breuer
2. Berichterstatter	Prof. Dr.-Ing. Rainer Adlung
3. Berichterstatter	PD Dr. rer. nat. habil. Martin Gurka

Vorwort

Diese Arbeit entstand im Rahmen meiner Tätigkeit als wissenschaftliche Mitarbeiterin am Leibniz-Institut für Verbundwerkstoffe GmbH (IVW), wo ich von Dezember 2018 bis Dezember 2023 im Kompetenzfeld „Tailored and Smart Composites“ tätig war. Mein besonderer Dank gilt all jenen, die mich während dieser Zeit unterstützt und so wesentlich zum Erfolg meiner Arbeit beigetragen haben.

Zuallererst möchte ich mich bei meinem Doktorvater Prof. Dr.-Ing. Ulf Breuer bedanken, für die kontinuierliche Förderung meiner wissenschaftlichen Entwicklung, sein regelmäßiges, ehrliches Feedback und das mir entgegengebrachte Vertrauen. Ebenso danke ich meinem Betreuer und Gutachter, PD Dr. rer. nat. habil. Martin Gurka, dafür, dass er mich „entdeckt“ hat, meinen Horizont mit wertvollen Anregungen erweiterte und mich stets unterstützt hat, wenn ich Hilfe benötigte. Mein Dank gilt auch Prof. Dr.-Ing. Rainer Adelung und seinem Team, deren engagierte Zusammenarbeit im Rahmen eines gemeinsamen Projekts maßgeblich zur Entstehung vieler Ergebnisse dieser Arbeit beitrug. Prof. Hausmann danke ich herzlich für die Übernahme des Prüfungsvorsitzes.

Einen wesentlichen Teil meiner Arbeit verdanke ich den Kooperationen mit unseren Projektpartnern. Besonderer Dank gilt Anna Gapeeva und Catarina Schmidt für anregende Diskussionen, spontane Unterstützung und die freundschaftliche Zusammenarbeit. Stefan Bruns danke ich für die Einführung in die Welt der Datenverarbeitung und die zuverlässige Kooperation. Mein Dank gilt auch Berit Zeller-Plumhoff, Julian Moosmann und Felix Beckmann, die mir durch ihre Unterstützung am DESY großartige wissenschaftliche Möglichkeiten eröffneten und stets für Austausch und spontane Hilfe verfügbar waren.

Herzlichen Dank an die Mitarbeiter des IVW, die mir die Arbeit stets angenehm machten und mich jederzeit unterstützten. Besonders bedanken möchte ich mich bei Benjamin Kelkel, Vitalij Popow, Bai-Cheng Jim, Andreas Klingler, Thomas Rief, Mark Kopietz, Kerstin Steidle, Sebastian Nissle, Maurice Gilberg, Max Kaiser, Manuel Kunzler, Sonja Adler, Harutyun Yagdjian, Benedikt Boos, Chris Queck, Claudius Pirro, Jan Rehra, Ilona Kunzler, Andreas Baumann, Christian Becker, Tim Schmitt, Andreas Krämer, Julian Weber, Francis Ramirez-Gonzalez, Hermann Giertzsch, Petra Volk, Ralf Schimmele, Pia Eichert, Torsten Becker, Marc Hein, Barbara Güttler,

Harald Weber, Uwe Schmitt, Silke Fischer, Regina Köhne, Ariana McCauley, Tobias Neisius, Thomas Schütz, Jörg Blaurock, Holger Mann, Joachim Stephan, Liudmyla Gryshchuk, Emmanuel Isaac Akpan, Markus Hentzel, Stefan Schmitt, Matthias Bender, Nora Feiden, Rolf Walter und Andreas Gebhard für jegliche technische, administrative und moralische Unterstützung. Ebenso danke ich meinen Hilfswissenschaftlerinnen Andrea Turizo und Vanessa Schäfer für ihre zuverlässige Unterstützung. Ich möchte mich auch bei allen Studenten bedanken, die im Rahmen ihrer studentischen Arbeiten meine Arbeit unterstützt haben.

Für das Korrekturlesen meiner Arbeit möchte ich darüber hinaus noch meinem Mann Michael, meinem Onkel Ricki und meiner Freundin Ilona danken.

Besonders möchte ich meiner gesamten Familie danken. Besonders erwähnen möchte ich meine Eltern Marika und Dieter für ihre bedingungslose Unterstützung und das Vertrauen, mich meinen eigenen Weg finden zu lassen, sowie meine Brüder Jonas und Lars.

Mein tiefster Dank gilt meinem Mann Michael: für seine Geduld, sein Verständnis, seine Unterstützung bei Korrekturen, für das Kochen in stressigen Zeiten und dafür, dass er nie an mir zweifelte – selbst wenn ich es tat. Und meinem Sohn Jonah, der unser Leben bereichert, mir jeden Tag vor Augen führt, was wirklich wichtig ist, und durch seine Gelassenheit dazu beigetragen hat, dass ich mich in Ruhe auf meine Prüfungen vorbereiten konnte.

Die Zeit am IVW hat meinen Horizont erweitert, zu neuen Freundschaften geführt und wird immer einen besonderen Platz in meiner Erinnerung einnehmen.

Table of Contents

Vorwort	I
Table of Contents	III
Abstract	VIII
Kurzfassung	IX
Deutsche Zusammenfassung	X
Nomenclature	XIV
1 Introduction	1
2 Fundamentals	3
2.1 Shape Memory Alloys	3
2.2 Analysis and Description of Interfaces in FRP Composites	5
2.3 X-ray Microcomputed Tomography for Composite Materials	9
2.4 X-ray <i>in situ</i> Analyzing the Interfacial Failure Process in FRP Composite.....	10
3 State of the art	12
3.1 Thermomechanical Characterization of Non-Embedded SMA Wires.....	12
3.2 Shape Memory Alloy Hybrid Composite	13
3.3 Interface Strength Improvement Techniques in SMAHC	14
3.4 Measurement and Description of Interface Strength in SMAHC	17
3.5 Current Understanding of the Interfacial Failure Process in SMAHC During Pull-Out Test Gained by Incorporating Optical Methods.....	22
3.6 Summary of the Gaps in the State of the Art of Characterization and Improvement of the Interfacial Strength between SMA wire and Polymer Matrix	25
4 Aims and Solution Strategy	27
5 Materials & Sample Preparation	31

5.1	Polymer Matrix	31
5.2	SMA Wire	32
5.2.1	Selective Electrochemical Etching	32
5.3	Pull-Out Test Sample Manufacturing	36
5.3.1	Manufacturing Process for Mechanical Laboratory Pull-Out Test Sample	37
5.3.2	Manufacturing Process for <i>In Situ</i> Pull-Out Test Sample	38
6	Methods of Laboratory and Analytical Measurements	40
6.1	Understanding the Influence of the SMA Wire Surface Selective Electrochemical Etching Process on the Thermomechanical SMA Wire Characteristics and the Applied Surface Morphology	40
6.1.1	Stress-Strain Analysis	41
6.1.2	Actuator Characterization Set Up	41
6.1.3	Dynamic-Mechanical-Thermal Analysis	42
6.1.4	Scanning Electron Microscope	43
6.1.5	X-ray Microcomputed Tomography	43
6.1.6	Rendering of Surface Area and Pit Morphology	44
6.2	Understanding the Influence of the SMA Wire Surface Morphology on the Force Transfer between SMA Wire and Polymer Matrix	46
6.2.1	Mechanical Laboratory Pull-Out Test	47
6.2.2	Stress Optics	47
6.2.3	Model Description of the Force Transfer by Using Greszczuk	50
6.2.4	Analysis of the Surface-Dependent Stress Needed for Failure in the Interface between SMA Wire and Polymer Matrix	51
6.3	Understanding the Interfacial Failure Behavior of an SMAHC during Pull-Out Test and the Influence of the Thermomechanical Clamping due to Embedding the SMA Wire	53
6.3.1	<i>In Situ</i> Pull-Out Test	53

6.3.2 X-ray μ CT <i>In Situ</i> Straining of the Non-Embedded SMA Wire with Structured Surface.....	55
6.3.3 Digital Volume Correlation for Strain Analysis of the μ CT <i>In Situ</i> Data	55
6.3.4 Segmentation	57
7 Results.....	60
7.1 Characterization of the Thermomechanical Characteristics of the SMA Wire and SMA Wire Surface Morphology Description before and after Selective Electrochemical Etching Process	60
7.1.1 SMA Wire with a Nominal Diameter of 1 mm.....	60
7.1.2 SMA Wire with a Nominal Diameter of 0.5 mm	66
7.1.3 Discussion of the Influence of the SMA Wire Surface Modification to the Non-Embedded SMA Wire Thermomechanical Characteristic Behavior.....	69
7.2 Characterization of the Influence of the SMA Wire Surface Morphology on the Force Transfer between SMA Wire and Polymer Matrix	71
7.2.1 SMA Wire with a Nominal Diameter of 1 mm.....	71
7.2.2 SMA wire with a Nominal Diameter of 0.5 mm	76
7.2.3 Discussion of the Influence of the SMA Wire Surface Morphology on the Force Transfer between SMA Wire and Polymer Matrix	80
7.3 Characterization of the Interfacial Failure Behavior of an SMAHC during Pull-Out Test and the Influence of the Thermomechanical Clamping due to Embedding the SMA Wire.....	83
7.3.1 SMA Wire with a Nominal Diameter of 0.5 mm	83
7.3.2 Discussion of the Findings by Micromechanical Analysis of the Force Transfer between SMA Wire with Surface Modifications and Polymer Matrix and the Influence of the Thermomechanical Clamping of the SMA Wire due to Embedding	92
8 Summarized Consideration.....	97

9 Conclusion & Outlook	102
References	106
Appendix.....	118
A.1 Reproducibility Test Selective Electrochemical Etching, for Structure B1	118
A.2 Quality Assurance Measurements	120
A.2.1 Pull-Out Sample Quality Control	120
A.2.2 X-ray Beam-Induced Post Curing Effects of the Polymer Matrix During μ CT Measurements	121
A.2.3 Testing the Bond Quality Between SMA Wire and Polymer Matrix by Ion-Beam Polishing of Cross-Section of a μ CT <i>In Situ</i> Pull-Out Sample	122
A.3 <i>In Situ</i> Pull-Out Sample Manufacturing	123
A.4 Separation of SMA Wire Surface Pits (μ CT Analysis)	123
A.5 Stepwise Increasing of Load During μ CT <i>In Situ</i> Pull-Out and Straining Test	125
A.6 Segmentation of Structure S1 μ CT <i>In Situ</i> Pull-Out Test	127
A.7 Comparison of the Global Axial and Radial Strain Development by Increasing Load for the <i>In Situ</i> Pull-Out and Strain Test for One Representative Sample for (Structure S1, S2 (Embedded) and Structure S1 (Non-Embedded))	127
A.8 Force-Time Curve During μ Ct <i>In Situ</i> Pull-Out Test.....	128
A.9 Values Used for Calculating the Interfacial Shear Stress	129
A.10 Propagation of the Interfacial Failure Observed for a μ CT <i>In Situ</i> Pull-Out Tested Sample with Structure S2.....	130
A.11 Influence of the Polymer Matrix Geometry to the Calculated Interfacial Shear Strength of the Pull-Out Test According to [50].....	131
A.12 Pre-Strain Test Mean Values with Confidence Interval for SMA Wire with a Nominal Diameter of 1 mm	131

Own Publication.....	132
Student Thesis	134
Curriculum Vitae	135

Abstract

This research investigates the force transfer mechanisms in active shape memory alloy hybrid composites (SMAHC), specifically focusing on the interface between the surfaces of selectively electrochemical structured nickel titanium (NiTi) shape memory alloy (SMA) wires and the surrounding epoxy polymer matrix. A novel approach that combines optical methods such as stress optics, synchrotron X-ray microcomputed tomography (μ CT) and scanning electron microscopy (SEM) with mechanical pull-out tests to quantitatively assess and observe the force transfer capability of surface structured SMA wires in SMAHC is developed and analyzed. Interface adhesion strength is crucial for the performance of SMAHC. Selective electrochemical etching of a one-way effect NiTi SMA wire enhances its adhesion to the polymer matrix, resulting in a significant increase in the force of the first (max. 3.3 times) and the complete interface failure compared to the as-delivered SMA wire during pull-out tests. The selective electrochemical etching process does not significantly influence the SMA wires' thermomechanical performance. This research also discusses the etching pit formation and distribution impacts on the resulting improvement of force transfer. High resolution μ CT *in situ* pull-out tests show the volume progression of interfacial failure, using digital volume correlation to relate the radial and axial strains of the structured SMA wire to the force of the first interfacial failure. This research highlights the complex mechanical interactions during the pull-out tests, which are influenced not only by shear stresses but also by normal stresses from the contraction of the SMA wire and external stresses from the polymer matrix.

Kurzfassung

In dieser Forschungsarbeit werden die Mechanismen der Kraftübertragung in aktiven Formgedächtnislegierungs-Hybridverbundwerkstoffen (engl. SMAHC) untersucht, wobei der Schwerpunkt auf der Schnittstelle zwischen der Oberfläche von selektiv elektrochemisch strukturierten Nickel Titan (NiTi)-Formgedächtnislegierungsdrähten (FGL engl. SMA) und der umgebenden Epoxid-Matrix liegt. Ein neuartiger Ansatz, der optische Methoden wie Spannungsoptik, Synchrotron-Röntgenmikrocomputertomographie (μ CT) und Rasterelektronenmikroskopie (SEM) mit mechanischen pull-out Versuchen kombiniert, um die Kraftübertragungsfähigkeit von oberflächenstrukturierten FGL-Drähten in SMAHC quantitativ zu bewerten, wird untersucht. Die Grenzflächenhaftung ist entscheidend für die Leistungsfähigkeit von SMAHC. Das selektive elektrochemische Ätzen eines FGL-Drahtes mit Einweg-Effekt verbessert die Kraftübertragung zur umhüllenden Polymermatrix, was zu einer signifikanten Erhöhung der Kraft des ersten (3,3-fach) und des vollständigen Versagens der Grenzfläche im Vergleich zum FGL-Draht im Lieferzustand während der pull-out Versuche führt. Die thermomechanische Charakteristik der FGL-Drähte wird durch den selektiven elektrochemischen Ätzprozess nicht wesentlich beeinflusst. In dieser Studie wird auch der Einfluss der Ätzgrubenbildung und deren Verteilung auf die resultierende Verbesserung der Kraftübertragung diskutiert. Hochauflösende μ CT *in situ* pull-out Versuche zeigen den Verlauf des Grenzflächenversagens über das Volumen, wobei digitale Volumenkorrelation verwendet wird, um die radiale und axiale Dehnungen des FGL-Drahts mit der Kraft des ersten Grenzflächenversagens in Beziehung zu setzen. Diese Forschungsarbeit verdeutlicht die komplexen mechanischen Wechselwirkungen während der pull-out Versuche, die nicht nur durch Schubspannungen, sondern auch durch Normalspannungen, entstehend aus der Kontraktion des FGL-Drahtes und externen Spannungen durch die Einbettung des FGL-Drahtes in eine Polymer Matrix beeinflusst werden.

Deutsche Zusammenfassung

Intelligente Hybrid-Verbunde bestehend aus Formgedächtnislegierungen (FGL) eingebettet in Faser-Kunststoff-Verbunde (FKV) sind eine neue Werkstoffklasse mit individuell ausrichtbaren Eigenschaften gepaart mit intrinsischem Funktionalismus. Bei dieser Werkstoffklasse wird eine Synergie gebildet aus den positiven Eigenschaften von FKV, wie einer hohen spezifischen Steifigkeit, anisotrop einstellbaren Eigenschaften und dem hohen Leichtbaupotential, mit den einzigartigen Eigenschaften von Formgedächtnislegierungen, die thermische in kinetische Energie umwandeln können, dem sogenannten Formgedächtniseffekt. Die Kombination dieser beiden Materialien resultiert in einem einzigartigen Eigenschaftsprofil, das für verschiedene Anwendungsbereiche, beispielsweise als Aktuator, morphender Oberfläche oder in der Sensorik interessant ist.

In dieser Arbeit ist der sogenannte Ein-Weg-Effekt des FGL-Drahtes von Interesse. Wenn eine FGL durch eine externe Kraft verformt wird, kehrt diese in ihre ursprüngliche Form zurück, wenn eine Temperatur auf die FGL wirkt, die größer ist als eine materialabhängige Umwandlungstemperatur. Diese Formänderung ist reversibel und kann nach einer induzierten Verformung beliebig oft abgerufen werden. Wird eine FGL, in dieser Arbeit in Drahtform, in einen steifen, dünnen FKV mit einem Abstand zur neutralen Faser des FKV eingebracht, so kann durch diesen Effekt eine Formänderung in Form einer Biegung induziert werden. Damit können Biege-Aktuatoren gebaut werden, die über eine hohe Energiedichte verfügen und keinen zusätzlichen Motor benötigen.

Damit Anwendungen wie diese möglich werden, ist die Kraftübertragung zwischen dem eingebetteten FGL-Draht und der umhüllenden Matrix von besonderer Bedeutung. Nur solange die durch den Formgedächtniseffekt induzierten Spannungen und Dehnungen über die Grenzfläche von dem FGL-Draht in die Polymer Matrix übertragen werden können, zeigt der Hybrid-Verbund den beschriebenen Funktionalismus. Um diese Kraftübertragung zu verbessern und eine Beständigkeit der Verbindung zu gewährleisten, gibt es verschiedene Ansätze. Diese reichen von zusätzlich eingebrachten Krafteinleitungselementen über die Modifikation der FGL-Drahtoberfläche bis zur Modifikation der Polymer Matrix. In dieser Arbeit steht die volle Integration des FGL-Drahtes in die Polymer Matrix mit einer Modifikation der FGL-Drahtoberfläche im

Vordergrund, ohne dass zusätzliche Kraffteinleitungselemente eingebracht werden müssen.

Dafür wird in dieser Arbeit die FGL-Drahtoberfläche mittels selektivem elektrochemischen Ätzen makroskopisch gesehen über die gesamte Drahtlänge homogen und reproduzierbar strukturiert. Dieses bereits an anderen Werkstoffen erprobte Oberflächenbehandlungsverfahren wurde zum ersten Mal für NiTi FGL-Drähte verwendet. Dadurch werden teilweise omegaförmige Hinterschneidungen und Löcher in die FGL-Drahtoberfläche geätzt, welche die Gesamtoberfläche vergrößern und in einer mechanischen Verhakung zwischen der Polymer Matrix und dem FGL-Draht resultieren. Durch die Ätzparameter kann die Ausprägung der Oberflächenmorphologie gezielt beeinflusst werden. In dieser Arbeit wurden zwei Drahtdurchmesser (0.5 und 1 mm) desselben Drahttyps untersucht. Für den FGL-Draht mit 1 mm wurden drei verschiedene geätzte FGL-Drähte und für den FGL-Draht mit 0.5 mm wurden zwei verschiedene geätzte Drahtmorphologien analysiert. Der Ansatz, die Kraftübertragung mittels faserseitiger Modifikation zu optimieren, wird im Stand der Technik häufiger genutzt. Allerdings wird der Einfluss der Oberflächenbehandlung auf die charakteristischen Eigenschaften des FGL-Drahtes kaum untersucht und die Analyse der neu entstehenden Oberflächenmorphologie wird häufig nur qualitativ für einen kleinen Auswertebereich durchgeführt. In dieser Arbeit wird das selektive Ätzverfahren auf seine Eignung geprüft, die Drahtoberfläche makroskopisch homogen zu ätzen, ohne die thermomechanische Charakteristik des FGL-Drahtes zu beeinflussen. Dafür wurden die oberflächenstrukturierten FGL-Drähte mit den unbehandelten FGL-Drähten in einem Zugversuch, einem speziell entwickelten Aktuatorik-Prüfstand und mit der dynamisch-mechanisch-thermischen Analyse bezüglich der charakteristischen thermomechanischen Eigenschaften analysiert. Die entstehende FGL-Drahtoberflächenmorphologie wurde mittels Rasterelektronenmikroskop (REM) und Synchrotron-Röntgenmikrocomputertomographie (μ CT) untersucht und quantifiziert. Es konnte kein Einfluss des selektiven Ätzverfahrens auf die thermomechanischen Eigenschaften des FGL-Drahtes gemessen werden. Die quantitative Beschreibung der Drahtoberfläche kann genutzt werden, um die aufgebrachten Oberflächenmorphologien von einander abzugrenzen und mit weiteren Messwerten zu korrelieren.

Um die Auswirkungen der Oberflächenbehandlung des FGL-Drahtes auf die Kraftübertragung zu messen, wurde der pull-out Versuch als in der Literatur etablierter Versuch identifiziert und in dieser Arbeit angewendet. Bei diesem mikromechanischen Test wird

ein FGL-Draht in eine Polymer Matrix eingebettet und aus dieser herausgezogen. Die Kraft wird dabei direkt in den FGL-Draht appliziert. Der Versagensfortschritt in der Grenzfläche wurde mittels Spannungsoptik beobachtet. Durch dieses optische Verfahren kann der Auf- und Abbau von Spannungen in der Probe visualisiert werden, jedoch können diese nicht weiter quantifiziert werden. Um den Einfluss der Ausprägung der Oberflächenmorphologie auf die Kraftübertragung zu überprüfen, wurden die bereits beschriebenen verschiedenen FGL-Drahtoberflächenmorphologien miteinander und mit der unbehandelten FGL-Drahtoberfläche verglichen. Dabei zeigte sich, dass der strukturierte FGL-Draht eine Erhöhung der Kraftübertragung von maximal dem 3,3-fachen im Vergleich zum FGL-Draht im Anlieferungszustand erzielt hat (abhängig von der aufgetragenen Oberflächenmorphologie). Mittels μ CT-Analyse wurde eine Vergrößerung der FGL-Drahtoberfläche um den Faktor 1,5 ermittelt. Allgemein zeigte sich, dass durch die Oberflächenstrukturierung nicht nur die Kraft des Erstversagens, sondern darüber hinaus auch die Kraftübertragung bis zum kompletten Versagen der Grenzfläche verbessert werden konnte. Durch das Einführen eines eigens definierten Parameters der oberflächenabhängigen Spannungen konnten die Ergebnisse der beiden verschiedenen FGL-Drahtdurchmesser miteinander verglichen und in Beziehung gesetzt werden. Dabei konnte gezeigt werden, dass eine Oberflächenmorphologie angestrebt werden sollte, in welcher relativ kleine Oberflächenlöcher möglichst gleichmäßig dicht verteilt werden, um eine maximale Kraftübertragung zu generieren.

Zu den pull-out Versuchen mit Spannungsoptik wurden Laststeigerungs-pull-out Versuche, die *in situ* mittels μ CT-Analyse beobachtet wurden mit dem Ziel durchgeführt, das Grenzflächenversagen im Volumen für einen definierten Bereich hochaufgelöst zu beobachten. Der Grund für das Versagen der Grenzfläche zwischen FGL-Draht und Polymer Matrix wird in der Literatur viel diskutiert. Allerdings ist nicht bekannt, welche Auswirkungen das Einbetten des FGL-Drahtes in eine Polymer Matrix und der damit verbundenen Applizierung einer äußeren Spannung auf den FGL-Draht auf das thermomechanische Verhalten des FGL-Drahtes hat. Durch den *in situ* pull-out Versuch können solche Fragestellungen näher betrachtet werden. Die applizierte FGL-Drahtoberflächenmorphologie kann dabei als so genanntes Speckle Muster genutzt werden, um mittels digitaler Volumen-Korrelations-Analyse die während des Versuchs aufgetragenen axialen und radialen Dehnungen zu messen. Dadurch kann erstmals für einen bestimmten Volumenbereich die axiale (in z-(Last) Richtung) und radiale (Kontraktion des FGL-Drahtes) Dehnung des eingebetteten FGL-Drahtes erfasst und

quantifiziert werden. Der Versuch zeigt, dass Dehnungen im Bereich der Bruchdehnung der Polymer Matrix erreicht werden, die einen Einfluss auf das Versagen haben können. Außerdem zeigt der Versuch, dass die Querkontraktion des FGL-Drahtes einen Einfluss auf den Versagensprozess haben kann. Der Vergleich von FGL-Drähten mit verschiedenen Oberflächenmorphologien zeigt, dass die Ausprägung der FGL-Drahtoberflächenmorphologie mikromechanisch betrachtet einen Einfluss auf das Grenzflächenversagen hat. Außerdem konnte gezeigt werden, dass die umhüllende Polymer Matrix die Querkontraktion des FGL-Drahtes bis zu einem bestimmten Punkt behindert.

Zusammenfassend zeigt diese Arbeit, dass selektives elektrochemisches Ätzen ein vielversprechendes Verfahren ist, um die Grenzflächenfestigkeit zwischen FGL-Draht und Polymer Matrix zu verbessern. Durch die Strukturierung kann ein mechanischer Formschluss erzielt werden, welcher in einem überlagerten adhäsiven und kohäsiven Versagensverhalten resultiert und die Kraftübertragung in der Grenzfläche optimiert. Diese Arbeit zeigt darüber hinaus das Potential der Korrelation von optischen Analysemethoden mit mechanischen Prüfverfahren. Das im pull-out Versuch beobachtete Grenzflächenversagensverhalten zwischen FGL-Draht und Polymer Matrix ist kein reines Schubversagen, sondern wird durch die charakteristischen Eigenschaften des FGL-Drahtes und Normalspannungen überlagert, wodurch sich ein komplexer Spannungszustand in der Grenzfläche ergibt. Der Aufbau eines tieferen Verständnisses für die Grenzflächenversagensmechanismen bildet die Basis für eine Optimierung der Grenzflächenfestigkeit, was in einer Optimierung von Hybriden-Verbunden resultiert.

Nomenclature

Abbreviations

AFM	A tomic force m icroscope
CE	C ounter e lectrode
DC	D irect c urrent
DESY	D eutsches- E lektronen S ynchrotron
DMA	D ynamic m echanical a nalysis
DMTA	D ynamic m echanical t emperature a nalysis
DIC	D igital i mage c orrelation
DSC	D ifferential s canning c alometry
DVC	D igital v olume c orrelation
EDS	E nergy d ispersive X-ray s pectroscopy
FoV	F ield o f V iew
FRP	F iber reinforced p lastic
HC	H ybrid composite
I/W	Leibniz-Institut für V erbund w erkstoffe GmbH
MEMS	M icro- e lectromechanical s ystems
Ni	N ickel
PEEK	P olyetheretherketone
PMMA	P olymethylmethacrylate
PU	P olyurethane
ROI	R egion o f interest
RT	R oom t emperature
SEM	S canning e lectron m icroscope
SMA	S hape m emory a lloy
SMAHC	S hape m emory a lloy h ybrid c omposite

SME	S hape m emory e ffect
SLA	S tereolithography
Ti	T itanium
TMA	T hermo m echanical a nalysis
WE	W orking e lectrode
XPS	X -ray p hotoelectron s pectroscopy
XRD	X -ray d iffraction
μCT	M icro c omputed t omography
2D	T wo D imensional
3D	T hree D imensional

Indices

<i>a</i>	Mean
<i>e</i>	Embedded
<i>f</i>	Finish
<i>m</i>	Matrix
<i>shear</i>	Shear
<i>rad</i>	Radial
<i>w</i>	Wire
<i>yield</i>	Yield
<i>zz</i>	Axial

Coordinate systems

<i>r, y, z</i>	Global coordinate system
----------------	--------------------------

Formula symbols		Dimensions
A	Austenite	°C
D	Radius polymer matrix	mm
F	Force	N
G	Shear modulus	MPa, GPa
σ	Stress	MPa
ε	Strain	-, %
L	Length	mm
M	Martensite	°C
R	Roughness	μm
r	Radius	mm
α	Material-dependent variable	$\frac{1}{\text{mm}}$

1 Introduction

The increasing demand for materials with improved properties concerning weight, flexibility, strength and multifunctionality has accelerated the research for innovative material solutions. These evolving material requirements, combined with the need for greater efficiency and sustainability, have led to a global change in perspective. One solution for addressing this challenge are so-called smart materials, in which the associated materials have multifunctional properties. [1, 2] Among these smart materials, shape memory alloys (SMA) can respond to external thermal stimuli by converting thermal into kinetic energy [3]. Combining the intrinsic function of SMA with the tailored properties of fiber-reinforced plastics (FRP) results in a multifunctional, stiff, strong and durable material whose properties can be adjusted by design [4]. Integrating SMAs in FRP, often in wire shape with an offset to the neutral axis of the thin, stiff composite structure, creates a new material category: the shape memory alloy hybrid composite (SMAHC). An SMAHC actuator can undergo a tailored shape change due to a thermal field applied to the incorporated SMA wires. [5] Avoiding the need for additional mechanical actuation makes an SMAHC very interesting for actuator applications in the aerospace [6] and automotive [7] industries since considerable savings in weight, space and costs can be achieved. For instance, integrating SMAs into FRPs results in new applications such as vortex generators, winglets, or wing airfoils. In the example of the vortex generators, the FRP is the tailored antagonistic partner, and the SMA wire is the induced agonist. [8]

In order to realize the intended functionality of SMAHC, it is essential to create efficient force transfer mechanisms between the embedded SMA wire and the surrounding polymer matrix across the interface [9]. When external thermal energy, such as joule heating, activates the SMA wire, it induces intrinsic strains and stresses within the SMA wire, which must then be effectively transferred through the interface into the surrounding polymer matrix and throughout the FRP structure [10]. In SMAHC, therefore, the interface is thermomechanically highly stressed. Consequently, the interface becomes the performance-limiting factor, underlining the need to characterize and optimize its performance for the durability and functionality of an SMAHC.

Numerous researchers focus on improving and characterizing the interface between SMA materials and polymer matrices [10, 11]. There are three main approaches to

improve the interface strength: modification of the SMA wire [10], modification of the polymer matrix [12] or introduction of force-transmitting elements [13] between them. The ultimate objective to which this research should contribute is to integrate an SMA wire into a composite material by selective electrochemical etching of the SMA wire surface in order to achieve robust interfacial strength, thereby eliminating the need for additional force transmission mechanisms. Due to the highly localized pseudoplastic deformation that the SMA wire undergoes when exposed to external loads [3], it remains unclear whether the SMA wire-polymer interface failure in an SMAHC is primarily stress-induced or strain-induced [14]. Therefore, a comprehensive investigation to optimize the interfacial strength is performed in this research. Essential steps towards fully integrated SMAHCs are the mechanical characterization of the interfacial strength as the basis for its improvement and a better understanding of the interaction between SMA wire and the envelope polymer matrix using pull-out tests combined with optical methods, such as SEM, μ CT and stress optics. Thus, the research goes beyond the simple optimization of the interfacial strength and includes a comprehensive understanding of the material interactions and the analysis of the interfacial failure progression [11].

In other words, characterizing the interfacial strength in SMAHC, increasing it, and building an understanding of the interaction between the SMA and the envelope polymer matrix are essential steps towards developing fully integrated SMAHCs and are thus the overall objective of this research. Section 2 gives an overview of basic measurement techniques as a basis for a better understanding of the research. The state of the art and open gaps described in section 3 will be addressed by the research strategy presented in section 4. The applied measurements, experiments and analysis resulting from the research strategy are discussed in detail in sections 5 and 6. The results of this research are finally summarized in section 7.

2 Fundamentals

2.1 Shape Memory Alloys

The relevance of SMA for technical applications was discovered in 1963 with research on NiTi-based alloys [3]. Since then, their technical relevance increased, and numerous research papers have been published [15]. Nowadays, SMA materials are relevant in the research for various technical fields such as mini actuators and micro-electro-mechanical systems (MEMS) [16, 17, 18], robotics [19, 20], automotive [7], aerospace [6, 21], and biomedicine [17, 22]. Nevertheless, only a limited amount of industrial applications, such as eyeglass frames [23] and stents [24], are known yet. Compared to other actuation technologies, such as piezoceramics, SMAs exhibit an outstanding volumetric energy density, defined as work output per unit volume [3]. They can provide actuation stresses up to 700 MPa [3] accompanied by large recoverable strains up to 8 % [15], with the only limitation being the operating frequency (1-10 Hz) [25]. Due to their high actuation energy density (approx. 10^3 J/kg), they can also respond mechanically to thermal stimulation when a large external load is applied [3].

SMA materials are so-called because of their intrinsic ability to convert thermally applied energy into mechanical energy using a solid-solid phase transformation. This phase transformation results in a reversible, hysteretic shape change. It occurs between the low-temperature phase martensite (tetragonal, orthorhombic, or monocline) and the high-energy phase austenite (cubic), accompanied by twinning processes. [3, 26]

The austenite phase is characterized by a high degree of symmetry and is commonly referred to as the parent phase, while the martensite has a less symmetric crystal structure [4]. During the phase transformation, the original atomic lattice is deformed by the enlargement and reduction of lattice axes. The neighboring atoms remain adjacent to each other, making this phase transformation reversible. The modification in the lattice structure alters the packing density between martensite (68 %) and austenite (74 %), resulting in a volume change during the phase transformation. Furthermore, distinctions in the mechanical properties, such as Poisson's ratio and Young's modulus, are observed between the austenite and martensite phases. [3, 27]

The martensite phase has two orientation direction variants: twinned and detwinned martensite [3]. In summary, SMA materials, categorized as multifunctional materials, can return to their first state after a pseudo-plastic deformation by applying thermal energy [3, 15]. This phenomenon, called the shape memory effect (SME), forms the foundation for the previously described applications. Therefore, the SME for the so-called one-way effect SMA wire is described below. Notably, SMA materials can exhibit a two-way effect or superelastic behavior. The two-way effect refers to the direct, intrinsic trained phase transformation between martensite and austenite without needing an external force. [3] However, these effects are omitted, as they are not relevant to the scope of this research.

For stress-free SMA materials, four characteristic phase transformation temperatures are decisive for the phase transformation described: martensite finish temperature (M_f), martensite start temperature (M_s), austenite start temperature (A_s) and austenite finish temperature (A_f). The unique stress-strain-temperature characteristics of one-way SMAs are shown in Figure 1. [3, 28]

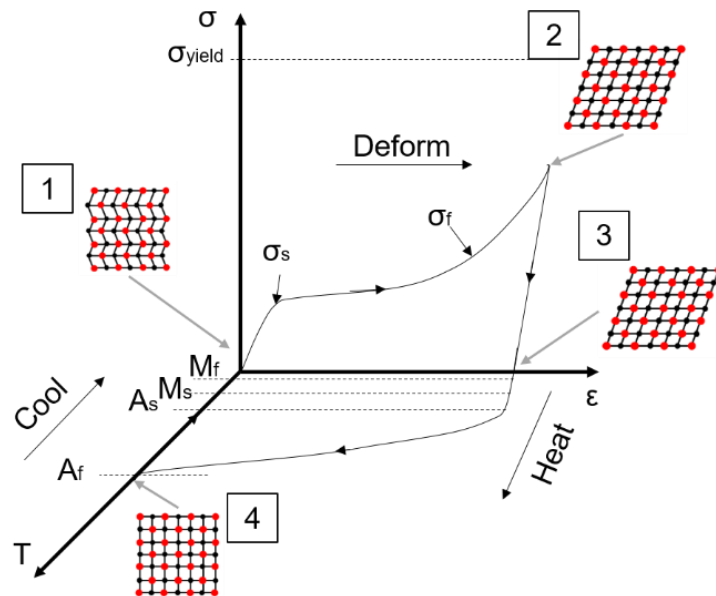


Figure 1: Stress-strain temperature characteristics for a typical NiTi SMA, showing the so-called one-way-effect. [3, 28]

The martensite phase, whose lattice structure is shown in point 1, first has a twinned lattice structure. If the SMA is subjected to external stress above σ_s , it deforms pseudo-plastically, and the lattice planes fold over to detwinned martensite, as indicated in point 2. During this lattice change, a prominent plateau emerges between the start stress level (σ_s) and the finish stress level (σ_f), in which the strain greatly increases

without significantly increasing stress. The reorientation of the martensite induced by external stress σ occurs at a stress level far below the plastic yield stress of the martensite. [3] The reorientation states are limited to twinned or non-twinned martensite variants. Consequently, the shape change is not applied homogeneously over the SMA length. Instead, the lattices fold locally depending on the external load state. [29] The deformation is no longer reversible when the SMA yield stress (σ_{yield}) is reached. Between the points 2 and 3, the SMA is elastically unloaded, and no further external stress is applied. The SMA remains pseudoplastically strained except for a small elastic part. A phase transformation from detwinned martensite to austenite occurs, accompanied by shape recovery upon heating the SMA. At the heating temperature A_s , the phase transformation from detwinned martensite to austenite starts. This phase transformation ends with A_f , where only the austenite phase exists (point 4). Upon cooling the SMA, the martensite phase starts to rebuild, beginning at M_s , and by reaching M_f , only the twinned martensite phase exists in the SMA. During the cooling phase, no further shape change can be observed. After the complete cycle, the SMA is at the starting point 1, and the whole process can be repeated. [3, 15] Beyond the austenite and martensite phases, the manufacturing process can also cause the formation of an intermediate phase, the so-called R-phase. The nomenclature “R-phase” is derived, referring to the rhombohedral structure of the crystal. The occurrence of the phase in SMA materials depends on specific alloy compositions and cooling conditions. [30] Similar to the martensite phase, the R-phase also has a twin structure and can appear between transforming austenite into martensite [31].

2.2 Analysis and Description of Interfaces in FRP Composites

Interfaces are of the utmost importance in FRP composite materials and have been the focus of extensive research [32, 33]. The interface mainly influences the interaction between the fiber and the matrix and thus directly impacts the macroscopic properties, such as tensile strength [34, 35] or Young’s modulus [33] of the entire composite. The terminology “interphase” is commonly employed, especially in nanoscale analysis, to describe a specific intermediate phase that can form between the fiber and the polymer matrix with specific properties depending on the interaction between the fiber surface and the enveloping polymer matrix [32, 33]. The interphase thickness between carbon fiber and polymer matrix ranges from 100 to 200 nm, which is dependent on nanoscale

local changes of the chemical and physical processes, such as crystallization and crosslinking of the polymer matrix in the fiber area [36]. The term "interface" refers to a two-dimensional (2D) perspective centered on a macroscopic contact surface [37]. Chemical (covalent) and physical bonding (dipole-dipole) and/or mechanical interlocking between fiber and polymer matrix can be achieved [38].

The quantification of the interfacial strength between fiber and polymer matrix in single-fiber micromechanical experiments is highly complex and the analysis of the results depends on many boundary conditions, such as test speed, embedding length and test resolution [33, 39]. Ensuring reproducibility and sample quality during sample preparation is a major challenge [40]. The absence of a standardized test method complicates the comparison of publications within the field of research [41]. For FRP composites, the fragmentation test [42], the microbond test [43], the push-out test [44], the Broutman test [45] and the pull-out test [46] are mainly used to determine the fracture energy, the shear or the normal stress in the interface [33]. These tests are generally used for qualitative measurements to determine the impact of modifications on the interfacial strength on either the fiber or matrix side compared to an unmodified system. Moreover, these tests are used to indicate the interface-related failure modes. [33] The micromechanical tests described here are used to evaluate the interfacial strength between fibers and matrices in conventional FRP. However, many of these tests are not applicable to SMAHCs for various reasons. For example, the fragmentation test utilizes a polymer matrix with a higher elongation at break than the embedded fiber, resulting in a fiber-sided failure. In the context of this study, which deals with hybrid composites containing metallic fibers (especially SMA wire) in a polymer matrix, the pull-out test is the established method for analyzing the interfacial shear strength. The pull-out test is therefore used in this research to quantify the force transfer between an SMA wire and a polymer matrix, which will be further described in section 6.2.1. The fundamentals of this test method are explained in the following.

A single fiber is embedded in the corresponding matrix in the standard pull-out test. The polymer matrix can have different shapes, such as a cylinder, a square or a thin plate [33, 47]. The polymer matrix is maintained in a specially designed holder during the test to reduce clamping-induced stresses, and the force is induced via the free, non-embedded end of the fiber [48]. It is crucial for the pull-out test that the force is applied in the longitudinal direction of the fiber, ensuring that no transverse stresses occur. Therefore, the angle at which the fibers enter the polymer matrix is particularly

important. [49] The dimensions of the sample [50, 51], the test speed [52], the free fiber length [53] and the embedding length of the fiber [51, 53] are of decisive importance for the test and strongly influence the result [54]. The schematic test set-up already described is shown in Figure 2 a) and the resulting test curve is demonstrated schematically in Figure 2 b). The force increases quasi-linearly until the complete interface fails, characterized by a significant drop in force. A residual force transmission attributable to friction effects can be seen in the curve. However, the first interfacial failure cannot be recognized solely from the curve progression observed during the pull-out test. In order to determine the first interfacial failure, additional measuring methods such as acoustic emission [39] or, for transparent systems, stress optics can be used [55].

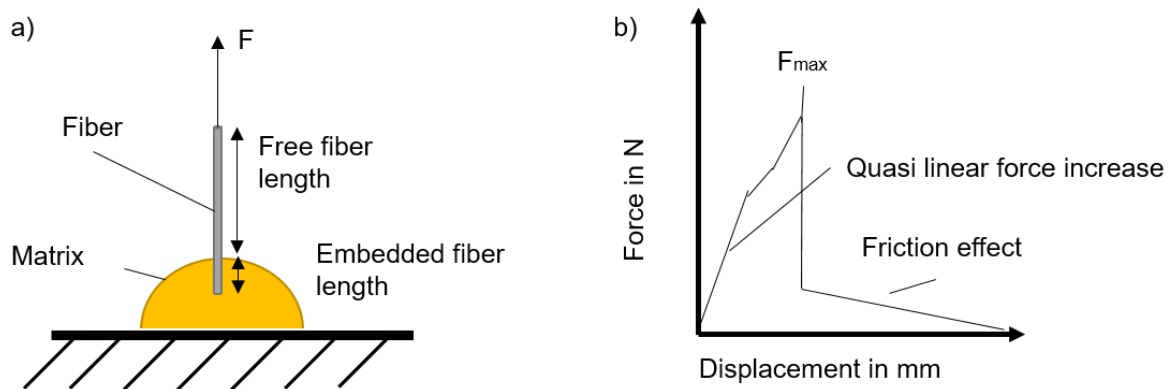


Figure 2: a) Schematic description of the single fiber pull-out test, b) exemplary resulting force-displacement-curve from the single fiber pull-out test showing the most important phases [56].

The analytical description of the pull-out test for composite materials is another challenge. Numerous analytical models have been developed to explain interfacial failure in FRP composite materials. These can be divided into two basic approaches: shear-lag and fracture mechanics theories [33]. Within the shear-lag theory proposed by Cox [57], debonding is postulated to occur when the interfacial shear stress reaches a critical value (maximum stress criterion) [58]. The fracture mechanics approach only describes the propagation of an interfacial crack when the potential energy release rate reaches a value corresponding to the interfacial fracture toughness (energy criterion) [59].

Depending on the interfacial micromechanical test procedure, the shear-lag theory has undergone many modifications and further developments over the years [33]. The shear-lag theory is based on a force balance approach with several simplifications.

Assumptions include the ideal adhesion between fiber and matrix, with the mechanical behavior of both components described as linear-elastic. A central problem of the analytical consideration arises from many unknown measurement influences such as sample quality, the forming interface and resulting stress distribution which are difficult or impossible to quantify, leading to many simplified assumptions. [33, 39]

The contributing influences on the interfacial failure behavior in composite materials are difficult to verify. An influence of the shear stress of the polymer matrix and the Poisson's ratio on the interfacial stress transfer is suspected [60]. The importance of the radial stress and the Poisson's ratio in the stress distribution of a composite is pointed out in [61]. The load transfer between fiber and polymer matrix depends entirely on the interface performance. For the investigation, a simplified micromechanical analysis model is typically used to consider a representative volume element containing an embedded fiber in a cylindrical polymer matrix to which a tensile force is applied. In particular, well-known model such as the Kelly-Tyson estimate the tensile stress in the fiber and the shear stress at the interface. [33]

Kelly-Tyson [42] originally described the mechanical interfacial behavior of a fiber embedded in a metallic matrix, showing a plasticity behavior of the matrix close to the fiber ends. The shear-lag theory proposed by Cox [57] assumes a perfect bonding between fiber and matrix, with an elastic material behavior of both fiber and matrix. The progression of the one-dimensional interfacial shear stress of an embedded fiber element after Cox is visualized in Figure 3. The fiber element is loaded with tension on both ends, and only the axial components are considered. The free end edges effect is an often neglected substantial effect in analytical considerations. This effect describes an increase in stress at the polymer entry point of the fiber caused by the hard phase edge [62] and can also be observed for pull-out tests with SMA wire embedded in the polymer matrix [63]. The influence of the position along the embedded fiber on the resulting shear stress was also analyzed in [64]. They observed an interfacial failure before the maximum interfacial strength was reached.

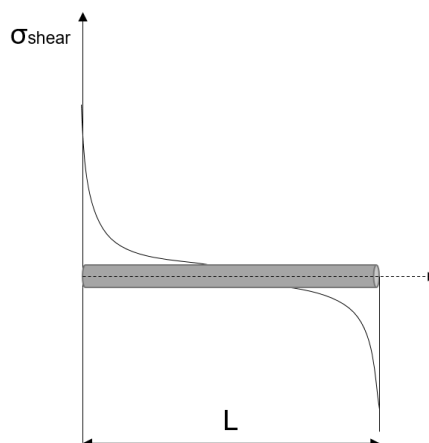


Figure 3: Interfacial shear stress distribution of an embedded fiber in a cylindrical matrix after Cox [57].

2.3 X-ray Microcomputed Tomography for Composite Materials

For composite materials characterization, μ CT analysis has grown substantially in recent years [65]. The conventional μ CT setup comprises an X-ray source, a sample stage and a detector, capturing the through the sample transmitted X-rays. The conventional μ CT setup is visualized in Figure 4. During μ CT analysis, two-dimensional (2D) X-ray images are gathered within different angles from the sample, which can be later reconstructed to a three-dimensional (3D) rendered volume [66, 67]. This methodology enables a comprehensive 3D analysis of materials [68]. In the last years, the spatial resolution for μ CT analysis was improved by simultaneously reducing the acquisition time needed. By using X-ray μ CT analysis, the inner structure of a material can be visualized. The observed area, the so-called Field of View (FoV), depends on the pixel resolution and the amount of pixels in the detector. A relevant part of the sample for further analysis can be extracted and analyzed from the scanned FoV; this area is called the region of interest (ROI). The resolution should be chosen to be larger than three times the most minor feature that should be visualized. [65]

The segmentation of data acquired with μ CT plays a very prominent role in the analysis of composites. For example, the fiber orientations and volume contents can be determined by segmentation. [65] Different segmentation techniques have been proposed in the last decade [65, 69]. Using segmentation techniques, the optical gathered data can be quantified, and further analysis can be done.

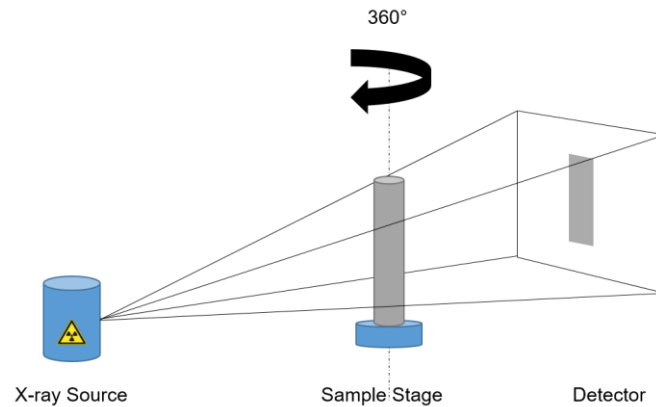


Figure 4: Schematic classical X-ray μ CT analysis set up, consisting of an X-ray source, a sample stage and a detector [70].

Synchrotrons are a special type of μ CT characterized by their highly collimated and almost parallel beam. They also have a photon flux several orders of magnitude higher than conventional X-ray sources. This has several advantages: Compared to conventional X-ray sources, measurements can be taken much faster. [65] This means that even complex *in situ* experiments can be performed several times, resulting in a certain level of statistics. Also, the contrasts are stronger, and the scan artifacts that occur are smaller. Beam hardening artifacts can occur for hybrid composites (HC) such as SMAHCs. These are caused by the polychromatic nature of the X-ray anode and occur due to the high density of the SMA wires. [71] The standard reconstruction algorithms (filtered back projection) do not consider the shift in the X-ray spectrum caused by the combination of different density materials. The Lambert-Beer law [72], the basis for the reconstruction algorithms, refers to monochromatic X-rays and a linear relationship between X-ray beam attenuation and sample thickness. [73] The combination of materials, such as polymer combined with metal, shifts the average energy of the spectrum to higher values as the X-rays are transmitted through the sample. This results in a higher transfer than assumed in the Lambert-Beer law. [74] As a result, black bands appear between and around highly attenuated structures surrounded by softer materials [68].

2.4 X-ray *in situ* Analyzing the Interfacial Failure Process in FRP Composite

The potential for combining X-ray μ CT analysis with micromechanical testing is shown by [39, 75, 76], which demonstrated the capability to combine detailed structural insights with the mechanical assessment of the interfacial strength.

[39, 75] used X-ray μ CT analysis to analyze the interfacial failure pattern after the micromechanical testing to better understand the interfacial failure process. [76] used an X-ray μ CT *in situ* fragmentation in combination with digital volume correlation (DVC) to understand the strain distribution in the surrounding polymer matrix during the fragmentation test. Barium titanate particles were integrated into the epoxy polymer matrix as a speckle pattern. The influence of the strain distribution during the fragmentation test in the polymer matrix on the fracture pattern of the embedded single carbon or glass fibers was analyzed. The fiber breakage during the fragmentation test could be correlated with the shear strain distribution in the surrounding matrix.

More research has been published for the macromechanical understanding of the fiber-matrix interface with X-ray μ CT *in situ* testing [77, 78, 79]. Those tests are highly time-consuming, and a compromise between resolution and FoV leads to a restricted observation area. Due to the time-consuming testing, data collecting for statistical measurements is limited [77].

3 State of the art

3.1 Thermomechanical Characterization of Non-Embedded SMA Wires

In the application of SMA materials, the unique characteristics of the SMA described in section 2.1 require comprehensive measurement and quantification. Various research works deal with the characterization of SMA wires [80, 81, 82, 83]. The resulting non-linear characteristics of the SMA are highly dependent on the testing procedure itself and the applied temperature [80]. For a good thermomechanical characterization of one-way-effect SMA wires, it is essential to characterize key parameters such as the mechanical detwinning characteristic [3, 4], the transformation temperatures [84], the stress-strain characteristics when subjected to an external load [85] and the surface condition after applying any surface treatment [86].

The classic tensile test can be applied to characterize the detwinning behavior of the SMA wire at room temperature or for pre-straining prior to further testing. However, the strain rate used in this tensile test significantly influences the results. High-velocity strain rates lead to homogeneous straining but can be susceptible to thermal effects, while slow strain rates can lead to localized strain concentrations [87]. The tensile test is used in this research to analyze the stress-strain characteristics of the SMA wire, which is described in further detail in section 6.1.1. However, only the global total strain applied to the SMA wire during tensile stress can be determined with this method. Various measurement techniques, such as digital image correlation (DIC) used in [29, 88, 89], enable the precise measurement of the actual 2D local strain distribution on the SMA surface during the straining or phase transformation of the SMA material. DIC is a tool for non-contact optical measurement of the full-field displacement observed on a surface with a non-uniform distributed pattern, often named speckle pattern. Applying a load causes strain, which results in a change in the observed speckle pattern. The change over time/load can be measured and analyzed by comparing images from the same surface at different time/load steps. The change in the speckle pattern can be described as axial (in load direction) and radial (circumferential to the SMA wire) by analyzing the change of the tracking points in relation to each other in these two main directions. [90]

[29] used DIC analysis to understand the stress-strain characteristics of an SMA tube under bending. The researchers have shown that an applied strain to the SMA tube

does not result in a homogenous strain over the SMA tube length but is applied partly by the detwinning. Also, *in situ* X-ray diffraction (XRD) analysis can be used to understand the SME and the detwinning characteristic [91, 92].

To determine the transformation temperatures described in section 2.1, differential scanning calorimetry (DSC) [3, 81] or dynamic mechanical temperature analysis (DMTA) [93] measurements can be conducted on the pre-strained one-way effect SMA wire. The characterization of the transformation temperature using DMTA is explained in more detail in section 6.1.3. To characterize the behavior of the SMA wire under load, the pre-strained SMA wire can, for example, be activated by Joule heating while it is working against a load, such as a spring. This is explained in more detail in section 6.1.2 and in [87, 94]. The actuation potential and the work capability of the SMA wire with variable external stress and temperature can thus be tested.

The determination of Poisson's ratio of SMA wire is highly complex due to the strong dependency on the transformation behavior and the complex stress-strain characteristics influenced by the temperature of the SMA wire. This results in a high variance in the literature values. However, the Poisson's ratio is an important parameter for characterizing SMA wires. In [95], *in situ* neutron diffraction under loading was used to measure the Poisson's ratio of a NiTi SMA rod, resulting in an average value of 0.387 for the martensitic phase. Different values are reported in research between 0.37 and 1.77 [95, 96, 97] for the martensite phase and 0.31 and 0.44 for austenite [27, 96, 98].

3.2 Shape Memory Alloy Hybrid Composite

As described in [99], the already explored potential of SMA materials can be utilized in two different ways: by developing novel alloy compositions and material systems or by integrating these alloys with existing materials to form HC. For this research, the second possibility is relevant. The combination of FRP and SMA is explicitly addressed to develop an SMAHC.

The meaning of FRP materials for lightweight, high-performance applications is constantly growing. The anisotropically adjustable properties contribute substantially to the success of these composite materials. [100] Polymer matrix based composite materials are available in various designs, with different fiber types, such as glass, carbon, aramid or natural fibers, in different lengths and configurations with individually designable property profiles [101]. By incorporating SMA wires within FRP, an SMAHC can

be built, which can act as sensors and actuators or react to external influences [102]. SMAHC's key design parameters include the choice of integrated SMA wire types and their diameter. Other design considerations include the placement of the SMA reinforcement within the composite structure, whether as a separate layer, embedded in a polymer matrix or in the middle of the fibers. In addition, the overall design includes structural aspects such as orientation, number of layers, fiber type and related properties of the FRP. [103]

The research presented in this work is relevant for developing SMAHC with fully integrated SMA wires directly into a polymer matrix. For matrix material, most SMAHC research uses thermoset matrix systems (mainly epoxy) [104]. Also, a few attempts have been made with thermoplastic matrices [105, 106]. The manufacturing of SMAHC is influenced by the chosen polymer matrix system, with the processing temperatures playing a critical role. The use of elevated temperatures during the curing of polymer matrices is limited, as unintentional activation of the SMA wires must be prevented throughout the manufacturing process. To overcome this limitation, many researchers are considering cold-curing matrix systems as an alternative approach. [13, 107] Using cold-curing matrices, post-curing effects often occur in the polymer matrix during an SMAHC's lifecycle. The application is often limited in terms of elongation at break.

As considered in this research, a possible application for the SMAHC is the so-called bimorph actuators [21, 108]. By integrating the SMA wire with an offset to the neutral axis into an FRP structure, a bending moment can be introduced by activating the SMA wire. The SMA wire works against the stiff composite structure. [4, 109, 110] Regardless of the application, the stress and strain transfer between the SMA wire and the encasing structure is critical and usually one of the performance-limiting factors [14, 107, 111].

3.3 Interface Strength Improvement Techniques in SMAHC

In SMAHC systems incorporating an SMA wire into a polymer matrix, the term “interface” is predominantly used to describe a macroscopic 2D contact phase between the constituents [104, 112]. For SMAHC systems without additional force transfer enhancement techniques, an important mechanism for force transfer across the interface is surface roughness and matrix shrinkage during the curing process, resulting in pre-existing stresses.

The force transfer enhancement technique can be divided into SMA wire-sided, polymer matrix-sided modification or integrating additional force transferring elements. The optimization of the force transfer between the SMA wire and the polymer matrix using additional force-transmitting elements, such as the insertion of anchors and seams, is documented in [13, 87]. However, the current research takes a different approach by fully integrating SMA wires and optimizing the force transfer fiber-sided through selective electrochemical etching of the SMA wire surface. This is why the discussion of this research focuses on the fiber-sided modification of the improvement of the interfacial force transfer and the approaches that have been published in this context. Numerous studies have been published on the alteration of the surfaces of SMA wires by various surface treatment processes. However, these studies often lack a comprehensive analysis of the correlation between the resulting interfacial strength and surface treatment's effects on the SMA wire's thermomechanical properties:

For the fiber-sided modification, different approaches are used to change the surface condition of the SMA wire, which are described below. Numerous researchers have used coupling agents to improve the force transfer efficiency, as described in [12, 113, 114, 115, 116]. [114] improved the interface strength by 100 % compared to the untreated SMA wire by functionalizing the SMA wire surface with silane coupling agents. The adhesive reacts on one side with metal surfaces and on the other side with the polymer matrix (polymethylmethacrylate (PMMA)). The chemical reaction is intended to create covalent bonds that contribute to an improvement of the interfacial bonding properties between the SMA wire and polymer matrix. However, the improvement of force transfer is limited to the material combination shown and, therefore, cannot be easily transferred to other material combinations. In the conducted researches, the thermomechanical characteristics of the SMA wire were not further analyzed. But, the changes in surface condition due to the different surface treatments were investigated by using different analysis methods: scanning electron microscope (SEM) imaging partly combined with energy dispersive X-ray spectroscopy (EDS) analysis, atomic force microscope (AFM), contact angle measurements and X-ray photoelectron spectroscopy (XPS).

Increasing the surface roughness of the SMA wire with multiple abrasive surface treatment methods, resulting in an enlargement of the contact surface, was investigated by [10, 12, 13, 63, 105, 115, 117], [118]. With some of the abrasive methods, mechanical interlocking can also be achieved. In [118], the importance of generating mechanical

interlocking between SMA wire and polymer matrix for increasing the interfacial shear strength is noted. Moreover, they pointed out that the choice of surface treatment can influence the thermomechanical properties of the SMA wire.

Researchers [10, 12, 49, 105, 115] used abrasive mechanical treatments such as sandpaper with different grain sizes or glass-/sandblasting for the SMA wire surface treatment. However, these methods achieved little to no improvement in adhesion, especially compared to the increase in bonding achieved by coupling agents. The SMA wire surface characterization was done using AFM, SEM and profilometric analysis. The influence of the thermomechanical characteristic of the SMA wire was not included in these researches.

Laser structuring of the surface of the SMA wire was used to increase the surface roughness and thus optimize the adhesion between the SMA wire and the polymer matrix in [117]. NiTi ribbons with a thickness of 0.35 mm were utilized in [117], and a surface structure was created using a solid state laser device. In their work, surface channels for matrix infiltration were introduced. The microstructural analysis of the surface morphology was done using an optical micrograph. The PMMA matrix should infiltrate the surface structure and generate a mechanical interlocking. The thermomechanical characterization of the resulting SMAHC was done using thermomechanical analysis (TMA) and dynamic mechanical analysis (DMA). The single materials were also characterized with DSC, but only before the surface treatment. The improvement of the adhesion due to laser structuring the SMA ribbon surface was 80 % compared to non-treated samples. The interface was not tested directly micromechanically, but they characterized the SMA ribbon surface by using SEM and microhardness test.

A laser gas nitriding process was used in [119] to improve the interfacial bonding between two SMA strips and an epoxy matrix. They used a lap-joint tensile test to analyze the interfacial adhesion properties. Compared to sandblasted and chemically etched surfaces, a 150 % increase of the interfacial strength could be observed. However, the influence of the surface treatment on the thermomechanical SMA wire characteristics was not further analyzed. The surface microstructure and morphology was analyzed by DE-SEM and SEM.

Increasing the surface roughness of an SMA wire can also be achieved using chemical treatment methods, such as chemical etching of the SMA wire surface.

[10, 115, 120, 121, 122, 123] used different aqueous acidic solutions containing hydrochloric acid (HCL), nitric acid (HNO₃), sulfuric acid (H₂SO₄) and/or hydrofluoric acid

(HF), with different treatment times. The improvement of the interfacial force transfer was mainly attributed to the increase in surface roughness [120]. The applied surface on the SMA wire was characterized by using SEM imaging and 3D SEM.

Only [123] and [124] measured the influence of the surface treatment on the thermo-mechanical properties of the SMA wire by using a tensile test [123] and thermal desorption analysis (TDA) [124]. [123] showed a reduction of the tensile strength after the surface treatment of the SMA wire with HNO₃. [124] reported embrittlement attributed to hydrogen absorption, independent of the immersion time, of the SMA wire by treatment with different aqueous acidic solutions.

The interfacial adhesion in SMAHC can be modulated by altering the properties of the polymer matrix, as described in [125]. They mixed a silane coupling agent into the epoxy polymer matrix to generate chemical bonding between the SMA wire and the polymer matrix. Using SEM images and XPS, their study showed that chemical bond formation was favored by incorporating adhesion promoters. An alternative approach is analyzing the influence of the chosen polymer matrix system on the interfacial force transfer between SMA wire and polymer matrix, as described in [105, 113].

The above-presented research works only address the influence of surface treatment on the thermomechanical properties of SMA wires to a limited extent or not at all. The SMA properties are predominantly analyzed before the surface treatment, and optical methods are mainly used to describe the resulting surface morphology. Nevertheless, the potential of using a fiber-sided modification to improve the force transfer between SMA material and polymer matrix is demonstrated.

3.4 Measurement and Description of Interface Strength in SMAHC

Most of the research presented in section 3.3 has utilized the pull-out test to quantify the force transfer between the SMA materials and various polymer matrices, as visualized in Table 1. This micromechanical test is the most widely accepted state of the art test for characterizing the interfacial shear strength between SMA wire and polymer matrix [111, 126, 127]. It is therefore used in this research to measure the force transfer. The pull-out test for classical composite materials described in section 2.2 is also relevant for SMAHC.

Using a pull-out test to characterize the force transfer in SMAHC depends not only on the selected material combination and modifications but also on the test speed, the

selected dimensions (embedding length [105], sample size (matrix and SMA) [50, 63], free fiber length [128] and the additional analytical measurement technique [10, 126]. Because of this, a lack of comparability of the published researches is evident. Consequently, the different methods for improving force transfer, as described in section 3.3, are not directly comparable. This emphasizes the need for a comprehensive study of force transfer optimization and its effects, given the complexity of establishing a comprehensive knowledge framework based on previously published findings.

In [126], a long embedding length (50 mm) using the pull-out test is proposed to analyze the influence of the martensitic transformation on the first interfacial failure since the position on the embedded SMA wire length significantly influences the resulting interfacial shear stress.

The resulting pull-out test curves usually show a large scatter for the same testing configuration, so a certain number of samples must be analyzed for statistical validation [12, 63, 127]. As mentioned in section 2.2 for classical composite materials, the first failure cannot be derived from the resulting force-displacement curve. To solve this problem, [126, 127] used stress-optical methods to observe the interfacial failure process and to identify the moment of the first failure. This is discussed in more detail in section 3.5.

The pull-out test described in section 2.2 has been further developed to estimate the interfacial strength when the SMA wire is intrinsically activated (thermal-activated pull-out test) [13]. For this purpose, pre-strained SMA wires or two-way effect SMA wires are embedded, and the pull-out is induced by thermal activation of the SMA wire with, for example, joule heating. Those analyses are further used to gain a deeper understanding and to evaluate the temperature dependency of the interfacial failure-driven mechanism. Nevertheless, the further developed pull-out test induced a complex stress-strain state and the temperature influences the thermomechanical behavior of the surrounding polymer matrix. The thermal-induced activation of the SMA wire leads to an unpredictable stress distribution along the SMA wire length.

[13, 52] showed that the temperature and the pull-out speed affect the interface strength between the SMA wire and polymer matrix. Higher interfacial strength was measured for the thermal-activated SMA wire pull-out test, which was mainly attributed to the change in the polymer matrix stiffness influenced by the applied temperature. In [111], a higher interfacial shear stress for heated samples was observed, which was attributed to the intrinsic recovery stress in the SMA wire, which compensates for the

externally applied load. Due to the complexity of the resulting stress state and the increase of non-describable measurement influences, the pull-out test, as described in section 2.2, is the focus of this research and is further described in section 6.2.1. An overview of the state of the art regarding improving the interfacial shear strength by surface treatment of the SMA wire and the used testing methods is given in Table 1. This list does not claim to be exhaustive but summarizes the relevant studies to this research.

For numerical analyses of the pull-out behavior of a single-embedded SMA wire, the shear-lag theory is often used [129]. The model description of the shear interfacial strength for classical composite materials is a complex task, as described in section 2.2. For SMAHC, the theoretical description of the pull-out test gets even more complicated because of the SMA wire nonlinear, hysteretic, rate- and temperature-dependent stress-strain characteristics, as described in section 2.1 [103, 104, 109].

[118] used a further development of the shear-lag model, Grezczuck's model [50], for the theoretical analysis of the shear stress in the interface between SMA wire and polymer matrix during the pull-out test. This model was also used in [13, 130]. In this model, the interfacial stress distribution along the embedded SMA wire length axis is not assumed to be constant. The maximum interfacial stress is assumed at the SMA wire entry point. This model is also used in this research to calculate the interfacial shear stress between the SMA wire and polymer matrix and is therefore described in more detail in section 6.2.3.

[131] formulated an analytical model to predict the interfacial shear failure of pre-stressed SMA wires embedded in an epoxy matrix during the pull-out test. Tensile tests, stress recovery tests, and tests under strain restriction were carried out to characterize the thermomechanical properties of the materials used. The theoretical description included the ambient temperature and was validated by experimental tests. External loads acting on the SMA wire have also been integrated into the analytical description. The researchers used Brinson's constitutive [132] to describe the recovery stresses of the SMA wire when heated to a specific temperature. A fracture mechanic approach was followed in the described research to formulate an interfacial debonding criterion. A good agreement was found between the experiments and the fracture mechanic based analytical description. Hence, a fracture mechanics approach was also pursued in this research, as outlined in section 6.2.4, to consider the above mentioned considerations.

Table 1: Overview state of the art improvement and measurement of the interfacial strength by surface treatment of the SMA wire.

Source	Matrix material	SMA material	SMA wire surface treatment	Improvement of force transfer	Best treatment	Analytical method surface	Thermomechanical characterization SMA	Force transfer test method	Additional analytical method
	Thermoset	Thermoplast		mechanical			before		
				chemical bonding			after		
[12]		NIT SMA ribbon (50.8 % Ni) 0.63 x 3.3 mm ²	Two coupling agents, plasma treatment mechanical grinding and polishing, electropolishing	x	Mechanical polishing + coupling agent + plasma treatment	XPS, AFM, contact angle measurement, SEM	DSC	pull-out, number of samples: 5/variant embedding length: 20 mm, free SMA wire: 20-30 mm, test speed: -	
[113]	Vinylester	SMA wire (0.5 mm)	Chemical etching, coupling agent	x	PE matrix, coupling agent	SEM, EDS	DSC	pull-out, number of samples: - embedding length: 20 mm, free SMA wire: 30 mm, test speed: 1 mm/min	Strain recovery test with 4%, 5%, 6%
[114]		SMA wire (0.762 mm)	Chemical etching, functionalized surface, coupling agent	x	azobis-isopropionitrile + surface functionalization	XPS		pull-out, number of samples: 3-19/variant embedding length: varied, free SMA wire: varied, test speed: 0.2 mm/s	
[115]	Epoxy	SMA wire (0.8 mm)	mechanical abrading, chemical etching	x	chemical etching	ESEM, EDXS electrochemical impedance spectroscopy, polarisation curves, potential vs time measurements		pull-out, number of samples: 8/variant embedding length: 5 mm, free SMA wire length: -, test speed: 0.1 mm/min	
[105]	Epoxy/ Graphite composite	SMA wire (0.381 mm)	hand sanded, acid-cleaned, sand-blasted	x	sand blasted	SEM		pull-out, number of samples: 5/variant embedding length: 2.5, 5, 1, 7.6 cm, free SMA wire length: 2.5-7 cm, test speed: 0.5-1 mm/s	
[13]	Epoxy	SMA wire (0.5 mm)	hand sanded, force transferring elements	x	force transferring elements			pull-out test, number of samples: 5/variant embedding length: 50 mm, free SMA wire length: -, test speed: 25%/min, 1000%/min	Activation induced pull-out test
[63]	Thermoplastic polyolefin	SMA wire (0.38-0.75 mm)	chemical etch, chemical conversion coating, hand sanding	x	regarding standard deviation no difference	AFM		pull-out test, number of samples: 10/variant embedding length: 70, 90 mm, free SMA wire length: -, test speed: -	FEM analysis

Source	Matrix material	SMA material	SMA wire surface treatment	Improvement of force transfer		Best treatment	Analytical method surface	Thermomechanical characterization SMA		Force transfer test method	Additional analytical method
				mechanical	chemical bonding			before	after		
[118]	Thermoset										
	Epoxy	SMA wire	glass blasted, anodized, prestrained,	x		anodized	profilometric analysis	method of 4 wires		pull-out test, number of samples: 4/variant, embedding length: -, free SMA wire length: -, test speed: 0.5 mm/s	modal analysis
[10]		SMA wire (0.15 mm)	acid etched, hand sanded, sandblasted	x		sandblasted				pull-out test, number of samples: 2/variant, embedding length: 1.27 mm, free SMA wire length: 40-50 mm, test speed: 0.1 mm/s	stress-optics
[116]	Epoxy	SMA wire (1 mm)	coupling agent		x	1-2% coupling agent	XPS, SEM			pull-out test, number of samples: 4/variant, embedding length: 60 mm, free SMA wire length: -, test speed: 1 mm/min	
[117]		NITI SMA ribbon (0.35 mm)	laser structured	x		laser structured	SEM				
[120]	CFRP	SMA wire (0.4 mm)	chemical etching	x		HF + HNO3	SEM roughness analyzer		DMA, TMA, DSC, tensile test	pull-out test, number of samples: 10/variant, embedding length: 5mm, free SMA wire length: 40 mm, test speed: 0.1 mm/s	
[121]	Epoxy	SMA wire (0.3 mm)	chemical etching, mechanical grinding	x		Chemical etched	SEM			pull-out test, number of samples: 3/variant, embedding length: 30 mm, free SMA wire length: -, test speed: 0.5 mm/min	

3.5 Current Understanding of the Interfacial Failure Process in SMAHC During Pull-Out Test Gained by Incorporating Optical Methods

Due to the typical stress-strain characteristics of non-embedded SMA wire discussed in section 2.1, there are differing views in the scientific literature on the specific effects that contribute to the interfacial failure of an SMAHC. Specifically, it is unclear whether the interfacial failure in an SMAHC is stress- or strain-induced [113]. Especially for SMAHC with a stiff matrix like epoxy, there is a wide discrepancy between the maximum elongation at break of the polymer matrix (usually in the range of 3 - 6 % [133]) and the actuation recovery axial strain of the SMA wire (up to 8 % as described in section 2.1). Understanding the interaction between SMA wire and polymer matrix is essential for the analytical modeling and design of SMAHC. The influence of the thermomechanical clamping of the polymer matrix on the stress-strain characteristics of the embedded SMA wire has been rarely investigated so far [10, 14, 134]. The micro-mechanical measurement of the interface strength and the investigation of the failure modes occurring during interfacial failure are important.

In situ SEM observations of the failure process during thermal-induced pull-out tests were conducted in [135]. The analysis's objective was the interfacial debonding process of different pre-strained SMA wires (0.5 mm) embedded in an epoxy polymer matrix. The debonding was induced by heating the SMA wire and the debonded area was analyzed with SEM imaging. In their study, correlations were found between circumferential cracks in the polymer matrix surrounding the SMA wire and the occurrence of high relative tensile stresses in the area of the SMA wire entry. Their study emphasized the physical constraints exerted by the surrounding polymer matrix on the stress-strain characteristics of the SMA wire. Furthermore, their study suggested a possible influence of increased relative tensile stresses during thermal activation of the SMA wire on the interfacial failure process. When heated, the SMA wire contracts, whereas the polymer matrix expands. In [136], an experimental and analytical study found that the stress distribution in SMAHC varied with different activation and loading conditions. However, the maximum shear stress was found to appear at the ends of the embedded SMA wire in the SMAHC and the maximum axial stress occurred at the midpoint of the embedment length of the SMA wire.

[11, 13, 126, 127] used stress optics with the pull-out test to observe the interfacial failure progression between the SMA wire and polymer matrix during the pull-out test

in situ. Using stress optics, the build-up and release of stresses transferred from the SMA wire to the polymer matrix can be observed during the pull-out test. Stress optics can be used to visualize the internal stresses that occur when a transparent sample is loaded. A linear stress optic set up consisting of a light source, a polarizer, an analyzer and a recording medium is used in this research and is further described in section 6.2.2 [130]. External stresses lead to anisotropies in samples, which can be observed due to optical birefringence. The stress-induced birefringence in the samples causes polarized light waves to split into two orthogonal components, which travel at different speeds in the sample. The resulting phase shift is visible by a polarizer that is shifted by 90° . [137]

[11, 13, 127] showed that the first debonding starts at the SMA wire entry point. The interfacial debonding propagates along the SMA wire length axis after the first interfacial failure until a complete interfacial failure appears. The first interfacial failure observed using stress optics was also taken to compare the force transfer for different surface treated SMA wires (section 3.3) embedded in the same polymer matrix.

In [126], stress optics was used to analyze the debonding initiation during the pull-out test for embedded SMA wires in different phase conditions and embedded steel fibers. The results were compared with each other. They showed that the SMA wire exhibits significantly lower debonding stress for the SMA wire in the R-phase or the martensitic phase. Moreover, a strong influence of Young's modulus of the embedded SMA wire on the interfacial debonding stress and an influence of the phase transformation is demonstrated.

In [11], the influence of martensitic lattice transformation on the interfacial debonding failure is further analyzed by comparing the influence of SMA wires with different stress-strain characteristics during the pull-out test using stress optics. The findings of their study showed that the SMA wire lattice transformation for the embedded part of the pull-out sample could only start after the first interfacial failure occurred. The non-embedded SMA wires of the study (this could not be shown for all SMA wires) experienced a lattice transformation before the stress transfer over the interface started. Moreover, they showed an influence of the SMA wire's stress-strain characteristics on the interfacial failure's propagation speed.

The influence of the phase state of the SMA wire on the interfacial failure behavior is also investigated in [27]. They performed pull-out tests on embedded SMA wires in different phase conditions and observed that the SMA wires showed higher interfacial

failure loads in the austenite than those in the martensite phase. Moreover, they could show a correlation between interfacial shear strength and the load needed for martensite transformation. This was attributed to the difference in Poisson's ratio of both phases. They also postulated a relation between Young's modulus and interfacial failure. SMA wires with a higher Young's modulus show a lower interfacial strength. Using DIC to characterize the strain applied on the SMA wire during testing was already part of other research. Most research in that field has focused on non-embedded SMA material, as described in section 3.1. Nevertheless, a few attempts have been made to analyze the strain behavior of the embedded SMA wire during testing [89]. In this study, a polyurethane (PU) embedded pre-strained SMA wire was tested in a specially designed actuation pull-out test. The random speckle pattern was applied to the PU matrix to measure the resulting strains during activation. By using DIC analysis, [89] were able to show that the polymer matrix strains slightly less than the embedded SMA wire, that the strain is not uniformly distributed along the embedded SMA wire length and that a volume-preserving behavior could be measured for the transverse contraction in the phase transformation for the one-way effect SMA wire that was used. DIC can provide more information, but especially considering the embedded SMA wires, it is often limited by resolution and distortions due to the enveloping polymer matrix. Moreover, the influence of the speckle pattern phase on the surface of the SMA wire on the interface characteristics is non-describable and not measurable. Uneven surfaces and inconsistent lightning are additional problems when using DIC in general or for analyzing the deformation behavior of inner structures. To overcome these limitations in this research, the applied SMA wire surface structuring with selective electrochemical etching is used as the speckle pattern for the image correlation, also called texture correlation. This is further described in section 6.3.3. Using the occurring texture of the sample is done mainly for trabecular bone tissues [138]. Combining this approach with X-ray μ CT analysis provides additional benefits, such as having volumetric information and a high resolution, allowing visualization of the microstructure in detail.

3.6 Summary of the Gaps in the State of the Art of Characterization and Improvement of the Interfacial Strength between SMA wire and Polymer Matrix

The optimization and measurement of the interfacial properties of SMAHC are part of many research approaches, as discussed in the previous sections. Surface treatments of the SMA wire can result in an improved interfacial strength between the SMA wire and polymer matrix. Generating chemical bonding using silane coupling agents is promising, but the surface treatment methods are limited to predefined material combinations. Chemical etching and mechanical grinding have been shown to be effective in improving force transmission; however, their effects on the thermomechanical properties of the SMA wire are still unexplored. Additionally, those treatments often lack reproducibility and cannot be applied homogeneously. Quantification of the applied surface roughness is often limited to a very small surface area. The present research aims to close this gap, as described in section 4, part 1.

Optical methods can be used to gain a deeper understanding of the processes of interface failure and the interaction between the SMA wire and the polymer matrix. Stress optics enables the observation of the first failure and the failure progression at the interface during the pull-out test. The pull-out test is predominantly used to evaluate the effects of surface treatment on interface failure. Published research objectives differ significantly due to the complex nature of micromechanical experiments, which depend on numerous parameters, limiting the comparability of studies described in sections 3.4 and 3.5. Consequently, a comprehensive experimental and analytical investigation of the interfacial strength between the SMA wire and the polymer matrix is a key aspect of this research, as outlined in section 4, part 2.

However, the methods described in sections 3.4 and 3.5 cannot measure the interfacial shear stress and strain. The description of the stress-strain characteristics of the embedded SMA wire is often limited due to resolution or optical distortion effects. In particular, the actual strain applied to the embedded SMA wire during the pull-out test has not yet been quantified. The interfacial failure can be stress- or strain-related. The failure-causing quantity for the interface failure between the SMA wire and the polymer matrix is commonly discussed regarding the non-linear stress-strain characteristic of the SMA wire. As described in section 3.5, the phase transformation of the SMA wire

and the related change of Young's modulus and Poisson's ratio are assumed to influence the interfacial failure progress. Also, the influence of the surrounding polymer matrix on the stress-strain characteristics of the SMA wire due to external thermomechanical clamping is not known and has been poorly studied. Understanding the micromechanical failure-induced processes and the interaction of both materials is critical for developing and modeling macromechanical SMAHC. To gain a deeper understanding of the interfacial failure process, the force transfer and the analysis of the influence of the thermomechanical clamping of the polymer matrix on the embedded SMA wire stress-strain characteristics is the third part described in section 4.

The gaps identified in the state of the art are summarized briefly below:

- The effect of the surface treatment on the thermomechanical characteristics of the SMA wire is roughly studied. Quantification of the applied surface morphology is often limited to a small Field of View.
- Plenty of studies regarding the improvement of force transfer (interfacial strength) between SMA wire and polymer matrix have been published but are limited in the comparability. Since those studies focus on different objectives, a lack of comprehensive experimental and analytical investigations is identified.
- The influence of the unique stress-strain characteristics of the SMA wire on the interfacial failure progression is not yet fully understood.
- The real applied strain on the embedded SMA wire during the pull-out test has not been quantified.
- The influence of the thermomechanical clamping and the outside stress on the SMA wire by embedding it into a stiff polymer matrix has not yet been quantified and analyzed.

4 Aims and Solution Strategy

In order to close the gaps in the state of the art summarized in section 3.6, the strategy of this research is divided into three parts, as illustrated in Figure 5.

The first part deals with optimizing the SMA wire polymer interface strength by modifying the SMA wire surface. A selective electrochemical etching process, developed in cooperation with the University of Kiel, introduced a reproducible surface structure to the SMA wire, which is homogenous over the length and quantifiable using X-ray μ CT. Electrochemical treatments have been used mainly to improve NiTi SMA surface corrosion resistance and biocompatibility in biomedical applications [139, 140, 141, 142] or to fabricate micro actuators from SMA sheets [143, 144]. Some limited attempts have been made to use electrochemical treatments to improve the interfacial adhesion, mainly by anodizing [118, 145, 146], which often leads to a thick and rough oxide layer on the surface. But this is the first time this surface treatment method has been applied to a NiTi SMA wire to improve the interfacial strength between the SMA wire and polymer matrix. Compared with other SMA wire surface treatments, such as chemical etching (section 3.2), the electrochemical etching process offers several advantages, including improved time efficiency (with a total treatment time per SMA wire of less than half a minute) and reduced susceptibility to hydrogen embrittlement. This results from the short treatment time and the experimental setup in which the SMA wire is connected to the positive pole, causing positively charged hydrogen ions to be repelled from the treated surface. The chosen etching parameters can control the resulting SMA wire surface morphology. Different surface morphologies were applied to one-way-effect SMA wires from the same type but with different diameters (0.5 and 1 mm). In order to assess the possible effects of the SMA wire surface treatment process on the thermomechanical properties of the non-embedded SMA wire, a thermomechanical characterization is performed using DMTA, a specially designed actuation testing device and a tensile test both before and after surface treatment. The effect on the SMA wire surface is analyzed by SEM and the SMA wire surface morphology was quantified using microcomputed tomography (μ CT) analysis. The methods used for the thermomechanical and surface characterization of the SMA wires are explained in section 6.1 and the results are shown in section 7.1.

The second part characterizes the interface strength with mechanical laboratory pull-out tests between SMA wires with a structured surface and the surrounding epoxy

polymer matrix, compared to the as-delivered SMA wires. The increase in the contact area and the mechanical interlocking between the materials contribute to an improved bonding between the constituents. The influence of the applied SMA wire surface morphology on the improvement of the force transfer is analyzed by comparing different surface structured SMA wires with each other and the as-delivered SMA wire. As described previously, the pull-out test was chosen because it is an established method for almost quasistatic micromechanical interface analysis. Stress optic was used to measure the force of the first interfacial failure and observe the interfacial failure propagation between the SMA wire and the polymer matrix. The moment of the first interfacial failure between the SMA wire and the polymer matrix is important because the force transfer can no longer be guaranteed after the first interfacial failure appears. Two different approaches were used to analyze the force-displacement characteristics of the pull-out test. The shear stress was calculated by using the Greszczuk model. To improve the understanding of the influence of the surface morphology, both on the first failure and the complete failure of the interface, the area under the stress-displacement curves was calculated for all tested pull-out samples. This enabled the establishment of a new comparative parameter, the surface-dependent interfacial failure stress. The SEM images of the pulled-out SMA wires were analyzed to get a first impression of the interfacial failure process. The methods are described in section 6.2. The results are presented in section 7.2.

The third part aims to better understand the interfacial failure behavior and the interaction between the SMA wire and the polymer matrix. Plenty of studies in the last years have been focused on characterizing and improving the force transfer between SMA materials and polymer matrix. An unresolved scientific question concerns the elucidation of the mechanical basis of interface failure in relation to the behavior of SMA wires. In particular, the dependence of the interfacial failure mechanism on the complicated nonlinear stress-strain characteristics outlined in section 2.1 will be described. In this research, the X-ray μ CT *in situ* pull-out tests were performed in addition to the mechanical laboratory pull-out tests for the following reasons:

- Interface failure can be detected earlier due to the higher resolution.
- A direct correlation between the surface morphology of the SMA wire and the interfacial failure can be made.

- By combination with other analytical methods, the strain of the SMA wire during the μ CT *in situ* pull-out test can be determined for the region of interest.

The μ CT *in situ* pull-out test has the limitation that only a small FoV can be observed. The test is run as a stepwise load-increasing test and fewer statistics can be obtained due to the high testing time required. Therefore, both pull-out tests are used in this research.

X-ray μ CT *in situ* pull-out tests were conducted to get a precise, high resolution 3D view of the interfacial failure propagation. An understanding of interfacial failure is achieved by using additional analysis techniques such as segmentation and DVC analysis.

The characteristic strain behavior of SMA materials has already been widely studied and is explained in more depth in section 2.1. However, there has been little investigation of the characteristic stress-strain behavior of the SMA wire when embedded [10, 14, 89, 134]. Those investigations were limited by optical resolution. Generally, the investigation of the inner structures in composite materials is difficult. Due to the shrinkage of the polymer matrix and the mechanical interlocking of the structured SMA wire surface with the polymer matrix, external stress that is hardly quantifiable acts on the SMA wire. The methodology used is explained in section 6.3 and the results are presented in section 7.3.

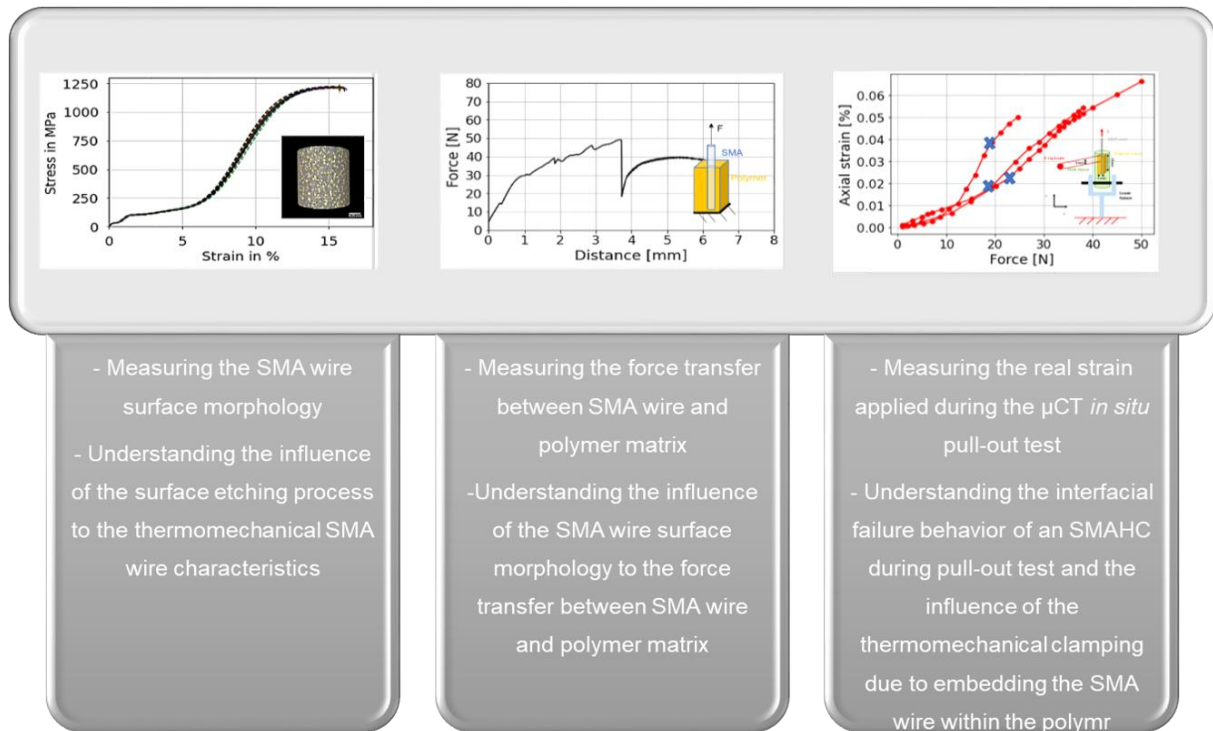


Figure 5: The analyzing strategy of this research is divided into three parts, in order to answer the formulated research questions.

As a result, the strategies address and provide answers to the following research questions:

1. Does selective electrochemical etching of the SMA wire alter its thermomechanical properties?
2. Does the surface structuring of the SMA wire improve the interfacial strength, and if so, can this improvement be attributed to specific features of the surface morphology?
3. Can optical quantification and monitoring of the structured surface of the SMA wire, obtained during the mechanical pull-out test, provide a better insight into the micromechanical interfacial failure processes?
4. Furthermore, does the surface structuring of the SMA wire contribute to a more comprehensive understanding of the interaction between the SMA wire and the polymer matrix and does it reveal whether the failure of the interface is stress- or strain-induced?

5 Materials & Sample Preparation

5.1 Polymer Matrix

For the application in SMAHCs, the polymer matrix must fulfill different partly contradictory requirements. To avoid the activation of the SMA wire during sample manufacturing, the polymer matrix must be cold curing. In addition, to penetrate the structured SMA wire surface pits, the viscosity of the polymer matrix must be low enough (approx. 1000-1500 cPs) [49]. The polymer matrix has to be stiff enough to hold the SMA wire during the phase transformation but flexible enough as the SMA wire exhibits until 8 % strain during phase transformation [15]. The selection of the polymer matrix resin was therefore based on careful considerations of various parameters, including viscosity and wetting behavior during processing, as well as the stiffness and strength of the cured polymer matrix. To meet the previously specified requirements for the polymer matrix, the cold-curing epoxy resin Araldite Aradur 5052 was purchased from Huntsman Corporation (The Woodlands, USA). The polymer matrix has also already been used and comprehensively characterized in the previous work of Sebastian Nissle [49] and Moritz Hübler [85]. Using previous experience and ensuring comparability were also reasons for choosing the mentioned polymer matrix system.

A 100 g Araldite® LY 5052 and 38 g Aradur® 5052 formulation was manually mixed for 2 minutes at RT. In order to achieve a polymer matrix without any voids, the polymer matrix was subjected to a two-day curing. The curing process was done in an autoclave, following predetermined conditions of 2 bar at room temperature (RT). During curing, the polymer matrix reacts exothermal, resulting in heat development below 50 °C [85]. This exothermal reaction temperature is below A_s of the SMA wire, as described in section 5.2. Subsequently, the polymer matrix underwent an additional curing period of at least five days under atmospheric pressure at RT. The material data for the epoxy polymer matrix used, provided by the manufacturer [147], as well as the calculated shear modulus* according to Ehrenstein [148] and a reference literature value for the cure shrinkage** of an epoxy resin [149], are summarized in Table 2. Also, the most essential properties of the polymer matrix system are summarized in the following. The characterization of the polymer matrix is outside the scope of this research.

Table 2: Mechanical properties of the cured epoxy polymer matrix [147]

Curing condition	Tensile modulus	Shear modulus*	Elongation at break	Poisson's ratio	Curing Shrinkage**
7d @ RT	3350 MPa	1241 MPa	1.5 - 2.5 %	0.35	2.5 %

5.2 SMA Wire

All experiments were carried out with a commercially available one-way effect NiTi SMA wire (Alloy H) from Memry Corporation (Bethel, USA) with a Ni content of 55.09 wt %. The manufacturer data sheet shows the A_s is 70 ± 10 °C [150]. The manufacturer removed the black oxide layer formed during the NiTi SMA wires manufacturing process. This research considered two nominal diameters, 0.5 and 1 mm [150]. The SMA wire with a nominal diameter of 1 mm was used to investigate whether the selective electrochemical etching process developed in cooperation with the University of Kiel [151] could be applied to the SMA wires. In order to transfer the results to real applications, more realistic SMA wire diameter tests were performed with the same SMA wire type but with a nominal diameter of 0.5 mm. Here, attention was focused mainly on understanding the interfacial failure behavior, the correlation between surface morphology and force transmission, and the force-strain behavior of the embedded SMA wire.

Prior to each test, all SMA wires were cleaned with Isopropanol and subjected to a 15-minute heat treatment in the oven at 100 °C to remove any residual stresses that may have resulted from storage or the manufacturing process. Subsequently, the SMA wires were allowed to cool down to RT and return to the martensitic state. The background of the unique, highly non-linear, reversible one-way characteristics is explained in section 2.1.

5.2.1 Selective Electrochemical Etching

This research uses selective electrochemical etching of the SMA wire surface to improve the interfacial strength between the SMA wire and the surrounding polymer matrix. The dissolution and oxide formation rates were chosen to be balanced, allowing control over the surface topography and chemical composition, resulting in a thin and unavoidable oxide layer on the metal surface. The electrochemical etching process

selectively targets defect sites, leaving the most thermodynamically stable surfaces of the SMA wire intact. The relevant aspects of this process are explained to understand the parameter dependencies related to the etching results observed in this research. Ti exhibits high activity (standard reduction potential $E_0 = -1.6$ V) [152], which allows easy dissolution and oxide formation upon direct contact with the electrolyte, even without additional electrochemical driving forces.

Conversely, a native titanium oxide (TiO_2) layer covering the surface of NiTi is resistant to chemical dissolution by Cl ions [153] and remains unaffected by our low-concentration electrolyte. Moreover, an insulating TiO_2 layer cannot be etched by an electrochemical equilibrium reaction governed by the Nernst equation because no significant potential is applied to the Helmholtz layers. Instead, the full applied potential drops predominantly across the TiO_2 layer, leading to the induction of high electric fields that result in localized electrical breakdowns [154]. Consequently, cracks in the TiO_2 layer and direct contact of pure metallic Ti with the electrolyte occur primarily at locations where the quality of the passivation layer is compromised due to underlying crystal defects, impurities, or localized roughness peaks. Subsequent robust Ti dissolution increases the breakdown gap by etching below the oxide and triggers positive feedback for further Ti dissolution. As a result, reaction products and reactants accumulate at the interface, preventing further Ti dissolution and supporting the formation of TiO_2 , resulting in the surface being covered with a closed TiO_2 layer. Thus, Ti dissolution is a sequence of self-reinforcing and suppressing processes that facilitate lateral coupling with adjacent surface regions. This leads to nonlinear collective phenomena that exhibit time-critical kinetic effects. Depending on the passivation layer formation and dissolution rate, certain sites, such as defect-rich phases with higher energy levels than undistorted regions, are more susceptible to etching. Once initiated, current flows predominantly through the existing pits, which grow mainly laterally due to the higher energy levels of the atoms at the pit edges where most bonds are broken. Applying current pulses after the nucleation step makes it possible to control dissolution and increase etch selectivity.

This research conducted selective electrochemical etching experiments using a custom-built set up comprising an etching cell, a DC voltage source, an electrolyte container, and a peristaltic pump. The working electrode (WE) or anode consisted of an SMA wire positioned within the etching cell. In contrast the counter electrode (CE) or

cathode consisted of a stainless steel hollow tube surrounding the SMA wire. This is schematically shown in Figure 6.

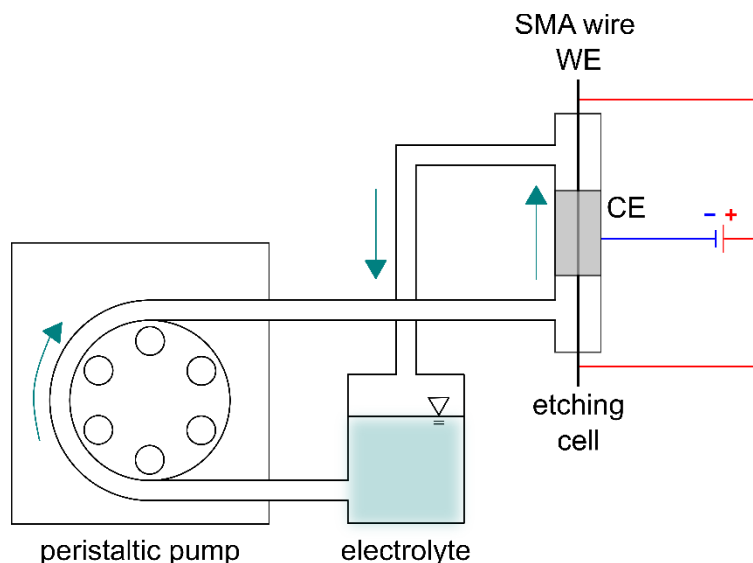


Figure 6: Schematic description of the custom-built selective electrochemical etching set up [130]

The SMA wire was connected to the positive terminal of the DC voltage source, while the counter electrode was connected to the negative terminal. The electrolyte utilized in this study was a solution containing 4.4 wt % NaCl and 0.26 wt % HCl, which was continuously circulated through the etching cell at a constant flow rate of 1.4 L/min using the peristaltic pump. The electrolyte temperature was maintained at 20 °C.

The electrochemical etching process was performed in a galvanic cell, with the applied current calculated based on the first surface area of the SMA wire and the desired current density for etching. The parameters governing pit formation, such as pulse duration and amplitude, could be controlled during the selective electrochemical etching. The specific parameters employed to achieve the desired surface morphology of the SMA wire are outlined in Table 3.

Table 3: Electrochemical etching parameters and introduction of specific naming of etching variants

Alloy H \varnothing	Designation Structure	Nucleation		Selective etching				
		Duration	Current density	Pulse duration		Pulse current density	No. of pulses	
				Current OFF	Current ON			
1 mm	Structure B1	0.25 s	8 A/cm ²	3 s	5 s	1 A/cm ²	3	
1 mm	Structure B2	0.25 s	10 A/cm ²	3 s	1 s	2.5 A/cm ²	6	
1 mm	Structure B3	0.25 s	10 A/cm ²	-	6 s	2.5 A/cm ²	-	
0.5 mm	Structure S1	0.5 s	16 A/cm ²	5 s	1 s	8 A/cm ²	3	
0.5 mm	Structure S2	0.5 s	16 A/cm ²	Long	Short	1 s	8 A/cm ²	3
				25 s	5 s			

The etching process involved multiple steps, including nucleation at high current densities and the application of pulses with resting intervals. The etching length for this study was set to 10 cm. Three morphologically different structures were obtained by etching in two steps for SMA wires with a nominal diameter of 1 mm: 1) nucleation at high current densities, 2) selective etching at lower current densities while the applied current is either pulsed (structures B1 and B2) or constant (Structure B3). The outgoing SMA wire surface morphology is shown with representative SEM images for the three different etching parameters used in this analysis in Figure 7. The analysis aimed to compare the surface morphology of three comparable surface structures with small differences. The SMA wire surface structured morphology is analyzed and the differences between the three different Structures are further described in section 7.1.1. The reproducibility of the selective electrochemical surface etching was demonstrated in [130] and is demonstrated in appendix A.1.

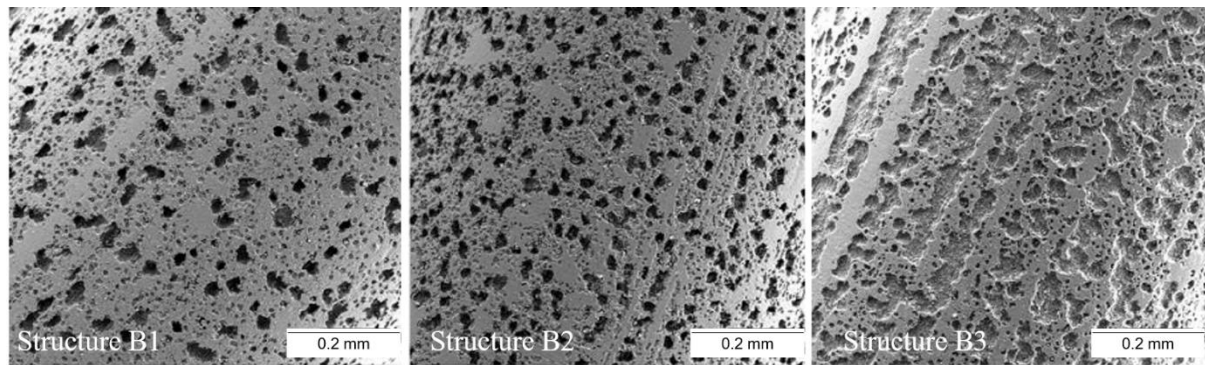


Figure 7: Representative SEM images of the structured SMA wire surface of the SMA wire with a nominal diameter of 1 mm for three different etching parameters [130].

Two structural variants were analyzed for the SMA wire with a nominal diameter of 0.5 mm, showing significant surface morphology differences. Representative SEM images of the applied SMA wire surface structures are shown in Figure 8. A detailed analysis of the introduced surface morphology is given in section 7.1.2.

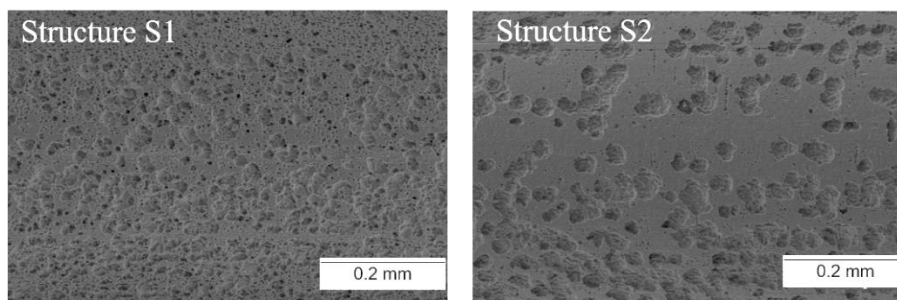


Figure 8: Representative SEM images of the structured SMA wire surface of the SMA wire with a nominal diameter of 0.5 mm for two different etching parameter sets [155].

5.3 Pull-Out Test Sample Manufacturing

This research uses the pull-out test, whose theoretical background is described in section 2.2, to analyze the force transfer mechanisms between the SMA wires and the surrounding polymer matrix. In order to determine the influence of selective electrochemical etching of the SMA wire surface on the force transfer for the different surface structured SMA wires (section 5.2.1), the mechanical laboratory pull-out test is performed. In addition, μ CT *in situ* pull-out tests were performed to gain deeper insights into the interfacial failure processes between the surface structured SMA wire and the polymer matrix. The aims and strategies of the two set ups were described previously

in section 4. The two different pull-out tests used in this research are explained in sections 6.2.1 (mechanical laboratory pull-out) and 6.3.1 (μ CT *in situ* pull-out test). The main differences between the two set ups are:

- The sample dimensions, the pull-out samples are schematically illustrated in Figure 9 and Figure 16.
- The optical observation methods, stress optics was used to observe and analyze the mechanical laboratory pull-out and μ CT was used for the μ CT *in situ* pull-out test
- The force was applied continuously in the mechanical laboratory pull-out test, whereas in the μ CT *in situ* pull-out test, the force was increased in increments.

The samples for the two pull-out test set ups are produced with the same process but with different sample dimensions. The SMA wires in the pull-out samples must be aligned in z-(force) direction. Misalignment of the SMA wires in the pull-out samples can cause transverse stresses that can affect measurement accuracy and reproducibility, as described in section 2.2. The samples must also be void-free and pre-delamination by the curing process must be strictly avoided. The pre-treatment of the SMA wires has already been described in section 5.2. The pull-out samples were cured in both cases, as described in section 5.1. Following the preparation process, sample quality control is carried out by visual inspection, as described in appendix A.2.

5.3.1 Manufacturing Process for Mechanical Laboratory Pull-Out Test Sample

A sample mold was developed to ensure the alignment of the SMA wires in the polymer matrix. The custom-made mold is a one side open steel frame in which a silicone mold is inserted. The two-part custom-made mold is shown in Figure 9. Small notches in the outer steel frame allow the SMA wires to be clamped in an aligned position. Five pull-out samples can be manufactured in one sample manufacturing process and one mold. After the SMA wires are fixed in the outer steel frame, the polymer matrix can be filled in, and the curing process described in section 5.1 can start. After curing, the custom-made mold is stress-free, disassembled, and the sample block is removed. The sample block was then cut vertically with the precision saw (DIADISC 6200, Mutronic, Präzisionsgerätebau GmbH&Co.KG, Germany) into individual pull-out samples with $50 \times 18 \times 9 \text{ mm}^3$ ($h \times w \times d$) in total sample dimension. The embedded SMA wire length was 50 mm.

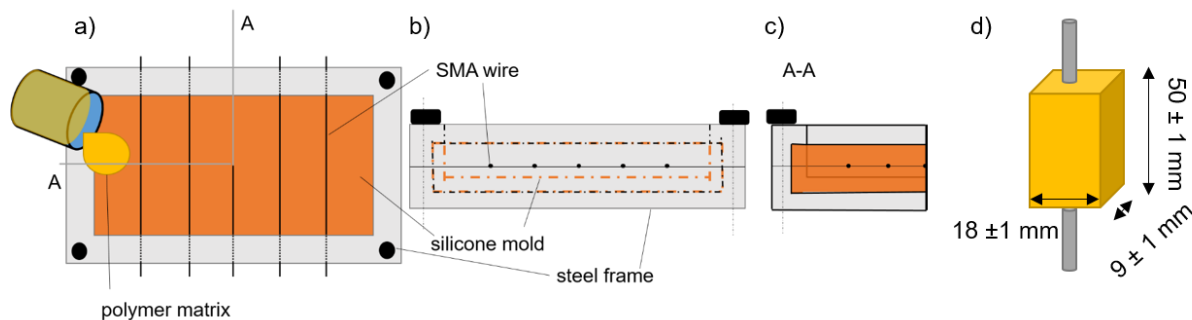


Figure 9: Sample preparation for the pull-out test: a) top view, b) front view, and c) A-A cross-sectional view d) schematic illustration of the sample dimensions. To ensure precise positioning of SMA wires inside the polymer matrix, the SMA wires were fixed using a one-side open steel frame, through which the polymer matrix was filled in. [130]

5.3.2 Manufacturing Process for *In Situ* Pull-Out Test Sample

The μ CT *in situ* pull-out test samples have additional specific requirements beyond those described above. The samples must be rotationally symmetrical to ensure uniform material absorption of the X-rays in all directions. Furthermore, the total width of the samples must not exceed 3 mm to remain within the FoV limitations of the high resolution X-ray μ CT measurement.

To meet these requirements, a new, customized sample mold was developed. The methodology involved using stereolithography (SLA) printers to 3D print positive molds. These molds were designed to contain a predefined opening for precise alignment of the SMA wire. After the curing process, silicone negative molds were produced from the positive molds to allow stress-free demolding of the samples. The SMA wire was inserted through the hole in the positive mold before the silicone was cast into the mold to ensure the hole was also located in the appropriate place. This allowed the accurate SMA wire positioning to be copied onto the silicone mold. The manufacturing process is illustrated in appendix A.3.

The polymer matrix was filled in the silicone mold and cured as described in section 5.1. To demold the samples, the silicone mold was cut open. Thus, the silicone molds were so-called lost molds. The 3D printing process allows various molds to be made quickly and cost-effectively. After demolding, no further sample processing was necessary. As mentioned previously, the sample quality was ensured through visual inspection (appendix A.2). The embedded part of the samples had a dimension of $3 \times 3 \times 15 \text{ mm}^3$ ($h \times w \times d$), a schematic illustration of the μ CT *in situ* pull-out samples

is shown in Figure 16. A rectangular mold was chosen because it is almost rotationally symmetrical and more accessible to manufacture than round samples.

6 Methods of Laboratory and Analytical Measurements

The methods are sectioned into the three parts described in section 4. Each part comprises mechanical testing, additional optical methods, and further analytical methods. As not all methods were used for all material combinations, an overview is shown in Table 4. The coloring indicates which methods are used in combination.

Table 4: Overview of the methods described in this chapter. Methods that are related to each other are highlighted with different colors to show which methods relate to each other.

	Alloy H Ø 1 mm	Alloy H Ø 1 mm + polymer matrix	Alloy H Ø 0.5 mm	Alloy H Ø 0.5 mm + polymer matrix
Mechanical testing	Stress-strain analysis	Laboratory pull-out test	Stress-strain analysis	Laboratory pull-out test
	DMTA			CT <i>in situ</i> pull-out test
	Actuator characterization			
Optical methods	SEM	SEM	SEM	SEM
	X-ray CT	Stress optics	X-ray CT	Stress optics
				X-ray CT
Analytics	Analysis of SMA wire surface morphology	Correlation of stress-optic with pull-out test data	Analysis of SMA wire surface morphology	Analysis of SMA wire surface morphology
		Shear stress analysis	DVC	Correlation of stress-optic with pull-out test data
		Crack energy analysis		Shear stress analysis
				Crack energy analysis
				DVC
				Segmentation

6.1 Understanding the Influence of the SMA Wire Surface Selective Electrochemical Etching Process on the Thermomechanical SMA Wire Characteristics and the Applied Surface Morphology

A comparative analysis was performed to evaluate the effects of selective etching on the thermomechanical properties of the SMA wires with a nominal diameter of 1 mm. In order to exclude the influence of the type of structuring on the characteristic SMA wire behavior, the three structure variants (Structure B1, Structure B2 and Structure B3, please refer to Figure 7) were compared with the as-delivered condition. The SMA wire was characterized using DMTA, stress-strain analysis, actuation test, SEM and μ CT as previously published in [130]. The non-embedded SMA wire with a diameter of 0.5 mm was not characterized in such detail; the analysis was reduced to the

stress-strain characteristics and the quantification of the applied surface morphology (Structures S1 and S2, Figure 8) by X-ray μ CT analysis.

6.1.1 Stress-Strain Analysis

The unique, strongly non-linear stress-strain characteristics of one-way effect SMA wires are explained in section 2.1. The plateaus described have certain characteristics and can vary depending on the SMA wire used. Stress-strain analysis of the SMA wire was divided into two test procedures: tensile and stress-strain test. Tensile tests were performed on the SMA wires to understand the stress-strain behavior of the SMA wire until failure. The stress-strain analysis stopped at a certain pre-strain to visualize the pseudoplastic effect. The test conditions for both tests were almost equal. The SMA wires were tested in a universal tensile testing machine, the Zwick RetroLine (Zwick-Roell GmbH & Co. KG, Ulm, Germany). The SMA wires were directly clamped in the pneumatic clamps with 2 bar and a textured surface to prevent slippage during the test. The SMA wires had a free test length of 90 mm and were pulled at a speed of 500 mm/min to a pre-strain of 4.5 %. These parameters were chosen following the work of [49, 85]. The detwinning of the SMA wire microstructure was to be induced as homogeneously as possible by rapid pulling. For the pre-strain test, ten SMA wires were strained for each investigated sample variant. The tensile test was carried out with a 400 %/min test speed. Five samples were tested per SMA wire sample variant. The data analysis was implemented using Python 3.7 (pandas, numpy, matplotlib, scipy stats).

6.1.2 Actuator Characterization Set Up

In order to generate a holistic investigation of the actuator potential of the SMA wires, a test device was developed at the Leibniz Institute for Composite Material GmbH (IVW) in which the SMA wires work against a specific spring stiffness [156]. The testing device has an integrated load cell that enables precise force measurement. In addition, the surface temperature can be monitored in real time using a thermocamera. Figure 10 shows an image of the experimental setup. The actuation test was conducted with a spring stiffness of 29 N/mm. The SMA wires were activated using joule heating with an applied electric current of 6 A. The SMA wire then starts to contract and work against the stiffness of the spring. One SMA wire previously pre-strained to 4.5 % per

variant was installed in the test device. The actuation tests are very time-consuming but provide a holistic view of the thermomechanical properties of the SMA wire since the actuation stresses and strains and the work actuation capacity can be determined. One sample per surface variant was measured for the SMA wire with a nominal diameter of 1 mm (as-delivered, Structures B1, B2 and B3). A starting SMA wire length of 90 mm was used. The joule heating was from RT to approximately 145 °C with a calculated heating rate of approximately 4.8 K/s. The shutdown criterion for this test was that no significant temperature change could be measured for a certain time period. The test was evaluated using Python 3.7 (numpy, matplotlib, re, math, pylab).

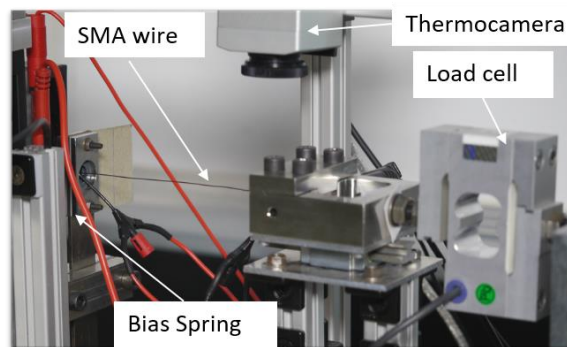


Figure 10: Image of the, at the IVW developed, SMA wire characterization test device. [156]

6.1.3 Dynamic-Mechanical-Thermal Analysis

DMTA analysis enables the precise determination of the transformation temperatures A_s and A_f . The analysis was done using the TA Instrument DMA 850 (TA Instruments, Inc., New Castle, USA). All samples were pre-strained to 4.5 % before testing. Four samples were investigated for each SMA wire variant (as-delivered, Structures B1, B2 and B3). The SMA wires were fixed in the DMTA using tensile clamps with a testing length of 15 mm. A preload of 0.1 MPa was applied to the SMA wires to ensure that the SMA wires were aligned. The SMA wires were heated in the DMTA from 20 to 150 °C with a 2 K/min heating rate. The lower restraint was movable, and as soon as the SMA wire experienced a thermal-induced phase transformation from the detwinned martensite to the austenite state, an axial contraction of the SMA wire occurred. The moment of the first movement can be considered as A_s temperature. When no more contraction can be measured, the phase transformation is complete, and A_f is reached. This means that the transformation temperatures can be read from the almost stress-free contraction of the clamped SMA wire. The transformation temperatures were then

determined using the TA instruments software TRIOS. The open source software Python 3.7 (numpy, matplotlib, re, math pylab) was used to illustrate the results.

6.1.4 Scanning Electron Microscope

Preliminary analysis of the surface morphology of the SMA wires was performed using the ZEISS ULTRA PLUS SEM equipped with the GEMINI column from Carl Zeiss Microscopy GmbH (Jena, Germany). This microscope included an energy-dispersive X-ray spectroscopy (EDX) analysis system supplied by Oxford Instruments. The chemical composition analysis by using EDX was performed at an accelerating voltage of 15 kV. A thin gold-palladium layer (< 10 nm) was deposited on the SMA wires by sputtering to examine the pulled-out SMA wires to visualize the epoxy residues on the surface.

6.1.5 X-ray Microcomputed Tomography

Two different analyses were conducted utilizing X-ray μ CT measurements:

The first analysis used X-ray μ CT to quantify the surface structure morphology of SMA wires. Parameters such as pit size, pit volume, pit depth and neighbor distance were evaluated. Detailed processing and analysis procedures are explained in sections 6.1.6, 6.3.3 and 6.3.4.

In the second analysis, μ CT measurements were used to observe *in situ* pull-out tests to obtain a high resolution volumetric perspective of the interfacial failure process.

All μ CT measurements were performed at Deutsches Elektronen-Synchrotron (DESY, Hamburg, Germany) at the high-energy materials science beamline P07 at PETRA III. Helmholtz-Zentrum Hereon operated the beamline. The number of projections was acquired with a rotational angle of 180°. The used detector was a Ximea CB500MG detector (Münster, Germany) with 7290 x 4500 pixels. Due to the detector size, a comparing large FoV can be scanned with a high pixel resolution. The parameters were adjusted for the different measurement sessions so that a consistent image quality could be guaranteed. Therefore, the parameters are summarized in Table 5.

The number of analyzed samples for quantifying the SMA wire surface morphology was at least one sample per configuration. Three samples per SMA wire surface variant were used for the μ CT *in situ* pull-out test.

Table 5: The parameter setting for the μ CT analysis done in this research for the SMA wire with a nominal diameter of 0.5 and 1 mm.

	Photon energy	Amount of projections	Pixel resolution	Exposure time	Binning	FoV	Magnification
Alloy H \varnothing 1 mm	55.75 keV	4800	0.673 μ m	500 ms	3x	1.8 x 1.4 mm ²	20 x
Alloy H \varnothing 0.5 mm	41 keV	2501	0.46 μ m	100 ms	-	3.6 x 2.1 mm ²	10 x

6.1.6 Rendering of Surface Area and Pit Morphology

Helmholtz-Zentrum Hereon Group Institute for Metallic Biomaterials reconstructed and analyzed the μ CT data. Before reconstruction, the pixels were binned. This was different for each measurement sequence and is included in Table 5. The resulting effective pixel size for each measurement series is also included. For reconstruction, a MATLAB script available at the beamline (R2020b, The MathWorks, Inc. Massachusetts, USA) was used [157]. The projection data were filtered with a median filtering (11-pixel kernel width) to reduce ring artifacts in the output data. The segmental reconstruction of the pits on the SMA wire surface was done using marsh cubes. The quantification of the SMA wire surface morphology is demonstrated in section 7.1. To identify the etched surface pits, all voxels segmented as NiTi and with a certain distance to the SMA wire length axis (closer than 250 μ m for the 0.5 mm SMA wire) were labeled. A local thickness transformation [158] was evaluated for the resulting mask, which was used to determine the diameter of the maximum inscribed sphere for the candidate voxels. This resulted in a density distribution. Only diameters of more than six voxels were considered individual pits for the statistical pit morphological analysis. The selective electrochemical etching process is described in section 5.2.1. Thus, multiple pits can be interlocked. The BoneJ thickness plugin in Fiji ImageJ [159] was used for meaningful segmentation of falsely connected pits. More information about pit segmentation is given in appendix A.4 and in [160]. Figure 11 shows the representative data analysis process. The reconstructed tomographic images are rendered to get a 3D volume view (1) and the surface pits are identified (2) and labeled (3).

The μ CT data was used to visualize the distribution of the segmented pits on the SMA wire surface in 3D and to demonstrate the omega-shaped pits in depth. Figure 12 compares the SEM micrographs with a μ CT projection slice and a 3D-rendered SMA wire volume with labeled pits. The parameters pit size (area), ten nearest neighbor distance,

pit volume and pit depth were considered to describe the selectively etched SMA wire surface in this research. The parameters were defined by Helmholtz-Zentrum Hereon Group as follows: The surface pit depth is described as the maximum sphere that will fit into each pit as determined by the BoneJ plugin. The distance between the ten nearest neighbors describes the distances between the determined pit centroids. The pit volume is defined as the convex mask around the identified pits. An analysis of the reproducibility of the description is given in appendix A.1, showing the analysis of four samples etched with Structure S1.

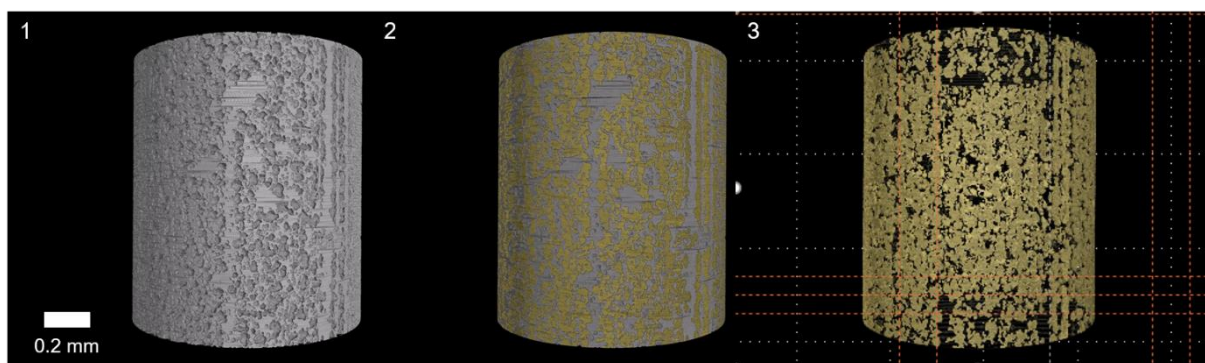


Figure 11: Representative example of the Structure B1 reconstructed and rendered tomographic images, showing the analyzed volume (1), the identified surface pits (2), and the segmented surface pits (3)

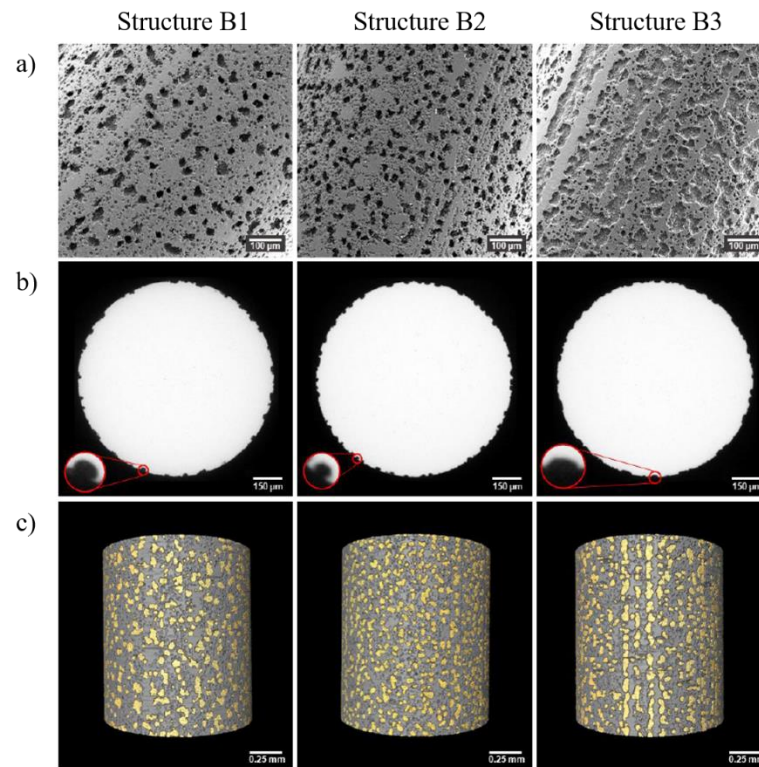


Figure 12: a) SEM micrographs showing the selective electrochemical etched SMA wire structured surface for the SMA wire, 1 mm, b) exemplary image slice of the reconstructed μ CT projection the reconstructed data results in a top view image stack along the SMA wire length axis, c) showing the identified pits for the different structured SMA wire surfaces on 3D renderings of the reconstructed SMA wire μ CT volumes. [130]

6.2 Understanding the Influence of the SMA Wire Surface Morphology on the Force Transfer between SMA Wire and Polymer Matrix

The mechanical laboratory pull-out test is performed to quantify the force transfer between the SMA wire and the polymer matrix and to verify it statistically. However, the statistical validation is limited by the high measurement effort. These tests were performed on samples with both SMA wire diameters of 0.5 and 1 mm in the surface structuring variants described in section 5.2.1. The results were compared with the pull-out samples with SMA wire in the as-delivered condition. The results for the SMA wire with a nominal diameter of 0.5 mm are published in [155], and those for the SMA wire with a nominal diameter of 1 mm are published in [130]. The mechanical laboratory pull-out test is described with the additional optical methods used to understand the interfacial failure progression described in sections 6.1.5 and 6.2.2.

For analyzing the mechanical laboratory pull-out test, two different approaches were used to generate a further understanding: a shear-lag based approach described in section 6.2.3 and a fracture mechanic approach described in section 6.2.4.

6.2.1 Mechanical Laboratory Pull-Out Test

The mechanical laboratory pull-out test was carried out according to the methods presented in [49], using the sample dimensions and test conditions specified there. Nevertheless, improvements were made to the sample manufacturing process, which is described in detail in section 5.3.1. The tests were performed in the Zwick RetroLine with a load cell of 10 kN. The load frame described in [49] was used for stress-free clamping of the embedded part of the sample. The mechanical laboratory pull-out set up is shown in Figure 13. The SMA wire is clamped in the upper pneumatic clamp jaw (clamping pressure 2 bar). A pre-load of 5 N is applied to the pull-out sample so that the polymer matrix is pressed against the load frame and thus, the sample is aligned. This is expected to reduce the transverse shear stresses. The extent to which transverse shear stresses occur depends primarily on the sample quality, as described in section 2.2. The free length of the SMA wire was set to 40 mm, following [49]. The 25 %/min test speed was selected according to [49], which correlated approximately with the transformation speed of an SMA wire that transforms utilizing joule heating. The force is introduced into the SMA wire and is then transferred from the SMA wire to the polymer matrix via the interface until interface failure can be observed.

The mechanical laboratory pull-out test was aborted by a force drop of more than 80 % or manually after an overall interface failure was detected with stress optics.

6.2.2 Stress Optics

During the mechanical laboratory pull-out test, an optical stress measurement technique based on photoelasticity was used to measure the force of the first interfacial failure between the SMA wire and the surrounding polymer matrix. Without stress optics, it is not possible to identify the first interfacial failure based on the curve progression of the measured force-displacement curve [161], as described in section 2.2. This technique has already been used by [13, 126, 127] on comparable samples to determine the first interfacial failure during mechanical laboratory pull-out tests between

SMA wire and polymer matrix, as described in section 3.5. Schematically, this is illustrated in Figure 13.

This measurement technique allows the qualitative observation of the built-up and release of internal stresses in the pull-out sample during the loading, as exemplified in Figure 14. The distribution of interfacial stresses and the resulting propagation of interfacial failure during the pull-out test can be observed visually. However, direct quantification of the applied interfacial shear and normal stresses is not possible within this test set up, since the measurement and the description of the stress distribution in the interface is complex and the optical observation only illustrates the distribution of the stresses and not the amount. The first interfacial stresses are expected to occur at the SMA wire entry into the polymer matrix, as discussed in section 3.5. The force transfer between the SMA wire and the polymer matrix can be detected using a stress optic, in which a bright point indicates the occurrence of stresses during the loading process (1). Subsequently, the shift of the interfacial stress can be observed (2). The interfacial stresses first movement during the pull-out test is interpreted as the first interfacial failure. At time point (1), the first occurrence of the interfacial shear stresses can be observed. The propagation of the interfacial shear stress occurs along the SMA wire length axis (3) until a complete interfacial failure is achieved and no further force transmission, besides some frictional effects, is expected (4).

In this research, a linear polarizer and an ultra-high-speed camera, the Motion v2512 from Vision Research in Wayne, USA, operating at a frame rate of 1000 frames per second, were used for this purpose. Data analysis was performed using software from Stemmer Imaging AG in Puchheim, Germany.

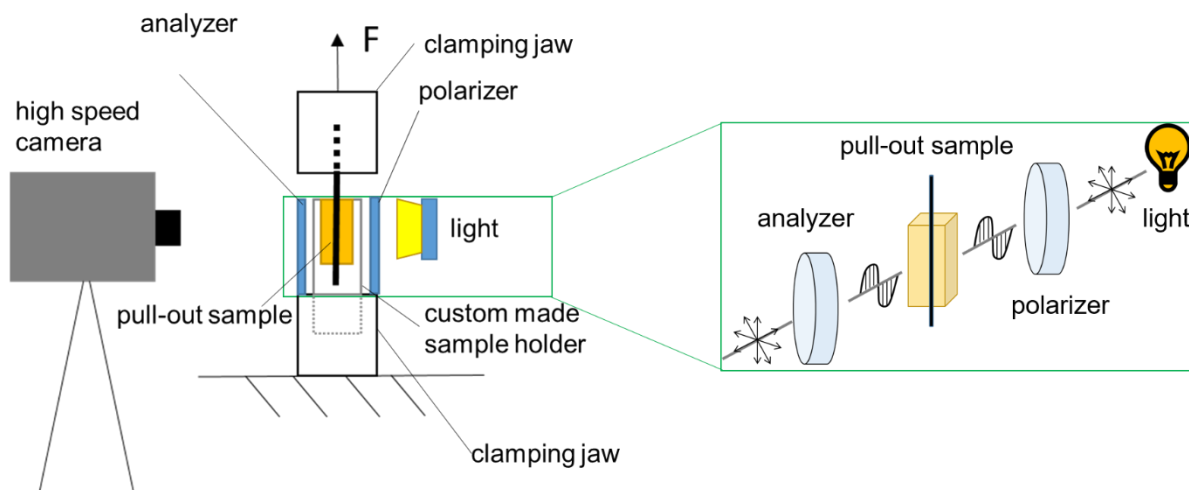


Figure 13: Schematic description of the pull-out set up combined with stress optic (left) and schematic description of stress optic (right) [49]

A Python (3.9) script developed at the IVW was used to analyze the recorded stress optic movie files. The script enables the correlation of the different recording rates from the universal testing device, which records force over time, with the high-speed camera, which collects image files over time. The script can directly correlate the evolution of the force over time and the optical change of the stresses in the sample. The first interfacial failure was chosen as the point at which stress relief was first observed along the interface, at the SMA wire entry into the sample (see Figure 14). The correlation was checked visually by comparing the complete interfacial failure, clearly visible from the force-time curve, with the movie files. The correlation showed a very good agreement. Although the evaluation of the failure progress at the interface was already largely automated, a certain subjective error cannot be ruled out, as the evaluator assessed the stress relief visually. However, the qualitative comparison is admissible since all samples were evaluated similarly.

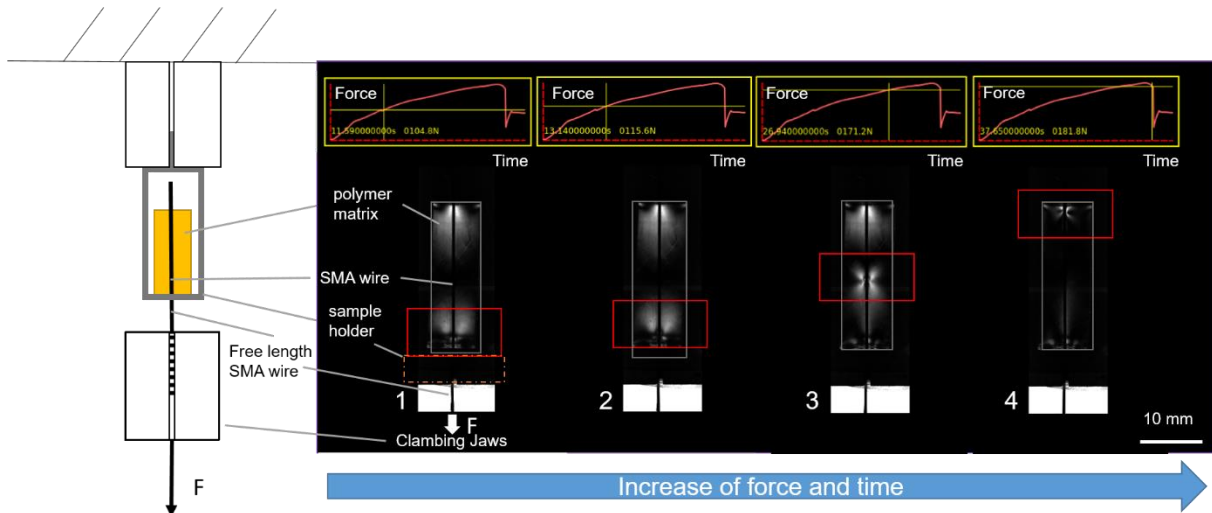


Figure 14: Exemplary visualization of the stress-optical observation of the failure progress during the mechanical laboratory pull-out test. On the left, the pull-out test is shown schematically. Then, the front view of the specimen from the optical stress observation is shown, which is subjected to a higher load from left to right. The failure progress can be observed by means of the light spot (highlighted with the red area) in the pull-out sample. [130]

6.2.3 Model Description of the Force Transfer by Using Greszczuk

The model description of the interface between fiber and polymer matrix is an open research topic that has been pursued for more than 30 years, as described in section 2.2. The different approaches and models used to characterize interfacial failure, particularly the challenges associated with describing the interfacial strength when dealing with a highly nonlinear SMA wire rather than a stiff carbon/glass fiber, were discussed in detail in section 3.

This research calculated the interfacial shear stress (σ_{shear}) between the SMA wire and the polymer matrix according to the Greszczuk model [50]. Greszczuk assumes that no radial effects must be considered for an axisymmetric linear elastic model. The strain and stress applied to the fiber by the externally applied load are fully transmitted via the interface. The shear stress distribution at the interface is non-uniform along the embedded length (z-direction) due to the free end of the SMA wire, which leads to excessive stresses near the entry point of the SMA wire into the polymer matrix. Various authors have used Greszczuk's model for similar shear stress analyses [49, 118, 162]. The model is based on the shear-lag theory in combination with pull-out testing.

The basic idea is to consider only an element of the embedded SMA wire and to equilibrate forces at this element.

According to Greszczuk [50] the interfacial shear stress in z-(force) direction is:

$$\sigma_{\text{shear}}(z) = F_w \frac{\alpha}{2\pi r} [\coth(\alpha L_e) \cosh(\alpha z) - \sinh(\alpha z)] \quad (1)$$

$$\alpha = \sqrt{2\pi \frac{G_m}{\left(\frac{r}{D}\right)} \left(\frac{1}{\pi r^2 E_w} - \frac{1}{\pi D^2 E_m} \right)} \quad (2)$$

F_w : force of the first interfacial failure [N],

α : material dependent variable,

G_m : calculated shear modulus of the polymer matrix,

r : SMA wire radius,

D : depth of the surrounding polymer matrix without the SMA wire diameter,

L_e : embedding length,

E_w : tensile modulus SMA wire (martensite, pseudoplastic state),

E_m : tensile modulus polymer matrix,

z : position along the SMA wire length axis.

The model is also used to predict the influence of the different pull-out sample sizes in this research work on the resulting shear stress in the interface (appendix A.11). A Table of the parameters chosen for every test is given in appendix A.9.

6.2.4 Analysis of the Surface-Dependent Stress Needed for Failure in the Interface between SMA Wire and Polymer Matrix

Another simplified approach to evaluating the interfacial failure characteristics between SMA wire and polymer matrix is a fracture mechanics based approach, as explained in sections 2.2 and 3. The previously described Greszczuk model (section 6.2.3, equation (1) and (2)) was used to transfer the measured force values into stresses to calculate stress-displacement curves from the data measured during the mechanical pull-out test. This was done in order to be able to take into account the different SMA wire diameters and the increase in cross-sectional area due to the structuring in the comparative study. The SMA wire embedding length for calculating the stress was assumed to be constant (initial length). The progressive interfacial failure results in a

change of the embedded SMA wire length during the pull-out test, this change was not taken into account. The resulting stress-displacement curves were analyzed up to both the point of first and complete interfacial failure and the corresponding area under the stress-displacement curve was quantified. During the pull-out test of an SMA wire embedded in a polymeric matrix, an inhomogeneous stress distribution appears due to localized length and diameter change during the pseudoplastic detwinning of the SMA wire. An advantage of the described simplified fracture mechanic approach is the inclusion of the displacement applied during the pull-out test. The measurement deviations and unknown measurement influences do not have to be described but are assessed as constant for the qualitative comparison. This allows the introduction of a new descriptive quantity, the surface-dependent stress and a direct comparison of the results obtained from the mechanical laboratory pull-out test with the SMA wire with nominal diameters of 1 and 0.5 mm. The introduction of this new descriptive quantity was necessary to compare all pull-out tests regardless of the SMA wire diameter used. However, the consideration also includes the part of surface-dependent stress needed for detwinning the free SMA wire. This part cannot be determined and calculated, but it is assumed to be constant since it was always the same SMA wire type and the same free SMA wire length. By keeping the relevant quantities constant, qualitative comparison is supported. A typical stress-displacement curve for a laboratory mechanical pull-out test for the samples with SMA wire (0.5 mm) with the as-delivered surface is shown in Figure 15. The calculated integrated area is marked green and includes the values from the pull-out test start to the stress where the first interfacial failure appears. The surface-dependent stress analysis was performed for all pull-out samples, and the mean values are considered in this research with the calculated 99 % confidence interval. The calculation was done using Python 3.9 (pandas, scipy, integrate, numpy).

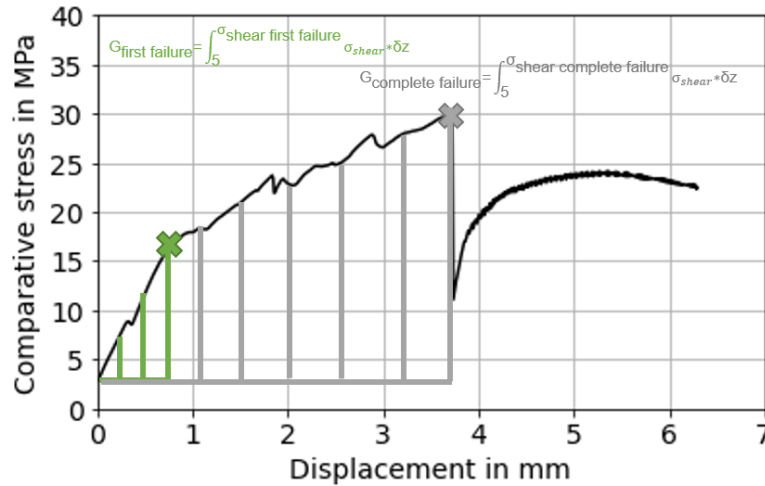


Figure 15: A representative surface-dependent stress-displacement curve for the SMA wire with a nominal diameter of 0.5 mm, the stress of first interfacial failure is marked with the green cross and the calculated integration area is marked green. The point of complete interfacial failure is marked grey and the calculated integration area is marked grey.

6.3 Understanding the Interfacial Failure Behavior of an SMAHC during Pull-Out Test and the Influence of the Thermomechanical Clamping due to Embedding the SMA Wire

X-ray μ CT was used to observe and analyze *in situ* the interfacial failure progress in the interface in high resolution and the *in situ* strain of the non-embedded SMA wire. The parameters chosen for μ CT are already described in section 6.1.5. The μ CT *in situ* pull-out test set up is described in section 6.3.1 and the *in situ* straining test is described in section 6.3.2. The real applied strain is analyzed using the DVC technique in section 6.3.3. In addition, a segmentation technique was used to analyze the interfacial debonding behavior for the ROI, as explained in section 6.3.4. The findings have partly already been published here [160].

6.3.1 *In Situ* Pull-Out Test

All μ CT *in situ* tests were performed using a load frame designed to accommodate simultaneous μ CT projections, as described in [163]. The load frame was originally developed for compression tests. The μ CT *in situ* pull-out tests demonstrated the feasibility of tensile tests in the load frame. The appropriate test set up can be seen in

Figure 16. The load frame consists of a connection to the air-bearing turntable of the beamline. A load cell, which can measure forces up to 200 N, was used. The polyetheretherketon (PEEK) outer shell, visible in Figure 16 (2), acts as an outer frame for the load frame. PEEK is an essential material for X-ray analysis because it is X-ray radiolucency [164]. The linear actuator (MA-35 Micro Actuator, Physik Instrumente (PI) GmbH & Co.KG, Germany) is attached to the PEEK outer shell, which can be used to apply the load to the sample. In order to perform the μ CT *in situ* pull-out tests, a new sample fixture was developed. As with the mechanical laboratory pull-out test, it is important to clamp the embedded part of the sample with as little clamping stress as possible. For this purpose, a PEEK sleeve was used. This PEEK sleeve has a central hole of 0.6 mm on the upper side, allowing the non-embedded SMA wire to be extended out of the PEEK sleeve. At the lower end, there is a transverse hole through the PEEK sleeve, which allows the PEEK sleeve to be firmly connected to the lower clamping. The free part of the SMA wire is fixed in a metal clamp made of high-strength aluminum with two grub screws. The overall clamping of the sample allows it to be aligned in the load direction when the load is applied.

For tomographic observation, the pull-out sample must be loaded incrementally. This means a force is applied and held until the sample is relaxed and image acquisition occurs. In addition, only a specific area of the μ CT *in situ* pull-out sample can be observed. The FoV is set to the entry area of the free SMA wire into the polymer matrix. Small load steps were chosen to facilitate the analysis and reproduce the interfacial failure in as much detail as possible. A listing of the μ CT *in situ* pull-out samples tested and the load increments chosen is given in appendix A.5. The number of samples for the μ CT *in situ* pull-out experiments was three per configuration. This was due to measurement time limitations and the test set up complexity.

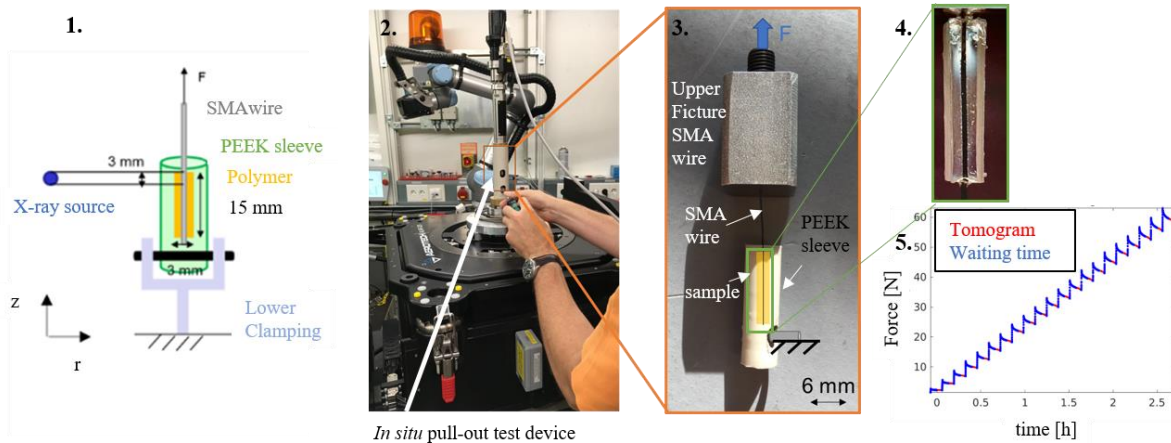


Figure 16: Schematic representation of the μ CT in situ pull-out test set up (1), the image of the test set up used (2), the clamping jaw holding the SMA wire and the PEEK sleeve (3), a picture of the sample with stress optics (4) and a representative load time progression during an entire μ CT in situ pull-out experiment (5). [160]

6.3.2 X-ray μ CT *In Situ* Straining of the Non-Embedded SMA Wire with Structured Surface

Investigating the influence of the external stress due to the thermomechanical clamping of the SMA wire by the enveloping polymer matrix is an important step toward the analytical modeling of active SMAHC.

To quantify the influence, it is important to perform the pull-out test in μ CT *in situ* and to strain the non-embedded SMA wire *in situ* in μ CT. For the *in situ* strained non-embedded SMA wire, two samples for Structure S1 were analyzed. Structure S2 was not included due to measurement time limitations. The applied forces are visualized in appendix A.5.

6.3.3 Digital Volume Correlation for Strain Analysis of the μ CT *In Situ* Data

The analysis of the radial and axial strain of the embedded SMA wire was done on the structured SMA wire surface for the defined ROI. The underlying principle is to utilize the surface pits as a speckle pattern, which allows the evaluation of their relative movement under applied loads. Instead of the applied speckle pattern, which is usually sprayed on, voxels describing a subset of the SMA wire surface structure, in this case, surface pits, are now clustered together and considered as a single data point tracked or related to the other data points. Those data points are limited to the surface area of the SMA wire in this research, and no data points in the inner volume of the SMA wire

are considered, as described in section 6.1.6. Thus, technically, it is a DIC on a cylindrical SMA wire surface, also called volumetric DIC. Helmholtz-Zentrum Hereon Institute (Dr. Stefan Bruns, Institute of Metallic Biomaterials) did the DVC analysis and the provided data was further processed in this research by using Python 3.9 (numpy, matplotlib, pandas, seaborn, math)

The macroscopic strain determined from the position change of the linear actuator was compared with the micromechanical strain from the DVC. HEREON's in-house software, CUDA/C++, was used to determine the deformation vectors of the reference scan. The software effectively deals with the DVC problem like a global variation problem. Compared to the volume of the SMA wire, the applied surface structure is relatively small. Moreover, an additional problem for the DVC is that the SMA wire moves out of the FoV on the edges of the image with a higher applied force. Accordingly, the total applied axial strain is larger than that observed in the FoV. To solve this problem, the FoV was extended with the load cell readings, and a comparison was made between the microscopic observations of the deviations from the ideal behavior. A solution to this problem was found by iteratively adjusting the boundary conditions concerning the previous solution. The evaluated image data are cropped at the image boundary in the axial direction so that 75 voxels are not considered at the image boundaries in the axial tensile direction, as they would move out of the ROI.

A surface structure was required for tracking, so this analysis cannot be performed for an SMA wire with an as-delivered surface. The DVC analysis published in [138] was adapted for the samples in this research, as described in detail in [160].

To understand the quantities axial (ϵ_{zz}) and radial strain (ϵ_{rad}), an analysis explanation is given schematically in Figure 17. Three weighted pit centers are considered as surface triangles for the radial strain and a new weighted center is calculated. The radial strain (ϵ_{rad}) describes the relative change between two load conditions of the distance of the weighted surface triangle center to the longitudinal SMA wire axis. Axial strain is described by the change of the center of the surface pits between two load levels in the direction of the applied tensile force. The axial strain is given according to the ϵ_{zz} component of the Green-Lagrange strain tensor of the derivatives calculated in [165].

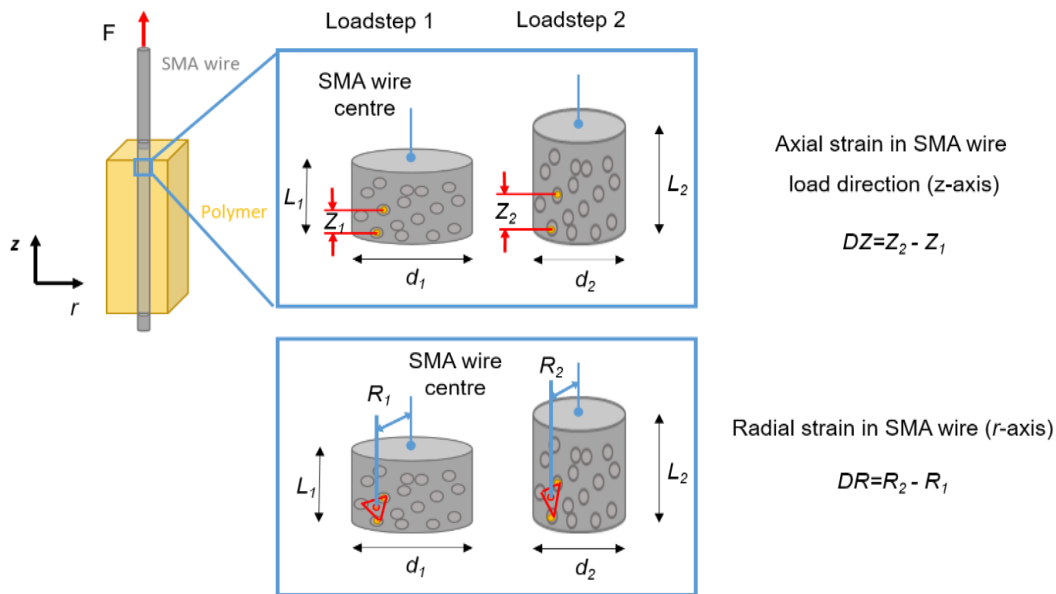


Figure 17: Schematically description of the DVC analysis parameter axial and radial strain.

The resulting interpretation of the DVC data can be divided into global and local strain values. The global strain describes an average value for ϵ_{rad} and ϵ_{zz} and can be calculated for each load increment over the analyzed ROI. The local strain is given in a visualization of the local strain distribution of both analyzed strains mapped onto the SMA wire surface. The global strain analysis was done for all tested samples, due to time restrictions, only two samples per configuration were analyzed with the local strain analysis.

6.3.4 Segmentation

Segmentation was performed on the 2D cross-sectional reconstructed images derived from μCT analysis to monitor the propagation of the delaminated area along the interface between the SMA wire surface and the polymer matrix to quantify the interfacial failure. For this purpose, the already processed μCT data, as described in section 6.1.6, was used. With μCT , a 2D image stack is acquired, which can be further processed by rendering to volume information. For the segmentation analysis, the reconstructed 2D image stack is used. The image stacks showed the top view of the μCT *in situ* pull-out sample and, thus, the cross-sectional area. The number of images in the analysis varied depending on the sample, as the defined ROI differed. The phases, delaminated area, SMA wire cross-sectional area and polymer matrix for each 2D image along the SMA wire length axis in the ROI were segmented for the analyses. Thus,

the development of the interfacial delaminated area and the change of the SMA wire cross-sectional area along the SMA wire length axis for the observed area can be described. This segmentation can be performed for each load step and the associated image stack, allowing the results to be visualized as a function of axial position and load increment. To achieve the phase segmentation, the free WEKA (Waikato Environment for Knowledge Analysis) segmentation [166] Fiji ImageJ software [167] plugin was used and trained. This tool is a collection of machine learning algorithms that work on pixel-based segmentations. The training data can be 2D or 3D images and is not limited to grayscale images. For analyzing 2D images, different training features can be included in the image processing. In this research, the training features Gaussian blur filter, Hessian, Membrane projection, Sobel filters and difference of Gaussian were used. The features were chosen by evaluation. The segmentation process is described in Figure 18. Pixels were color-coded to individual images' phases to train the segmentation. This process was repeated until the image stacks automatic coloring corresponded to the visual assignment phases. An image stack consisting of only three colors was achieved as an output. Everything segmented as polymer matrix was red colored, the assigned SMA wire was green colored, and the delaminated area was purple colored. Thus, the grey value image stack with histogram became one in which only three colors existed. This process was performed consistently in the same manner for the different samples and the load levels considered. The segmentation results were compared with an automatic segmentation of the most prominent feature, the SMA wire, and showed good agreement. The segmentation values shown are not intended to be absolute values since no error analysis was performed and the assignment of the pixels to the individual phases is affected by scan artifacts. However, since this problem occurs in all projections considered and the evaluation workflow remains constant, a qualitative development of the segmented phases can be derived from the segmentation. A Python 3.9 (cv2, numpy, os, pandas) script was used to quantify the phases by counting the number of pixels with a specific color. This number can be multiplied by the pixel size of the μ CT measurements, and the phase areas can be determined. The pixel size is already given in section 6.1.5. Segmentation analysis was limited to the μ CT *in situ* pull-out samples with Structure S1 due to time restrictions.

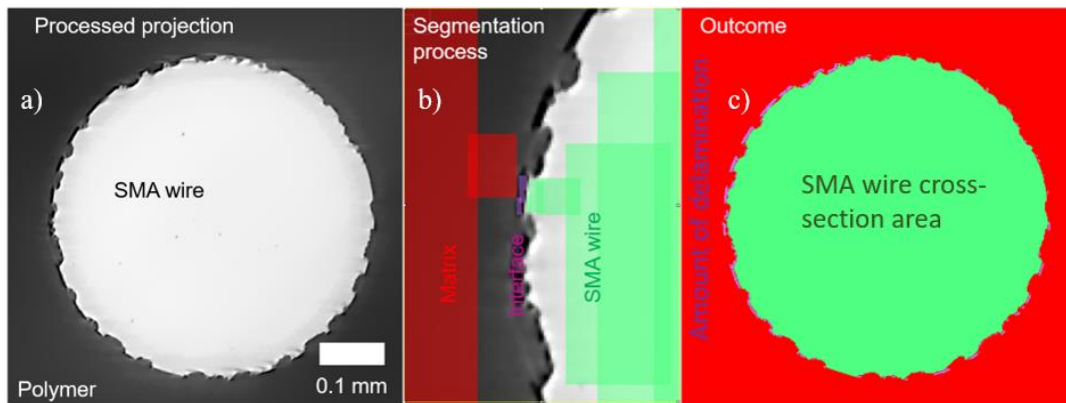


Figure 18: Workflow of the image segmentation technique as an example of one representative image out of an image stack for a certain load. a) Exemplary projection of the analyzed image stack, indicating the selected phases, b) magnification of the image shown in a), describing the segmentation chosen for the analyzed phases, polymer matrix, interface and SMA wire, c) outcome image after segmentation process. [160]

7 Results

7.1 Characterization of the Thermomechanical Characteristics of the SMA Wire and SMA Wire Surface Morphology Description before and after Selective Electrochemical Etching Process

Different characterization methods were used to understand the influence of the selective electrochemical etching of the SMA wire surface on the SMA wire thermomechanical characteristics and surface morphology, as described in section 6.1. The results are divided into the SMA wire with a nominal diameter of 1 and 0.5 mm, followed by a first discussion of the findings.

7.1.1 SMA Wire with a Nominal Diameter of 1 mm

SMA Wire Surface Morphology Description

EDX analysis was used to understand the chemical composition of the SMA wire surface before and after selective electrochemical etching. By comparing the EDX analysis of the SMA wire with an as-delivered SMA wire surface with that of an exemplary SMA wire with a structured surface (Structure B3), a decrease in the Ni content on the SMA wire surface can be observed. The results can be seen in Figure 19. The as-delivered SMA wire surface shows a uniform Ni and Ti distribution at the surface. The Ti distribution is homogenous for the structured SMA wire surface, but the amount of Ni is reduced. So, a selectivity for Ni can be demonstrated. While the thin native TiO₂ layer covering the untreated SMA surface cannot be detected by EDX, the oxide that forms from the etched sites is thicker and can, therefore, be identified. This occurs due to the nonlinear dynamics of its formation and dissolution as well as the roughness of the underlying surface that results in a strong O signal for the etched SMA wire surface. The ratio of Ni to Ti in the analyzed SMA wire surface for the different SMA wire surface variants was 1.21 for the as-delivered (1.23 manufacturer data sheet), 0.98 for Structure B1, 0.93 for Structure B2 and 0.88 for Structure B3 (Table 3).

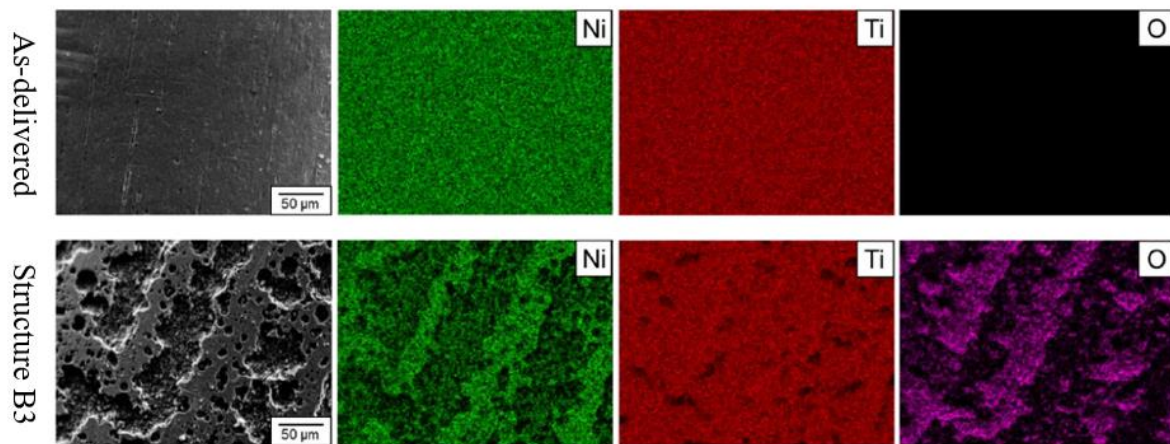


Figure 19: SEM and EDX analysis of the SMA wire with an as-delivered surface in comparison to SMA wire with a structured surface (Structure B3). [130]

The structured SMA wire morphology surface was quantified using μ CT as described in sections 6.1.5 and 6.1.6. The resulting SMA wire surface morphology depends on the parameters chosen during the selective electrochemical etching process. The surface morphology describing parameters pit size, pit volume, ten nearest neighbors and pit depth was chosen. The parameters can only be described within the selected pixel resolution, thus defining the results' accuracy. The description of the structured SMA wire surface morphology for all structure variants is shown in Figure 20. The different structured SMA wire surfaces vary mainly in the depth of the surface pits. As mentioned in section 5.2.1, the SMA wires resulting surface morphology predominantly depends on the phase distribution (Ni and Ti) on the SMA wire surface and the etching parameters chosen. Due to the selective etching process, it is not possible to change only one SMA wire surface morphology parameter since their distribution is influenced by each other. Even if the characteristics of the SMA wire surface morphologies of the different variants differ in parts, Structure B1 and B2 achieve a comparable surface enlargement of 1.5 compared to the as-delivered SMA wire surface. Structure B3 has a slightly lower surface enlargement of 1.3 than the as-delivered SMA wire surface. Structure B1 was etched using longer and weaker pulses, resulting in a broad and evenly distributed pit formation. Using a constant current in the etching process, which was used by Structure B3, a widening and overlapping of the individual surface pits can be generated.

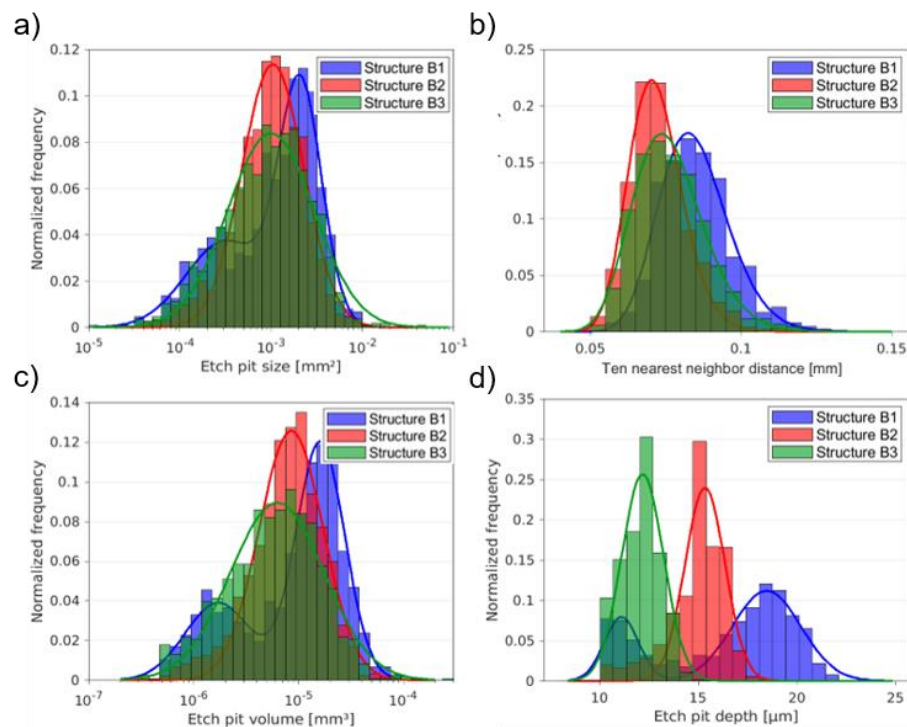


Figure 20: μ CT data analysis of the SMA wire with a nominal diameter of 1 mm for the chosen describing surface morphology parameters: a) Etch pit size, b) Ten nearest neighbor distance, c) Etch pit volume and d) Etch pit depth. (partly published in [130])

Non-Embedded SMA Wire Stress-Strain Characteristic

To understand the stress-strain characteristics of the chosen SMA wire, two different analysis methods described in section 6.1.1 were used. Figure 21 shows the calculated mean stress-strain curve for the different structured SMA wire surfaces: a) for the pre-strain test and b) for the tensile test. Additionally, the SMA wire diameter for each variant can be measured using the μ CT data and calculating a mean value over the measured length. The diameters used are shown in appendix A.9. This allows the occurring stresses to be calculated precisely. Only the mean value curves are shown in Figure 21 to present the data clearly and concisely. The mean value curves plus the calculated confidence interval curves for all four tested SMA wire surface variants can be found in appendix A.12 for the pre-strain test.

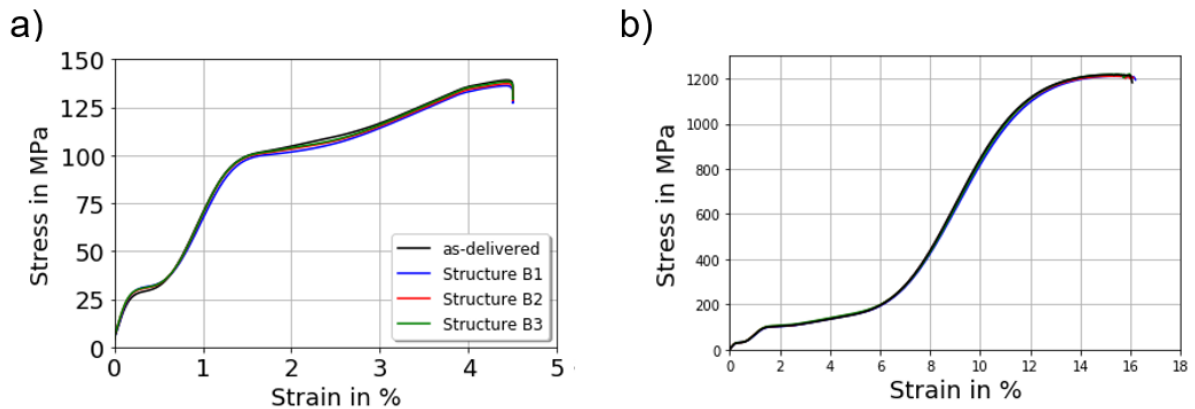


Figure 21: Calculated mean values for the stress-strain characteristics of the SMA wire with a nominal diameter of 1 mm for different surface morphologies, a) pre-strain test, b) tensile test. [130]

The expected typical SMA wire stress-strain characteristic, as described in section 2.1, can be seen. The pre-strain stress-strain curve a) was taken to analyze the two visible plateaus. Both curve progressions (Figure 21, a) and b)) show a load drop at the end of the test, which is caused by the test device regulation. The R-phase is observed for small strains below 0.56 %, and the martensite detwinning transformation is visible from 1.1 to 4.5 % axial strain. The tensile test b) confirmed the characteristic stress-strain behavior. Additionally, it shows another elastic region of the detwinned martensite, which starts at approximately 6 % strain. The tensile test shows that the average ultimate stress value is comparable for all tested SMA wire surface variants. The values are visualized in Table 6. If the confidence interval is included, no significant change in ultimate stress due to the SMA wire surface structuring can be detected. The characteristic shape of the observed stress-strain curve is constant for all analyzed SMA wire surface variants, which indicates a reproducible and homogenous SMA wire surface structuring due to the selective electrochemical etching procedure.

Table 6: Comparison of the mean values and the 99 % confidence interval of the ultimate tensile strength for the four surface variants: as-delivered, Structure B1, Structure B2 and Structure B3. (SMA wire, 1 mm)

	as-delivered	Structure B1	Structure B2	Structure B3
Ultimate tensile strength in MPa	1217.6 ± 4.9	1217.6 ± 3.06	1211 ± 1.44	1217.8 ± 2.57

The stress-strain characteristics of the pre-strained SMA wire (4.5 %) working against a spring with a specific stiffness, including the transformation temperature, were measured by the actuator characterization test described in section 6.1.2. The results can be seen in Figure 22, which shows the induced stress and strain by activating the SMA wire due to heating the SMA wire above A_f , which results in a contraction of the SMA wire and causes the SMA wire to work against the spring stiffness. Figure 22 a) shows the complete heating and cooling cycle for the one-time activation of SMA wires with different surface variants. Cooling was done by switching off the current and, thus, reducing the SMA wire temperature caused by convection. The Figure shows the increased stress and the decreased strain, indicating the contraction of the SMA wire during the heating cycle for all tested samples. The analyzed SMA wire was a one-way effect SMA wire. As explained in section 2.1, the one-way effect of SMA wire has no trained intrinsic effect. By activating the pre-strained SMA wire by applying thermal energy, the SMA wire contracts in its original shape before pre-straining. The stress-strain characteristic is influenced since the SMA wire works against a spring with a certain stiffness in this test set up. During the cooling cycle after reaching M_s , the spring induces again a pre-strain of the SMA wire dependent on the spring stiffness. That is why a small straining of the SMA wire in the cooling cycle is observable and the tested SMA wires are not contracting back to their original shape. The real SMA wire diameter measured by μ CT was used to calculate the stress values.

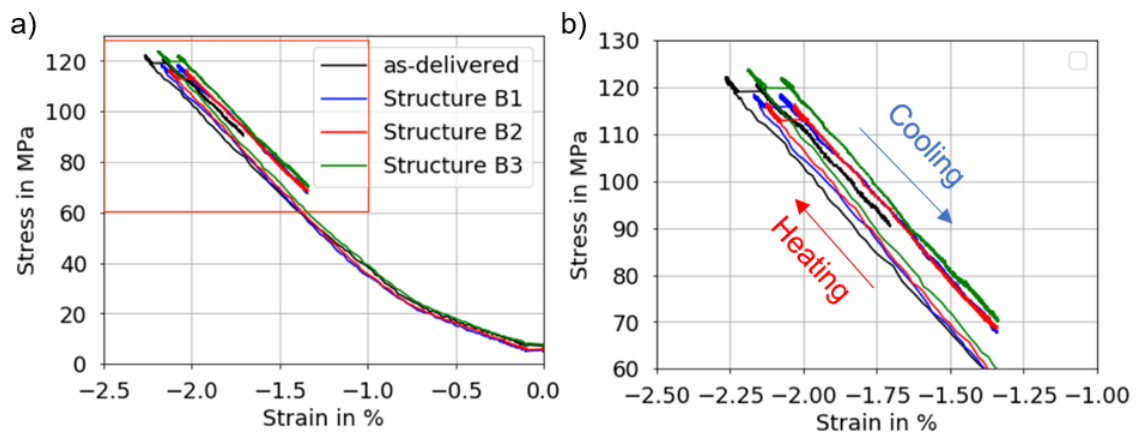


Figure 22: Actuation characteristics of the SMA wire with a nominal diameter of 1 mm for the four surface variants: as-delivered, Structure B1, Structure B2 and Structure B3, working against a spring: a) full actuation stress vs actuation strain diagram, b) detailed view of the red marked area. [130]

The measured results are summarized in Table 7. Minor differences between the SMA with different surface variants are visible. However, the induced work capacity by pre-straining the SMA wire is almost not influenced by structuring the SMA wire surface, as well as the maximum actuation stress. Since the actuation test is very time consuming, only one sample per configuration was tested, so no assumptions regarding a trend can be made.

Table 7: Results for the actuation test for the SMA wire with a nominal diameter of 1 mm for the four surface variants: as-delivered, Structure B1, Structure B2 and Structure B3. Showing the results for one sample per variant.

	as-delivered	Structure B1	Structure B2	Structure B3
Maximum actuation stress in MPa	122.2	118.6	116.7	123.9
Maximum actuation strain in %	-2.265	-2.168	-2.124	-2.189
Work actuation capacity in J	0.255	0.233	0.225	0.248
Induced work capacity in J	0.455	0.437	0.44	0.443
Work capacity retrieved in %	56	53.3	58	57.3

SMA Wire Phase Transformation Temperature

One essential characteristic of the SMA wire are the transformation temperatures, as described in section 2.1. To determine the transformation temperatures before and after surface treatment of the SMA wire, the DMTA analysis was used. Between the SMA

wire with an as-delivered surface and the structured SMA wire surface variants for A_s and A_f , there is no difference in the tolerance range specified by the manufacturer (please refer to section 5.2). The results are visualized in Figure 23.

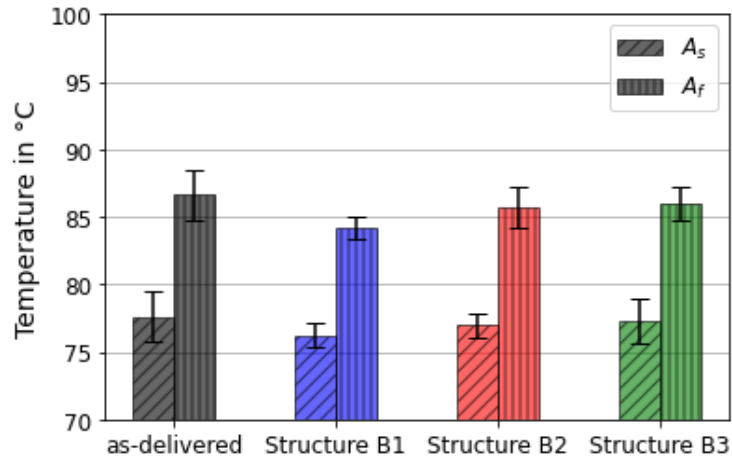


Figure 23: A_s and A_f for the SMA wire with a nominal diameter of 1 mm for the four surface variants: as-delivered, Structure B1, Structure B2 and Structure B3.

7.1.2 SMA Wire with a Nominal Diameter of 0.5 mm

SMA Wire Surface Morphology Description

The μ CT surface morphology analysis of the structured SMA wire (Structures S1 and S2) considered for the SMA wire with a nominal diameter of 0.5 mm is visualized in Figure 24. One of the main differences between Structures S1 and S2 is the distance between the ten nearest surface pits. This results in a different amount for the identified SMA wire surface pits for the two analyzed samples: for an evaluated length of 1.5 mm, 672 pits were identified for Structure S2 and 1212 pits were identified for Structure S1. Structure S2 has additional deeper and larger surface pits. By comparing the SEM images shown in section 5.2.1 (Figure 8) and correlating them with the μ CT analysis, another difference between the two SMA wire surface structures becomes clearer. Structure S2 has a simpler pit shape, whereas Structure S1 shows smaller pits in a hierarchical range. The larger pits have smaller pits inside, which results in a more complex shape.

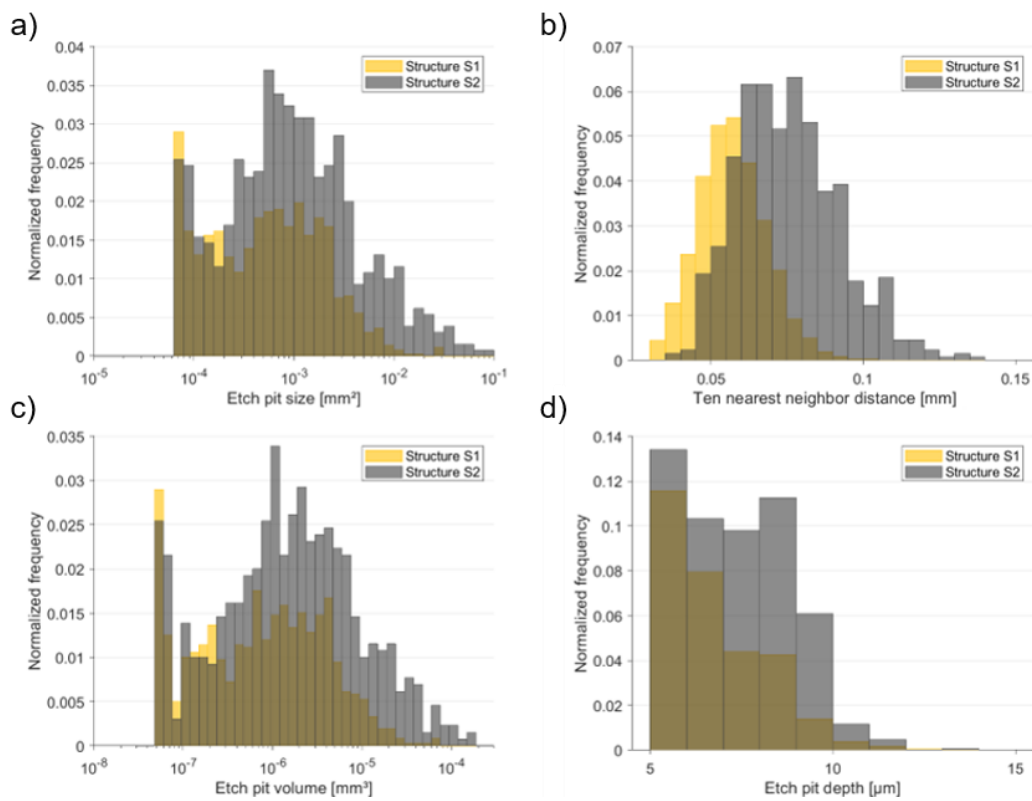


Figure 24: μ CT data analysis of the SMA wire with a nominal diameter of 0.5 mm for the chosen describing surface morphology parameters: a) Etch pit size, b) Ten nearest neighbor distance, c) Etch pit volume and d) Etch pit depth.

The shape of the surface pits for both variants can also be seen by looking at the top view cross-sections reconstructed slice-through tomography images of the μ CT data analysis. A representative cross-section of the two structured SMA wire variants is demonstrated in Figure 25. Comparing the μ CT data in Figure 24 and Figure 25 with the SEM images in Figure 8, the previously described differences can be visualized and quantified.

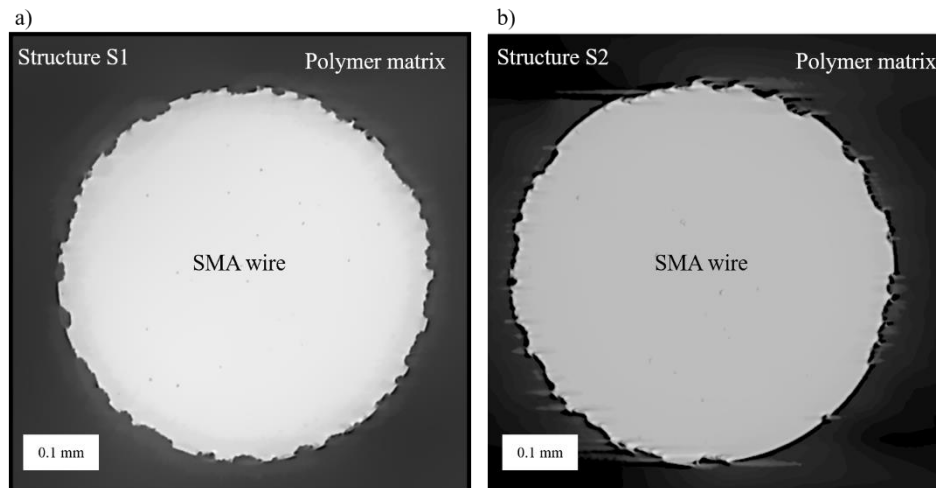


Figure 25: Representative top view cross-section reconstructed slice-through tomography image of a) Structure S1 and b) Structure S2

Non-embedded SMA Wire Stress-Strain Characteristic

The mean curve of the stress-strain characteristics of the non-embedded as-delivered SMA wire with a nominal diameter of 0.5 mm is demonstrated in Figure 26. Comparing this Figure (b) with Figure 21 shown in section 7.1.1, the two already described plateaus can be seen. The R-Phase is visible between 0 - 0.5 % strain and the detwinning plateau between 1.5 - 6 % axial strain. The ultimate tensile strength is 1276.98 ± 16.4 MPa, slightly higher than the SMA wire with a nominal diameter of 1 mm.

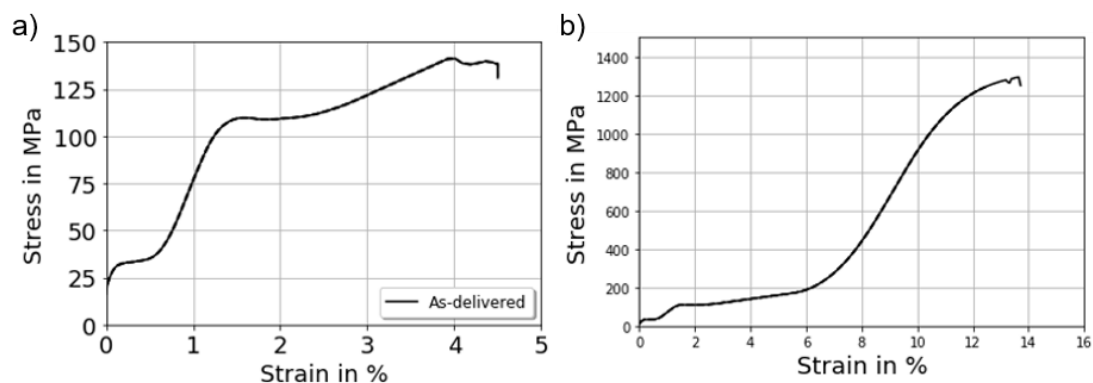


Figure 26: The calculated mean values from the tested data for the stress-strain characteristics of the SMA wire with a nominal diameter of 0.5 mm, a) pre-strain test, b) tensile test.

As explained in section 6.3.2, non-embedded SMA wires were *in situ* strained with μ CT analysis. Using the DVC analysis described in section 6.3.3, the global axial and radial strain values for the analyzed SMA wire volume are visualized in Figure 27 during the

μ CT *in situ* straining for one exemplary sample. The progression of the global axial strain shows a constant increase with higher load. At a stress level of 86.15 MPa, an anomaly in the curve progression is visible, due to the small data set, the reason for the anomaly remains unclear. The global radial strain decreases with increasing the applied load. At 90.28 MPa, likewise, an anomaly in the curve global radial strain progression is visible. No detwinning plateaus are visible for the global axial strain, which can be attributed to the limited FoV and the discrepancy of the testing speed, as explained in section 2.1.

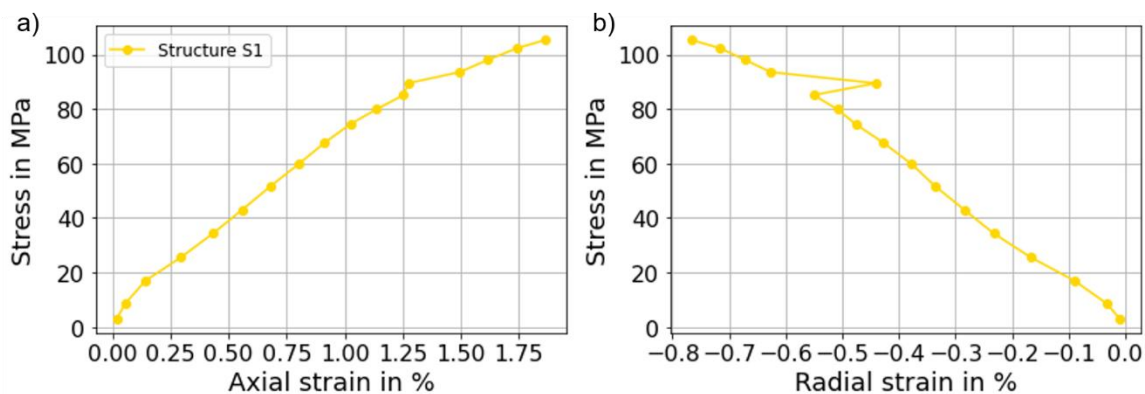


Figure 27: The global axial a) and radial b) strain during the μ CT *in situ* pre-strain test for the SMA wire with a nominal diameter of 0.5 mm. The analysis of the strain values was done by DVC analysis.

7.1.3 Discussion of the Influence of the SMA Wire Surface Modification to the Non-Embedded SMA Wire Thermomechanical Characteristic Behavior

The chemical analyses of the SMA wire surface, demonstrated in section 7.1.1, indicate a change in the chemical composition. The selective etching process shows a selectivity for Ni-rich areas. The etching process can be applied to different SMA wire diameters but is limited to an SMA wire with only a thin oxide layer.

With the μ CT analysis, the surface morphology can be quantified and characterized, which is limited by the applied chosen pixel size. The surface enlargements due to the surface structuring can be determined. Using the μ CT analysis, the shape of the introduced surface pits can be analyzed. Omega-shaped pits can be found in all analyzed SMA wire surface structures but are not regularly found. The shape and the pit distribution are not uniform in circumferential SMA wire direction regarding the top view images shown in Figure 12 and Figure 25. Microscopically, the distribution of the sur-

face pits is non-homogenous. The analysis of the SMA wire surface using the described surface parameters indicates a macroscopic homogenous distributed and reproducible etching over the measuring length. The applied surface structure is controllable by the etching parameters, and reproducibility only depends on the SMA wire chemical composition on the surface. In appendix A.1, an additional reproducible test is shown for an exemplary sample to support the findings. The etching structures on the SMA wire surface through selective electrochemical etching are not transferable from the SMA wire with a nominal diameter of 1 mm to the one with 0.5 mm (please refer to Figure 20 and Figure 24). This is because the selective electrochemical structuring process had to be adapted to the smaller SMA wires and new etching parameter settings had to be defined. In addition, the surface structure can be controlled, but individual parameters cannot be adjusted separately, as the structuring process is not a linear system. The surface topography depends on the interaction of energetic and kinetic aspects, i.e. both the energy states on the surface and the passivation kinetics. The applied SMA wire surface structures for the SMA wire with a nominal diameter of 1 mm are quite similar. Structure B1 and B2 differ mainly in the etching depth. Structure B3 shows more interconnected pits on the SMA wire surface than Structure B1 and B2. For the SMA wire with a nominal diameter of 0.5 mm, Structure S1 and S2 differ distinctly. Structure S1 (0.5 mm) shows a higher pit density with smaller pit sizes and a more complex interaction between the surface pits, as described in section 7.1.2. From the applied type of surface structure morphology of the two different SMA wires considered, Structure B1 (1 mm) and S1 (0.5 mm) are the most alike.

Full thermomechanical characterization was done for the SMA wire with a nominal diameter of 1 mm. Including the findings of the DMTA test and the stress-strain analysis with the actuation characterization test, the selective electrochemical etching process does not influence the SMA wire thermomechanical characteristics. No change in the stress-strain curves of the as-delivered SMA wire compared to the SMA wire with a structured surface could be measured (Figure 21). The relation between the characterization and the optical methods indicates that the surface treatment of the SMA wire ensures macroscopic homogenous structuring along the entire etching length of the SMA wire. The surface treatment or the structuring process does almost not influence the working capacity of the SMA wire tested. Those findings are assumed to be transferable for a comparable SMA wire treated with selective electrochemical etching. One reason for this assumption is that only a small part of the SMA wire's overall volume is

etched. No influence on the resulting thermomechanical SMA wire characteristics could be found for the different etchings applied to the surface of the SMA wire with a nominal diameter of 1 mm. The tensile test was also applied to verify if the SMA wire with a nominal diameter of 0.5 mm shows the same stress-strain characteristics as the SMA wire with a nominal diameter of 1 mm. The analysis indicates similar stress-strain characteristics with minimal deviations. The surface of the SMA wire with a nominal diameter of 0.5 and 1 mm in the as-delivered condition is comparable. Both have a polished surface with few drawing grooves due to the SMA wire manufacturing process.

7.2 Characterization of the Influence of the SMA Wire Surface Morphology on the Force Transfer between SMA Wire and Polymer Matrix

In the following the results of the micromechanical interface analysis using the mechanical laboratory pull-out test for the SMA wire with a nominal diameter of 1 mm (section 7.2.1) and 0.5 mm (section 7.2.2) are demonstrated. All samples were tested with the methodology described in section 6.2. In section 7.2.3, a first discussion of the results is presented.

7.2.1 SMA Wire with a Nominal Diameter of 1 mm

The progression of interfacial failure can be observed using stress optics, allowing quantification of the force at first failure, as shown in section 6.2.2 (Figure 14). Due to the quantification of the SMA wire surface morphology as described in section 7.1, the increase of the surface area caused by the selective electrochemical surface structuring process is measurable. The mechanical laboratory pull-out test results are visualized in Figure 28, showing the force of the first interfacial failure in relation to the surface enlargement, which also increases the contact area between the SMA wire and the polymer matrix. The calculated mean force of first failure values are given along with the 99 % confidence intervals for all SMA wire surface variants considered.

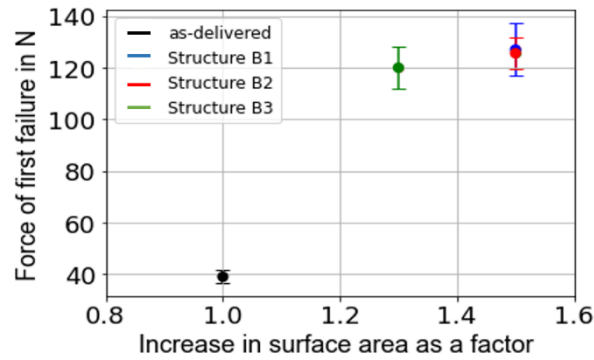


Figure 28: The results of the mechanical laboratory pull-out test for the SMA wire with a nominal diameter of 1 mm are demonstrated. The mean values of the force of first failure for all tested structured SMA wire surface variants and the as-delivered SMA wire over the increase in surface as a factor is shown. The error bars represent the 99 % confidence interval.

The first interfacial failure was measured for the as-delivered SMA wire at a force of 39 ± 2.4 N. In contrast, applying selective electrochemically induced surface enlargement to the SMA wire resulted in an increased force at first interfacial failure. For Structure B1, a first failure at 126.9 ± 10.2 N related to an SMA wire surface enlargement by a factor of 1.5 could be observed. An increase of 3.3 times compared to the as-delivered SMA wire in the force of the first failure could thus be demonstrated. The surface enlargement of Structure B2 is identical to Structure B1. For Structure B2, a force of first failure of 125.5 ± 6.1 N was measured. With 1.3 times the surface enlargement of Structure B3, it is slightly smaller than the other surface structures considered. The force transfer is comparable with 119.9 ± 8.1 N. Considering the 99 % confidence intervals, no difference between the structured surfaces can be detected.

The 99 % confidence interval for the calculated mean values for the force of first interfacial failure for the different SMA wire structure variants differs. Structure B1 shows the highest 99 % confidence interval with 10.2 N, an 8 % difference from the calculated mean value. The SMA wire with the as-delivered surface shows a higher reproducibility with only a 6.2 % difference from the calculated mean value.

The comparative stresses were calculated as described in section 6.2.3 (eq. (1) and (2)). The calculated comparative stress-displacement curves during the pull-out test for all tested sample variants are given in Figure 29. The evaluated interfacial shear stresses for the first failure, according to [50], are highlighted in this Figure. As described in section 6.2.4, the increase in surface area and the crack growth after this point is not considered in the calculation of the comparative stresses. The comparative

stress is only a relative quantity introduced for a better comparison between the different sample variations. The parameters chosen for the shear stress calculation are summarized in appendix A.9. The progression of the curves is influenced by the stopping criteria of the test device, which was either manual by the maintainer when the stress optic showed a complete interfacial failure or by the parameters defined in the test device. However, all curves show a complete interface failure. The captured curves match the typical pull-out test curve progression described in section 2.2. The progression of the curves for the structured SMA wire variants shows a high degree of similarity between all etched variants. Differences in the stress of the first interfacial failure, particularly, are observed within the same surface variant, resulting in a standard deviation, as already mentioned. The stress distribution of the marked first failure points in Figure 29 shows that the point of first failure is not apparent from the stress-displacement curve. After the first failure, the applied interfacial shear stress can still be transmitted until the point at which the entire interface has failed, and a sharp drop in the stress curve can be seen. Compared to the as-delivered stress-displacement curve progression after the first interfacial failure, a higher force-bearing capacity for the SMA wires with a structured surface can be observed. The stress needed to provoke a complete interfacial failure is substantially higher for the SMA wire with a structured surface.

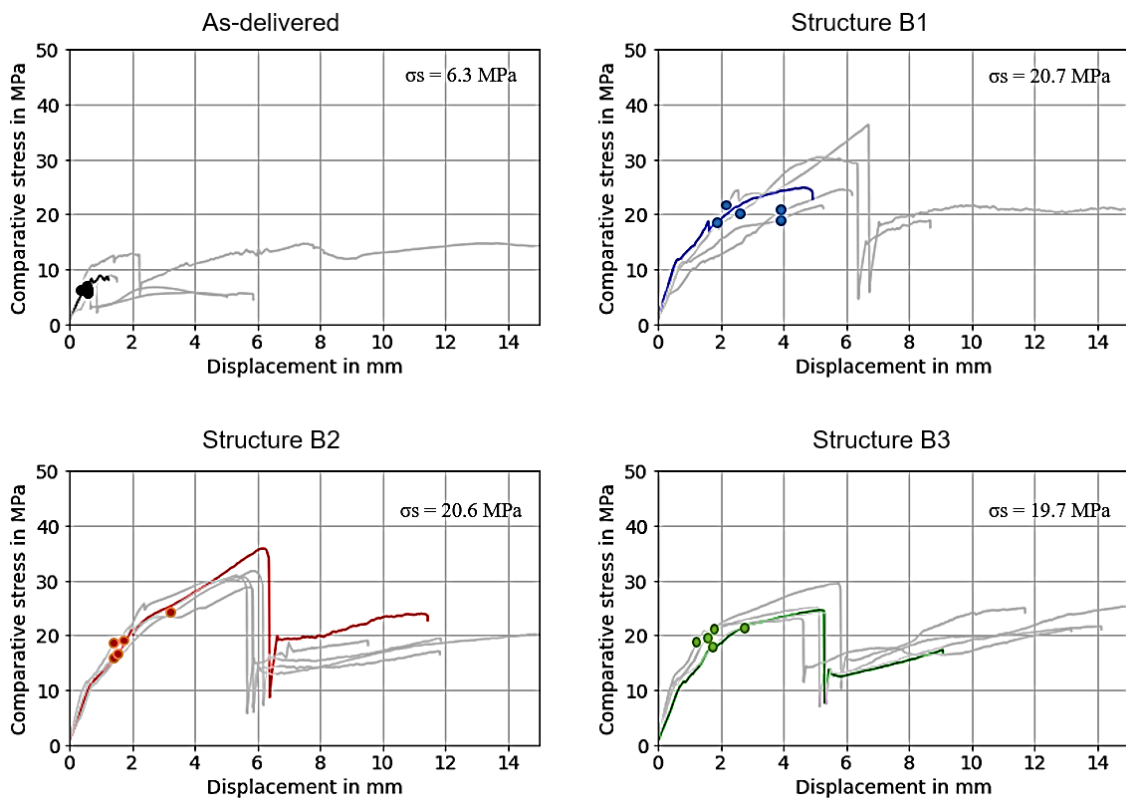


Figure 29: The stress-displacement curves from the mechanical laboratory pull-out tests of all tested samples for the SMA wire with a structured surface and the as-delivered SMA wire with a nominal diameter of 1 mm. The first interfacial failure shear stresses calculated according to [50] are marked.

To precisely quantify this finding and to obtain a first approximation of the surface-dependent stress required to trigger either a first or a complete interfacial failure, the integral of the stress-displacement curve up to the corresponding stress level (first or complete interfacial failure) was calculated using the method described in section 6.2.4. The resulting values are compared and visualized in Table 8.

Table 8: The calculated integral for the stress-displacement curves generated using the mechanical laboratory pull-out test for the SMA wire with a nominal diameter of 1 mm with different surface morphologies are demonstrated. The mean values of the surface-dependent stress with the 99 % confidence intervals are shown. Two points are considered in the curve progression, the moment of first interfacial failure and the complete interfacial failure.

Interface	As-delivered	Structure B1	Structure B2	Structure B3
First Failure	2.01 N/mm ± 0.64 N/mm	29.93 N/mm ± 9.13 N/mm	26.81 N/mm ± 2.2 N/mm	21.36 N/mm ± 1.67 N/mm
Complete Failure	5.2 N/mm ± 2.31 N/mm	121.95 N/mm ± 35.7 N/mm	116.9 N/mm ± 3.48 N/mm	86.77 N/mm ± 4.37 N/mm

Considering the 99 % confidence intervals, no difference between Structure B1 and B2 can be observed for the first and the complete interfacial failure. Structure B3 shows minor values for both. An increase of 14.9 times of the mean surface-dependent stress of Structure B1 to the as-delivered state can be measured. The mean surface-dependent stress for the complete interfacial failure is 23.5 times higher for Structure B1 than for the as-delivered SMA wire.

The SEM method described in section 6.1.4 was used to examine the surfaces of the SMA wires after the pull-out test to analyze the interfacial failure modes by visualizing the amount of polymer matrix residues on the SMA wire surface. Figure 30 compares SEM images for the different SMA wire surface variants. The polymer matrix residues are highlighted. The surface pit distribution is also shown in the Figure for reference. For the analyzed images, the most polymer matrix residues in the SMA wire surface pits can be found for Structure B1. Almost no polymer residuals can be found on the as-delivered SMA wire surface.

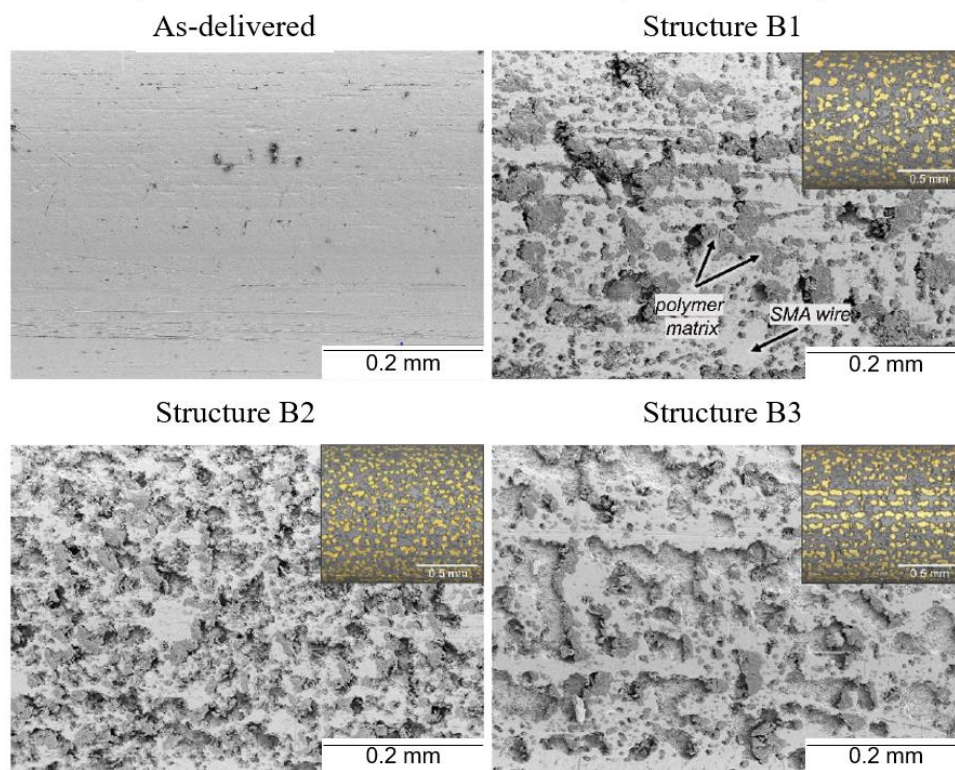


Figure 30: Representative SEM images of the pulled-out SMA wire with a nominal diameter of 1 mm showing the amount of matrix residues on the SMA wire surface for the four different surface variants.

7.2.2 SMA wire with a Nominal Diameter of 0.5 mm

The correlation between the force of first interfacial failure and the increase in the surface area due to the applied SMA wire surface structuring is visualized in Figure 31 for the mechanical laboratory pull-out test. Mean values with 99 % confidence intervals are given for each surface condition based on five samples, as described in section 6.2.1. The structuring of the SMA wire surface contributes to both an increase in surface area and the force required for the first interfacial failure. A mean value of 28.5 ± 1.9 N was measured for the as-delivered SMA wire. The differences in the surface structure between Structures S1 and S2 were described in section 7.1.2, causing a recognizable deviation in the force required for the first interface failure.

For Structure S2, an increase in the force of first failure of factor 1.13 compared to the as-delivered SMA wire condition could be measured. The mean value for the force of first failure was 32.2 ± 1.6 N. The enlargement of the surface area of Structure S2 was quantified by a factor of 1.16 compared to the SMA wire as-delivered. With an increase

in surface area of 1.24, the surface enlargement for Structure S1 was slightly higher, resulting in a measured force of first failure of 42.6 ± 2.8 N. The increase of force of first failure compared to the as-delivered SMA wire was factor 1.5.

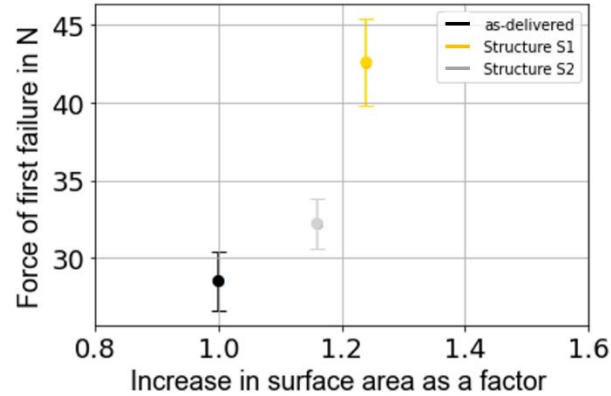


Figure 31: The results of the mechanical laboratory pull-out test for the SMA wire with a nominal diameter of 0.5 mm are demonstrated. The mean values of the force of first failure for all tested structured SMA wire surface variants and the as-delivered SMA wire over the increase in surface as a factor is shown. The error bars represent the 99 % confidence interval, the results are demonstrated without outliers.

The comparative stress–displacement curves for all tested configurations are demonstrated in Figure 32. The interfacial shear stress of the first interfacial failure, according to [50], is marked. A scattering of the values for the first interfacial failure for each surface condition can be seen, as described previously. A difference in the curve progression is visible between the as-delivered pull-out curves and the curves of the SMA wire with a structured surface. The stress load capacity of the pull-out curves for structures S1 and S2 is significantly higher after the onset of the first interfacial failure. In addition, complete interfacial failure occurs with the structured variants at larger displacement and stress values than with the as-delivered SMA wire. Almost no difference between the two structured SMA wire configurations was measured regarding the maximum comparative stress. Structure S1 reaches higher displacement values for the complete interfacial failure.

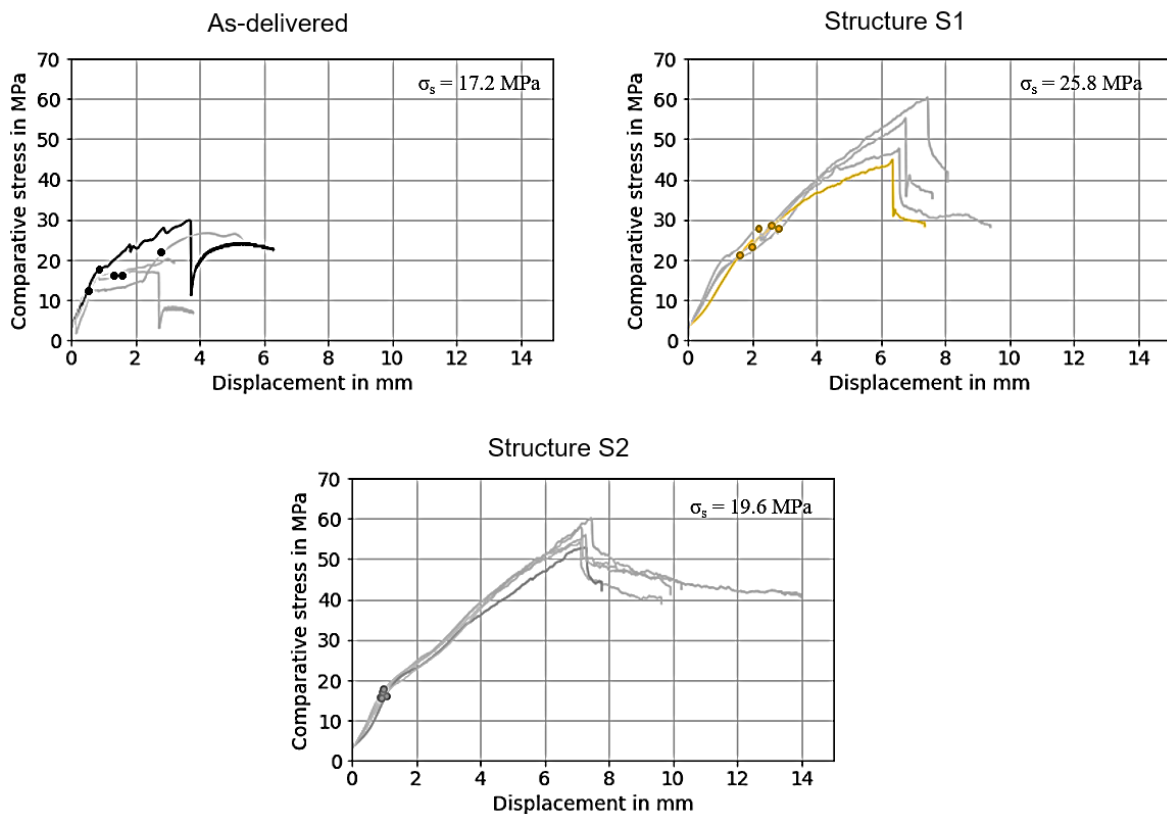


Figure 32: The comparative stress-displacement curves from the mechanical laboratory pull-out tests of all tested samples for the SMA wire with a structured surface and the as-delivered SMA wire with a nominal diameter of 0.5 mm. The first interfacial failure shear stresses calculated according to [50] are marked. The mean interfacial shear strength is also given for each SMA wire surface structure variant.

The calculated surface-dependent stress results are demonstrated in Table 9. The mean values with the 99 % confidence interval for the three analyzed SMA wire surface configurations for both first interfacial failure and complete interfacial failure are given. Structure S1 shows the highest value for the surface-dependent stress for the first interfacial failure. Concerning the standard deviation between Structures S1 and S2, there is no recognizable difference in the surface-dependent stress for complete interfacial failure. The calculated mean value for the surface-dependent stress of Structure S1 is 3.4 times higher than for the as-delivered SMA wire. For the complete interfacial failure, Structure S1 shows 1.3 times higher values.

Table 9: The calculated integral for the stress-displacement curves generated using the mechanical laboratory pull-out test for the SMA wire with a nominal diameter of 0.5 mm with different surface morphologies are shown. Two points are considered in the curve progression, the moment of first interfacial failure and the complete interfacial failure. The mean values of the surface-dependent stress with the 99 % confidence intervals are shown.

Interface	As-delivered	Structure S1	Structure S2
First Failure	10.7 N/mm ± 2.01 N/mm	36.5 N/mm ± 9.5 N/mm	15.79 N/mm ± 3.41 N/mm
Complete Failure	74.86 N/mm ± 18.6 N/mm	218.26 N/mm ± 26.77 N/mm	240.98 N/mm ± 3.41 N/mm

The pulled-out SMA wires were analyzed to understand the interfacial failure modes better (Figure 33). On the SMA wire surfaces of Structures S1 and S2, matrix residues can be seen in the surface pits. No real differences between the two structured SMA wire variants can be observed. Almost no polymer matrix residues can be found on the as-delivered SMA wire.

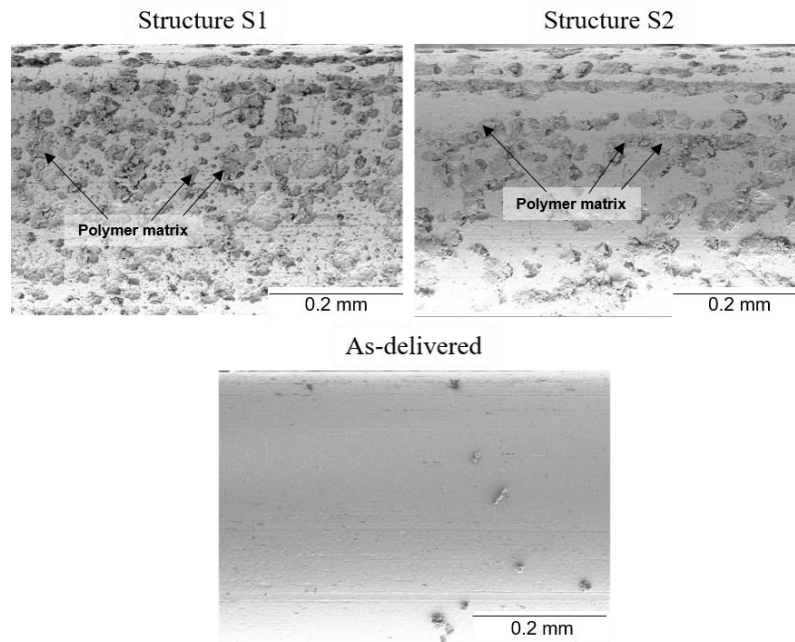


Figure 33: Representative SEM images of the pulled-out SMA wire with a nominal diameter of 0.5 mm showing the amount of matrix residues on the SMA wire surface for the three different surface variants.

7.2.3 Discussion of the Influence of the SMA Wire Surface Morphology on the Force Transfer between SMA Wire and Polymer Matrix

The first interfacial failure starts in all conducted mechanical laboratory pull-out tests at the SMA wire entry point (Figure 14), which agrees with the state of the art discussed in section 3.5. The results show an increase in the force of the first failure due to the applied surface structuring for all tests with the SMA wire with 0.5 and 1 mm, as illustrated in Figure 25 and Figure 30. The increase in the force of the first interfacial failure can be partly attributed to the surface enlargement applied by the selective electrochemical etching process. Considering the SEM images illustrated in Figure 30 and Figure 33 and the presented polymer matrix residues in the surface pits, a partially cohesive interfacial failure behavior can be postulated. These polymer matrix residues indicate that the liquid polymer matrix has penetrated the SMA wire surface pits, resulting in mechanical interlocking after curing. Since no coupling agents were used, the formation of chemical bonds that contribute to interfacial strength is considered unlikely.

Referring to the comparative stress-displacement curves shown in Figure 29 and Figure 32, it can also be demonstrated that structuring the surfaces of the SMA wires increases the stress required for both the first and complete interfacial failure. After the first failure, the mechanical interlocking between SMA wires with structured surfaces and the polymer matrix implies an increased stress-bearing capacity. In contrast, almost no force transfer is measurable for the as-delivered SMA wire after the first interfacial failure appeared. Since the same assumptions are made for the calculation and the overall increase in surface area due to the structuring is taken into account in the calculation, it seems permissible to state that the structuring requires more energy to provoke an initial failure and an overall interface failure.

Between the forces of first failure for the different structured SMA wire surfaces with a nominal diameter of 1 mm, no significant difference can be measured, considering the 99 % confidence interval. However, the mean values show a tendency for the type of structuring having an influence on the resulting force transfer. The applied SMA wire surface structures were comparable but small differences can be quantified, as discussed in section 7.1.1. The structured surface SMA wires (1 mm) improve the force transfer via the interface compared to the as-delivered SMA wire at maximum by fac-

tor 3.3. The maximum increase of the surface area as a factor was 1.5 for Structures B1 and B2 (1 mm). However, the SEM surface images for these two surface structured SMA wire variants demonstrate a difference in the amount of visible polymer matrix residues. The difference in the amount of polymer matrix residues on the SMA wire surface could depend on the pit volume and the pit shape. Structure B1 (1 mm) shows mostly omega-shaped pits, as described in section 5.2, which could explain why most polymer matrix residues can be found on the pulled-out SMA wire surface of Structure B1.

The results indicate a measurable difference in the force of the first interfacial failure in the mechanical laboratory pull-out test between Structures S1 and S2 (0.5 mm). Although both surface structure variants increase the force of the first interfacial failure compared to the as-delivered SMA wire, Structure S1 (0.5 mm) with a factor of 1.49 achieves a more distinct improvement than Structure S2 (0.5 mm) with a factor of 1.13. The difference in the force of first failure of Structures S1 and S2 (0.5 mm) indicates that the specifications of the surface morphology influence the interfacial failure behavior. The SEM images show no visible difference in the amount of matrix residues in the surface pits on the structured SMA wire surface, and all surface pits are filled.

The differences in the applied surface morphology of the structured surface SMA wire with a nominal diameter of 1 mm are less prominent compared to the differences between Structures S1 and S2 (0.5 mm). Comparing the results of the force of first interfacial failure for both diameters of the structured variants of the SMA wires, reveals that the thinner SMA wires (0.5 mm) achieve a lower increase due to the surface structuring process. By reducing the SMA wire diameter, a lower force of first interfacial failure can be demonstrated for the as-delivered SMA wire surface condition. In order to relate the results shown for the two SMA wire diameters with each other, a new describing variable, the surface-dependent stress (section 6.2.4), has to be implemented.

The surface-dependent stress values shown in Table 8 and Table 9 help to compare and interpret the results shown so far and are visualized as an overview in Figure 34.

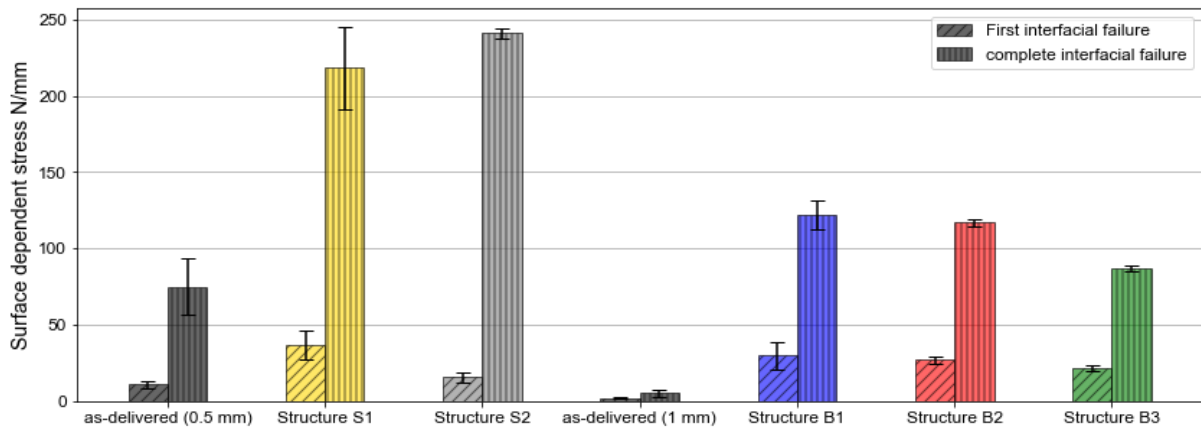


Figure 34: Overview of the mean values of the surface dependent stresses determined from the mechanical laboratory pull-out test for all tested SMA wire surface variants, the mean values with the 99 % confidence intervals are shown.

These values show the transferable force normalized to the respective SMA wire diameters calculated from the μ CT data in relation to the measured deformation of the SMA wire during the pull-out test. It is not possible to specify the applied strain during the pull-out test, as it can be assumed that the non-embedded SMA wire detwines first followed by an increase of the applied interfacial force. The SMA wire surface structuring seems to influence the surface-dependent transmissible stress between the SMA wire and the polymer matrix. For the SMA wire with a nominal diameter of 1 mm, Structure B3 shows a slightly lower optimization of stress transfer considering the 99 % confidence interval. Comparing the results of the surface-dependent stress between the SMA wires (0.5 and 1 mm) in the as-delivered SMA wire surface condition and the polymer matrix, there are clearly higher surface-dependent stresses for the thinner SMA wire (0.5 mm) for both the first as well as the complete interfacial. For the interfacial first failure and the complete interfacial failure, Structures S1 (0.5 mm) and B1 (1 mm) show comparable values, considering the 99 % confidence intervals, for the surface-dependent interface stresses. For the SMA wire with a nominal diameter of 0.5 mm, the increase in the transferable surface-dependent interfacial stress due to the surface structuring of the SMA wire is significantly lower than for the SMA wires with a nominal diameter of 1 mm.

7.3 Characterization of the Interfacial Failure Behavior of an SMAHC during Pull-Out Test and the Influence of the Thermomechanical Clamping due to Embedding the SMA Wire

The μ CT *in situ* pull-out test was done to 3D characterize the interfacial failure propagation between SMA wire and polymer matrix with a great resolution and to simultaneously measure the failure radial and axial strain during the pull-out test using DVC analysis. The μ CT *in situ* pull-out test was described in sections 6.3.1. The reconstruction was done as described in section 6.1.6, and the DVC analysis on the structured SMA wire surface was done as described in section 6.3.3. The analysis of the progression of the delamination in the interface between SMA wire and polymer matrix was done using the segmentation technique described in section 6.3.4. The results are demonstrated below. This test was performed on the μ CT *in situ* pull-out samples with a nominal diameter of the embedded SMA wire of 0.5 mm.

7.3.1 SMA Wire with a Nominal Diameter of 0.5 mm

The starting point of the analysis of the collected μ CT data was to determine the force of first interfacial failure. This was achieved by a detailed examination of the cross-sectional images from the tomographic reconstruction for each loading step. These image stacks were created for each μ CT *in situ* pull-out sample tested. The analysis process is visualized for a representative sample in Figure 35. The images show the same sample (Structure S1) at different load levels at almost the same position in the z-direction. In the top view reconstructions, the cross-section of the embedded SMA wire is visible and with higher load steps, the gradual occurrence of interfacial failure in terms of delamination between the SMA wire with structured surface and the polymer matrix can be demonstrated. The area of delamination occurrence is marked red in the reconstructed images and can be seen as a black phase between the SMA wire surface and polymer matrix. In the exemplary analysis, not all force steps tested are integrated to keep the results concise. One exemplary Figure for the interfacial failure propagation for Structure S2 can be seen in the appendix A.10.

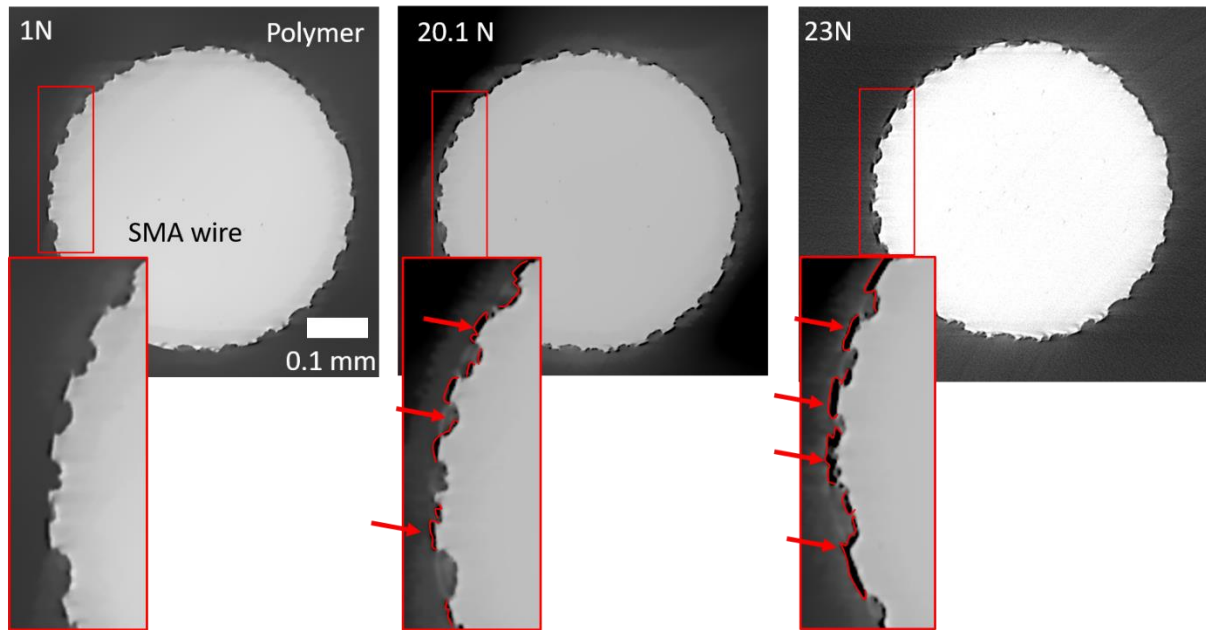


Figure 35: Three load steps of a representative Structure S1 (0.5 mm diameter, sample 2) *in situ* pull-out sample, showing the top view slice through tomographic reconstructions of the embedded SMA wire. Approx. the same z-position close to the SMA wire entry point is shown. The advancing delamination is visualized with increasing force steps. The red marked area demonstrates where the delamination starts in the circumferential direction and is therefore shown enlarged. [160]

The visualization of the interfacial failure process shows that the interfacial failure process during the μ CT *in situ* pull-out test can be observed. The top view reconstruction images show the three phases, SMA wire cross-section, polymer matrix and interfacial delamination area, which can be distinguished and quantified. The introduced surface pits to the SMA wire are visible, and the variability of the introduced SMA wire surface pit shapes can be seen. The shape of the surface pits is replicated in the polymer matrix in the contact area between the SMA wire and the polymer matrix. Some surface pits are omega-shaped or show smaller pits in the bowls of the larger surface pits. Additionally, to the three phases already mentioned, a slight black shadow around the circumferential of the SMA wire cross-section can be observed, which is caused by the so-called enhanced edge phase contrast [65]. This scan artifact is also described in section 2.3. A narrow black stripe between the SMA wire and the polymer matrix, even with no applied load, can be observed on all cross-sectional images from the tomographic reconstruction for each loading step. Due to the difference, the first interfacial failure can only be determined when the delamination grows larger than the contrast stripe around the SMA wires. However, due to the high resolution, the moment of first

interfacial failure can still be determined more accurately than in the mechanical laboratory pull-out test. The first delamination is visible at a force of 20.1 N, and with a higher load, the delamination grows further in height and width. The failure of the interface often starts as a small crack, which expands into a delamination as the load increases. The growth of the delamination is unevenly distributed in the circumferential direction over the entire cross-section of the sample, as can be seen in the top view.

To gain a first insight into delamination growth during μ CT *in situ* pull-out testing, visualization of a representative reconstruction image of the side view of a previously failed pull-out test sample can provide valuable information. The interfacial progression of the delamination in two planes is demonstrated in Figure 36, showing the top and side view of the same representative sample as chosen above for an applied force of 27 N. This gives an example of the delamination growth in the radial direction (r-axis) (a). Additionally, a projection image showing the growth alongside the SMA wire length axis (z-axis) is shown in Figure (b).

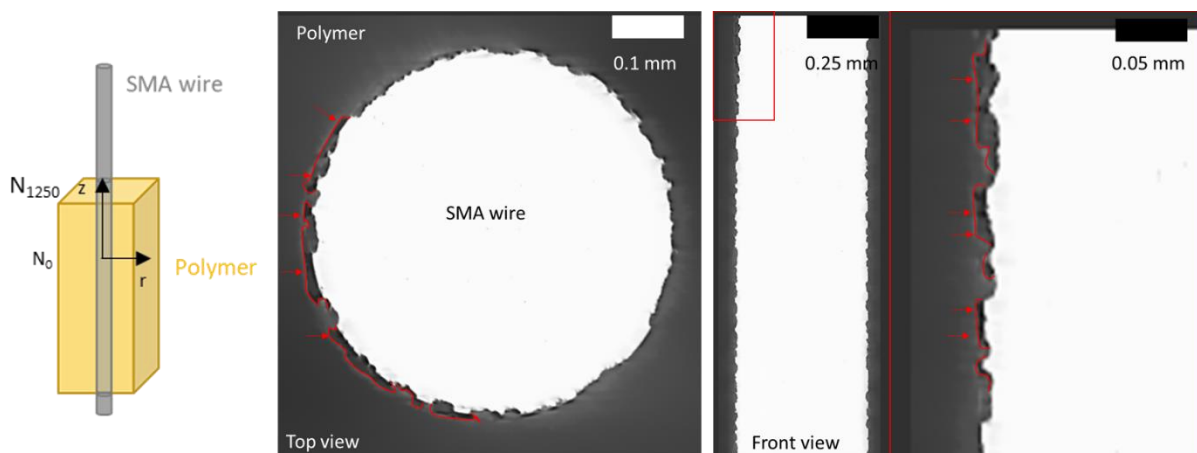


Figure 36: Representative images of the development of the delamination for an applied force of 27 N for a Structure S1 pull-out sample (sample 2). The top view slice through tomographic reconstruction (a) at a z-position close to the SMA wire entry point is shown. Additionally, the side view slice through reconstruction (b) with an enlarged view of the red marked delaminated area (c). The delamination visible in a) and c) is marked with yellow arrows.

To quantify and describe the delamination growth visualized in Figure 35 and Figure 36 across the entire image stack acquired during a single loading step in μ CT analysis, a segmentation technique, described in section 6.3.4, was used. With this analysis method, the three phases, SMA wire cross-sectional area, polymer matrix and delamination area, can be segmented. For further analysis, the amount of delamination along the perimeter of the SMA wire cross-section and the change in the cross-sectional area

of the SMA wire were segmented. This phase segmentation was done for all reconstruction images (N) along the z-direction for every load step for the μ CT *in situ* pull-out samples tested. Therefore, the progression can be quantified and visualized, demonstrated in Figure 37 for a representative sample of Structure S1. Only the curve propagations of a few relevant loads are integrated. Figure 37 (a) illustrates the amount of delamination along the z-axis for every chosen load, 1250 images were analyzed along the z-axis, where N=1250 represents the entry point image of the SMA wire into the polymer matrix (Figure 37 (c)). The scan artifact previously described cannot be distinguished from the delamination phase segmentation and slightly influences the quantification of the amount of delamination. Analyzing the first interfacial failure and the load steps before a noise level can be determined. The influence of the scan artifact on quantifying the amount of delamination is approx. in the range of 2-3 pixels. The first interfacial failure visualized previously in Figure 35 was at a force of 20.1 N. This cannot be verified only by looking at the progression of the amount of delamination visualized in Figure 37 (a). However, at this force, there is an evident change in the SMA wire cross-sectional area (Figure 37 b). By further increasing the load, an increase in the amount of delamination in the z-direction can be visualized. The largest delamination in r-direction continues to appear at the SMA wire entry point.

In Figure 37 (b), the development of the cross-sectional area of the SMA wire was analyzed for different load steps in the z-direction. With the growing amount of delamination, the SMA wire contracts more, and the SMA wire cross-sectional area decreases. Therefore, the SMA wire cross-sectional curve's propagation is inverse to the amount of delamination. At the lower load levels, the SMA wire cross-sectional area is almost constant for the analyzed ROI and the contraction of the SMA wire is visible at an applied force of 20.1 N. The contraction of the SMA wire starts at the SMA wire entry point and is not homogenous in the z-direction, but the distribution is visible for the entire ROI. The amount of SMA wire contraction decreases in the z-direction.

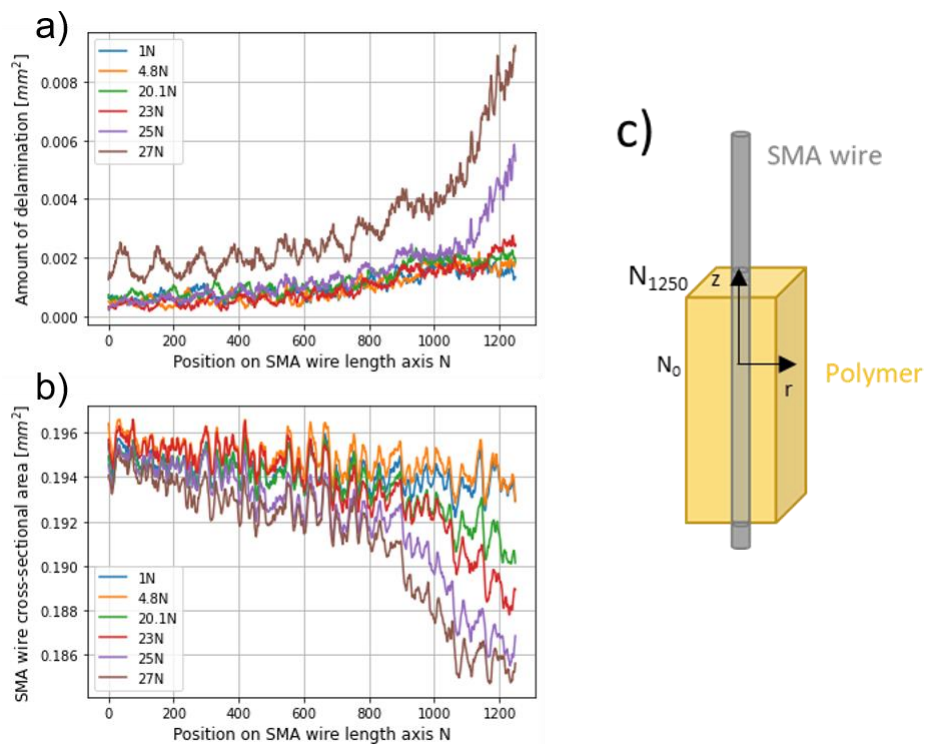


Figure 37: Development of the amount of delamination a) and the SMA wire cross-sectional area b) for each slice through tomographic reconstruction in z-direction for the load levels, 1 N, 4.8 N, 20.1 N, 23 N, 25 N and 27 N. The segmentation analysis was done for a Structure S1 pull-out sample (sample 2). The position on the SMA wire length axis $N = 1250$ is denoted as the SMA wire entry point image. In c) a schematic pull-out sample is shown illustrating the coordinate system and the description of the position on SMA wire length axis N . [160]

DVC analysis, described in section 6.3.3, was used to evaluate the strain applied to the SMA wire structured surface's embedded section, starting from the SMA wire's entry point into the polymer matrix during the μ CT *in situ* pull-out test. The analysis is divided into a global analysis, which gives a mean value for the axial and radial strain for the ROI and the local strain, which shows the radial and axial strain distribution on the SMA wire surface for the ROI. The axial and radial strain (global and local) definitions are specified in section 6.3.3, Figure 17.

The results of the global DVC analysis for three tested samples of Structure S1 are demonstrated in Figure 38, showing the global axial (a) and radial (b) strain over the applied load. The crosses mark the identified moment of first failure for each sample in the Figure (19.1 N, 20.1 N, 19.4 N). The global axial strain increases with a higher load level. The progression of two of the three tested pull-out samples is almost similar

for Structure S1. In contrast, the third sample's curve propagation was distinguished, and a two times larger global axial strain at first failure was measured.

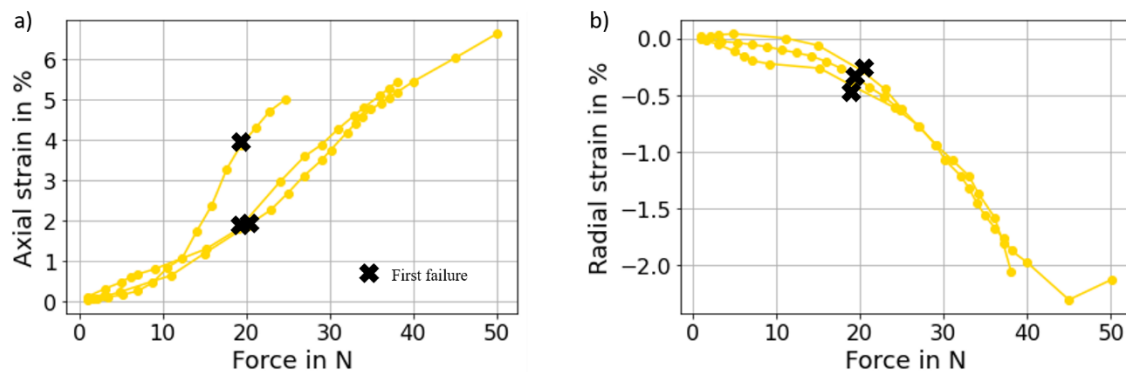


Figure 38: Visualization of the global axial a) and radial b) strain vs. applied pull-out force, derived from DVC analysis for all embedded SMA wires with the same structured surface (Structure S1). A black cross marks the moment of first failure for all tested samples. [160]

For the three μ CT *in situ* pull-out Structure S1 samples, the global axial strains are 1.8 %, 1.9 % and 3.8 %, and the global radial strains are -0.45 %, -0.28 % and -0.34 % for the first interfacial failure. The progression of the radial strain follows the negative Poisson's ratio of the SMA wire with a decreasing cross-section of the SMA wire for all three samples.

For comparison, the DVC analyses of the global axial and radial strain of the three samples tested in the μ CT *in situ* pull-out test with Structure S2 are illustrated in Figure 39. The maximum axial strain applied during the μ CT *in situ* pull-out test was more than 6 %. The progression of the axial curves is slightly different, and the first failure values differ between the three tested samples. The first interfacial failure was observed at a load level of 13.8 N, 21.1 N and 9.1 N. The related axial and radial strain values are 1.9 %, 4.7 %, 0.99 %, and -0.23 %, -0.34 %, -0.08 %.

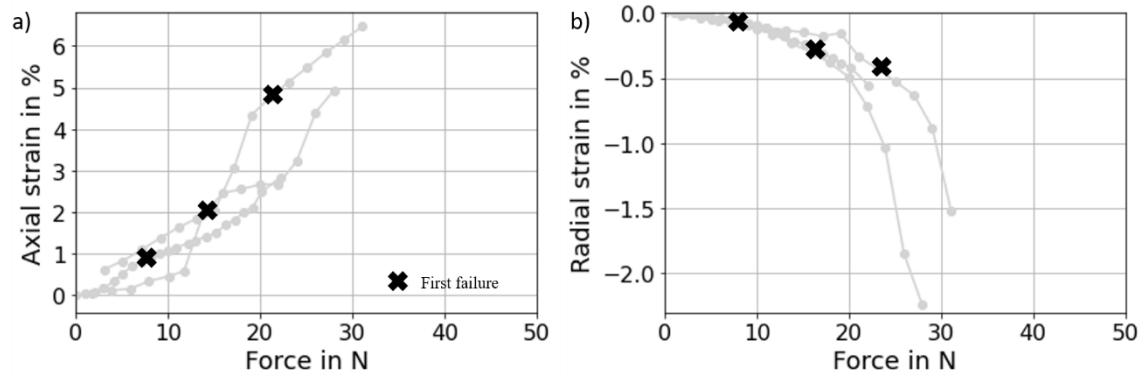


Figure 39: Visualization of the global axial a) and radial b) strain vs. applied pull-out force, derived from DVC analysis for all embedded SMA wires with the same structured surface (Structure S2). A black cross marks the moment of first failure for all tested samples.

Figure 40 compares the local axial and radial strain distribution plotted on the circumferentially unrolled SMA wire surface of the observed ROI for different loads. The whole SMA wire surface can be visualized over the observed ROI by unrolling the cylindrical SMA wire shape. For the Structures S1 and S2, a representative sample is shown. The strain distribution is visualized using color bars and given in different scales in radial and axial directions. For the chosen samples, the first failure was at a force of 19.1 N (Structure S1) and 9.1 N (Structure S2).

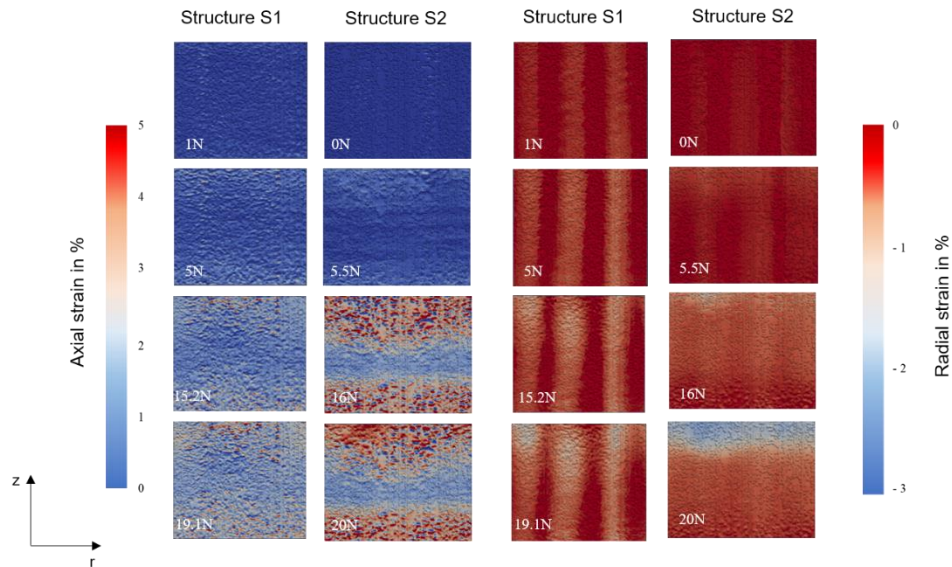


Figure 40: Local axial and radial strain distribution, derived from DVC analysis. Data are shown as circumferentially unrolled structured SMA wire surface. For each Structure (S1 (sample 1), and S2 (sample 3) a representative analysis is shown.

In the axial direction, both structured SMA wires show the development of the applied strains increasing from two sides. For almost the same force at 15.3 N (Structure S1) and 16 N (Structure S2), higher strain values and distribution for the axial strain can be seen for Structure S2. The radial contraction of the embedded Structure S2 during the μ CT *in situ* pull-out test seems more homogenous, higher strain values are achieved for the same loads, and the appearance of preferential planes seems less prominent.

To gain an understanding of the extrinsic thermomechanical clamping of the SMA wire with structured surface (Structure S1) by embedding it in the polymer matrix, a comparison of the global strain values of the embedded SMA wire tested in the μ CT *in situ* pull-out test and the non-embedded SMA wire, which was strained *in situ* is visualized in Figure 41. The comparison in the global axial direction shows hardly any difference between the two curve progressions. In the global radial direction, a distinct difference is visible. Due to the limited number of samples and the limited measurement time, the number of measurement points recorded varies.

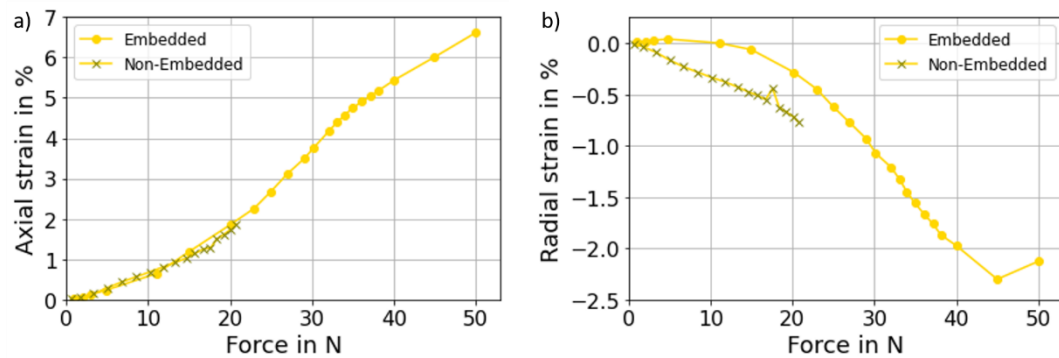


Figure 41: Comparison of the global axial a) and radial strain b) over the applied load for the non-embedded and the embedded SMA wire with structured surface (Structure S1).

As mentioned above, the DVC analysis can also be visualized locally to illustrate the strain distribution directly on the circumferentially unrolled, structured SMA wire surface. Figure 42 compares the local axial and radial strain distribution on the unrolled structured SMA wire surface for both embedded and non-embedded structured SMA wires (Structure S1) for a representative sample and four loads.

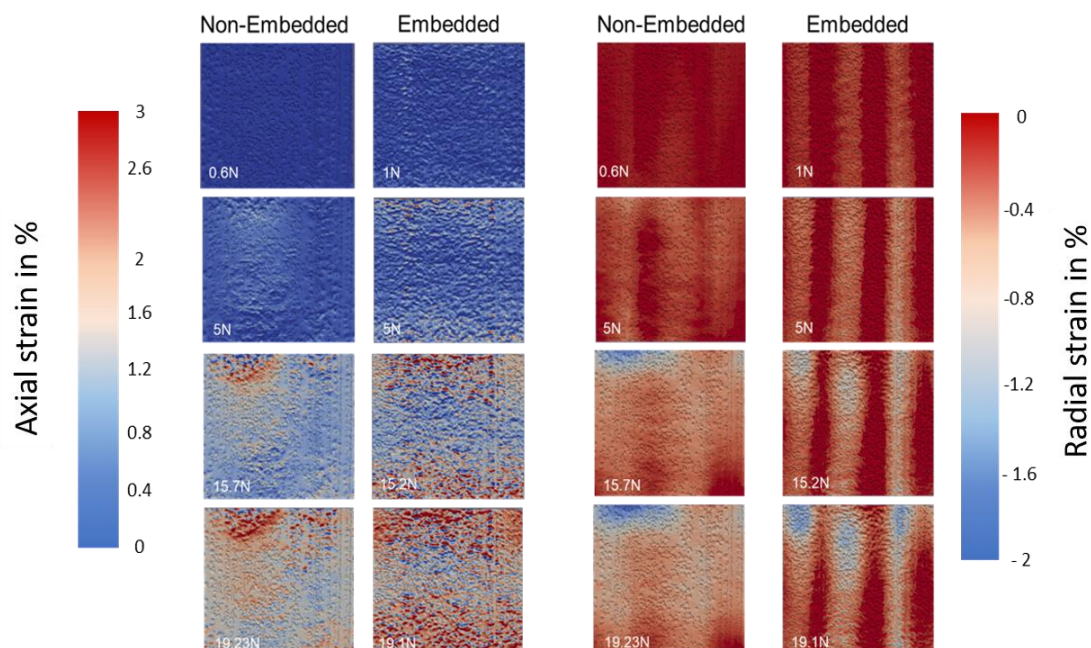


Figure 42: Local axial and radial strain distribution, derived from DVC analysis. Data are shown as circumferentially unrolled structured SMA wire surface (Structure S1). A comparison of an embedded and non-embedded SMA wire for four load levels is shown. [160]

The identified first interfacial failure occurs at a force of 19.1 N for the embedded sample. Identical to the first interfacial failure occurring, the highest strain value in the z-direction is observable at the SMA wire's top end, representing the SMA wire entry point

into the polymer matrix. A progressive expansion of the axial strain in the z-direction can be observed for the non-embedded SMA wire with a structured surface. In contrast, the axial strain seen for an embedded SMA wire is characterized by a more homogeneous distribution over the observed ROI. Additionally, a non-uniform distribution of the local axial strain along the perimeter of the cross-section of the non-embedded SMA wire is visible. The local axial strain distribution for the embedded SMA wire is more uniform.

The local radial strain shows three preferential planes for the embedded SMA wire, which indicates a non-uniform contraction during the μCt *in situ* pull-out test. The SMA wire surface parts outside of those preferential contraction planes do not contract. The effect is more prominent for the embedded SMA wire but can also be observed for the non-embedded SMA wire.

7.3.2 Discussion of the Findings by Micromechanical Analysis of the Force Transfer between SMA Wire with Surface Modifications and Polymer Matrix and the Influence of the Thermomechanical Clamping of the SMA Wire due to Embedding

By using stepwise μCT *in situ* pull-out testing, new volume insights into the interaction and the interfacial failure-driven mechanism between SMA wire and polymer matrix can be achieved. The change on the SMA wire surface and the interfacial failure progression can be recorded, visualized and quantified. Observing the interfacial failure debonding process with a high resolution and using analysis methods can help to understand the relationship between applied load resulting in radial and axial surface strains and interfacial failure propagation.

The μCT images show that the SMA wire surface pits are filled with polymer matrix, indicating that the polymer matrix penetrates the inserted surface structuring, thereby generating mechanical interlocking. The interfacial failure is observable as progressive delamination between the SMA wire and the polymer matrix, and it starts at the SMA wire entry point and propagates from there, which is in good agreement with the state of the art discussed in section 3.5. The interfacial delamination grows stronger on one side in the SMA wire circumferential direction. In the circumferential direction, one side of the SMA wire still seems firmly bonded to the surrounding polymer matrix at first interfacial failure. The first interfacial failure in the form of a crack or first delamination

starts at one point and propagates from there. This could be attributed to the brittle interface failure between SMA wire and polymer matrix, which was also proposed by theoretical investigations [105, 168]. The delamination area can be quantified by using a segmentation method. Due to the delamination, an even larger difference in the absorption coefficient at the SMA interface (SMA wire/air vs. SMA wire/polymer matrix) is caused, resulting in sufficient contrast to detect the delamination onset. The spread of the delamination in the width seems to grow faster than in the depth. This is probably also related to the radial contraction of the SMA wire by increasing the load. However, what happens first is uncertain from the data. Does the delamination grow due to the strong contraction of the SMA wire, or can the SMA wire contract more in the radial direction due to the delamination?

The influence of the radial contraction of the SMA wire (Poisson's ratio) on the interfacial failure propagation has already been postulated by [11, 89, 129], as discussed in section 3.5. As far as the author is aware, the propagation of delamination in the cross-sectional volume has not yet been investigated. Therefore, what happens first cannot be answered unambiguously according to the state of the art (section 3) and the measurements carried out so far.

The applied SMA wire surface structuring can be used to trace the applied radial and axial strain in the ROI utilizing DVC. The DVC analysis on the structured SMA wire surface allows the axial and radial strain of the embedded SMA wire to be traced over the volume for the first time. The results show that the first interfacial failure for Structure S1 is within a similar load range for the three samples tested. The forces of the first interfacial failure for the three specimens show an average value of 19.5 N with a 99 % confidence interval of ± 0.42 N. If the shear stress is calculated from this mean value according to [50] as described in section 6.2.3, a first failure interfacial stress of 14.3 MPa is obtained.

The progression of the strain-force curves shown in Figure 38 is similar for two samples, but a third shows a very different progression. The deviation of the third curve could be explained by the high standard scatter in micromechanical tests. The sample fails compared to the two samples (which have a similar curve propagation) at a much higher axial strain of 3.8 %. However, at a lower radial strain of the SMA wire of -0.34 % and the curve propagation shows a steeper trend, indicating that less applied load is needed to induce a higher axial strain. The global axial strain at first interfacial failure is significantly higher than the elongation at break of the polymer matrix specified by

the manufacturer, which is 1.5 - 2.5 % [147]. Locally, much higher axial strains can be observed which occur in spots as shown in the Figures 40 and 42. Due to the limited amount of samples, outlier analysis is not meaningful. A physical cause for the large deviation in the first interfacial failure between the SMA wire and the polymer matrix observed could be the different influences contributing to the interfacial failure, which are equally important and exert different constraints. As a consequence, several factors could trigger the first interfacial failure, which was also postulated in [11, 89, 129] and was already discussed in section 3.5. Accordingly, the interface can fail if the maximum transmissible strain in the radial or the axial direction or the interfacial tension applied by the load is exceeded. The global axial strain values of the other two samples are in the range of the elongation at break of the polymer matrix, which would support the second assumption.

The characteristic stress-strain behavior of the non-embedded SMA wire should be macroscopically homogeneous but may vary microscopically, as explained in section 2.1. The micromechanical stress-strain characteristics of the SMA wire could also result in variations in the behavior of the embedded SMA wire. The progression of the determined curves and the determined values of the first interfacial failure could also be influenced by the applied SMA wire surface structuring, which is homogeneous from a macroscopic point of view but shows local variations from a microscopic point of view.

A similar phenomenon can be observed for Structure S2. The trend of the individual curves of the three measured samples shown in Figure 39 shows even more significant deviations in the axial strain direction (z-axis). Except for one specimen, the specimens with Structure S2 fail at lower force values and a lower radial strain compared to Structure S1. The calculated interfacial mean shear strength is 10.8 MPa for the three samples tested. However, for one sample, the axial strain is in the range of the elongation at break of the enveloping polymer matrix. Another sample fails at a smaller strain, and the third sample at a higher strain. The determined first interfacial failure strain and force values fluctuate significantly more than for Structure S1. This could be due to the applied SMA wire surface structuring, which shows larger surface pits with greater distance between the pits compared to Structure S1. As a result, the micromechanical inhomogeneity is greater. In addition, in the case of Structure S2, the progression of the radial strain over the force is more reproducible than the trend of the axial strain. For both Structures S1 and S2, there is an increase in the radial strain values over the

force after the first interfacial failure has occurred. This indicates that the SMA wire can contract radially more easily after being delaminated from the surrounding polymer matrix. The assumption that the propagation of the interface's delaminated area correlates with the SMA wire's radial contraction is thus supported.

Considering the local strain distribution shown in Figure 40, clear evidence that the applied SMA wire surface structure influences the interfacial failure propagation is provided. Structure S1 shows preferential planes in the radial strain direction, indicating that the SMA wire does not contract homogeneously. An explanation can be found in the polymer matrix, which still holds the SMA wire at some points and keeps the SMA wire from contraction. Structure S2 does not show those preferential planes, which could be an explanation for the lower interfacial strength previously described. Due to the larger surface pits distributed with a lower density and less force transferring, mechanical interlocking points are distributed over the ROI of the SMA wire. The radial strain is applied almost homogeneously but Structure S2 shows preferential strain planes in the axial direction (z-axis). This could be due to the unique stress-strain characteristics of the non-embedded SMA wire explained in section 2.1, describing a microscopic non-homogeneous distribution of the applied axial strain, depending on the detwinning characteristics of the SMA wire. The locally more prominent hindrance of the radial contraction of the SMA wire by the polymer matrix could also explain the non-uniform delamination propagation, which has been previously described. For Structure S2, higher and more strains can be seen for almost the same applied load compared to Structure S1, which can be attributed to the already failed interface by a lower load. The two investigated surface structures of the SMA wire show that the embedding of the SMA wire prevents radial contraction until the first interfacial failure occurs. The omega-shaped SMA wire surface pits, which serve as an interlocking structure and form a strong mechanical bond between the SMA wire and the polymer matrix, can be attributed to the improvement in force transmission.

Comparing the embedded SMA wire and the non-embedded SMA wire strain-force behavior shows the influence of the surrounding polymer matrix on the stress-strain characteristics of an SMA wire. Nearly no variation of the global axial strain development during the μ CT *in situ* pull-out test with increasing load can be measured. However, embedding the SMA wire into the polymer matrix considerably influences the radial strain of the SMA wire under load. Observing the local strain distribution on the

unrolled SMA wire in axial and radial directions, differences can be visualized for almost the same applied load between the embedded and non-embedded sample shown in Figure 42. Although the non-embedded SMA wire displays the same strain distribution as shown in [18], the embedded SMA wire strains more homogeneously along the SMA wire length and the cross-sectional axis. This is related to the thermo-mechanical clamping provided by embedding the SMA wire into a stiff polymer matrix and, hence to the applied external stress. Furthermore, it can also be related to the force transfer between SMA wire with a structured surface and polymer matrix. Preferential planes can be observed in the local radial strain distribution, and the SMA wire does not contract uniformly transversal. This resistance of the polymer matrix to the radial contraction of the SMA wire with a structured surface could also explain the uneven delamination observed over the cross-section area of the SMA wire, as described before.

Everything discussed so far implies an influence of the axial and radial strain applied during the pull-out test to the interfacial failure progression. So, the first interfacial failure seems not only shear stress-induced. This assumption was also made by [113], who postulated that two possibilities exist for the first interfacial failure in an SMAHC, as discussed in section 3.5. The interface fails when either the interfacial shear stress exceeds its maximum shear strength or the interfacial failure is strain driven, i.e., induced by accumulated strain at the SMA wire entry point. Following the first debonding, the theory of brittle fracture propagation can be used to describe the further propagation of the crack tip. This research confirms this assumption by adding the radial contraction of the SMA wire as a third factor relevant to interfacial failures.

8 Summarized Consideration

Comparing the results of the three parts:

- Part 1: Understanding the influence of the selective electrochemical etching process on thermomechanical SMA wire characteristics and measuring the SMA wire surface morphology.
- Part 2: Understanding the influence of the SMA wire surface morphology on the force transfer between the SMA wire and polymer matrix.
- Part 3: Understanding the interfacial failure behavior of an SMAHC during a pull-out test and the influence of the thermomechanical clamping due to embedding the SMA wire within the polymer matrix.

shown in this research and relating them to each other, an overall understanding of the characterization and optimization of the interfacial strength between SMA wire and polymer matrix emerges.

Structuring the SMA wire surface with the selective electrochemical etching process increases the force transfer for all structured SMA wire surface variants shown. The interfacial failure propagation analysis can be further improved using optical measurement methods, such as X-ray μ CT, stress optics, and SEM images. The first interfacial failure occurs for all measurements at the SMA wire entry point, as discussed in section 3.5 and demonstrated in section 7.2. After that, the interfacial failure continues to increase along the embedded SMA wire length. The 3D growth of the interfacial delamination area can be further investigated only with the μ CT *in situ* pull-out test, but only for a limited ROI. This is a new test method developed in this research, enabling a high resolution volume view of the progression of interfacial delamination and the correlation with the change of the SMA wire surface morphology by applying load. The potential of using this combined analysis method to increase the understanding of the interfacial failure progress is demonstrated in section 7.3.

The amount of delamination propagation is not homogeneous in the circumferential direction of the SMA wire at the SMA wire entry point. This non-uniform distribution of the delamination can be explained by the theoretically proposed brittle interfacial failure [41, 156] and the partly non-uniform radial local strain distribution shown in Figure 40. The mechanical laboratory pull-out test showed that the macroscopic homogeneous structuring along the longitudinal axis of the SMA wire can still guarantee good

force transfer even after the first interface failure compared to the SMA wire as delivered. However, this is not evident in the μ CT *in situ* pull-out test due to the stepwise loading and the smaller FoV. Combining both analyses gives a holistic view of the microscopic interfacial failure progression between an SMA wire and a polymer matrix. The μ CT *in situ* pull-out tests show a higher deviation of the force of first failure for Structure S2 (Structures S1 2.2 %, S2 27 %). The force of first failure is significantly lower than in the mechanical laboratory pull-out tests for the SMA wire with a nominal diameter of 0.5 mm. Visual inspection of the μ CT data shows that the force of the first failure decreased by 45.77 %, comparing the μ CT *in situ* pull-out test with the mechanical laboratory pull-out test for Structure S1. The higher deviation of the individual measured values for the μ CT *in situ* pull-out test could be related to the higher resolution in the measurements, the lower number of samples and the lower stiffness of the overall test set-up. The lower force of the first interfacial failure measured is also related to different testing parameters, such as straining rates [52] and the free SMA wire length difference. The influence of the free length of the SMA wire during pull-out test was investigated in [53]. The sample geometry induced boundary effect for different sample polymer matrix dimensions on the resulting interfacial shear stress was analyzed by calculating the interfacial shear stress as described in [50] for the same parameters but by changing the outer polymer matrix dimensions. It was thereby revealed that compared to the mechanical laboratory pull-out test, the interfacial shear stress is underestimated in the μ CT *in situ* pull-out test by approximately 18 %, just by changing the polymer matrix dimensions. This is illustrated also in appendix A.11. It was excluded that post-curing of the polymer induced by the X-ray beam influences the experimental results with a lower force of the first interfacial failure by DSC measurements on samples with and without X-ray exposure (appendix A.2.2).

Analyses of the pulled-out SMA wires by SEM after the mechanical laboratory pull-out test suggested the presence of superimposed adhesive and cohesive interfacial failure behavior. The occurrence of cohesive matrix failure was confirmed by analyzing the image data from the μ CT *in situ* pull-out test, independent of the SMA wire surface structuring configuration, showing polymer matrix cracks. The μ CT analysis shows that the SMA wire surface pits are filled with polymer matrix for the observed FoV. This can also be demonstrated by considering an ion-beam polished cross-section of a non-tested pull-out sample showing no delamination or gap between the SMA wire with a structured surface and the surrounding polymer matrix (appendix A.2.3). The change

in the failure modes between as-delivered SMA wire (adhesive) and surface structured SMA wire (adhesive and cohesive) could also explain the improvement of the interfacial strength, as discussed in section 7.2.

A theoretical study [113] proposed that the interfacial failure in SMAHC is either strain- or shear stress-driven. This research confirms this assumption but also extends the assumption to consider the influence of the radial strains. It is assumed in [11] that the embedded SMA wire can only contract radially after first interfacial failure appears. This research provides evidence that there is a superimposed interfacial failure behavior. The strain values shown from the DVC analysis indicate that the elongation at break of the polymer matrix can contribute to the first interfacial failure.

The detailed characterization of the non-embedded SMA wires also assists in interpreting the pull-out tests. Comparing the determined strain values with the shown macroscopic analysis of the non-embedded SMA wire thermomechanical characteristics (section 7.1.2, Figure 26), it can be seen that the first failure occurs in the second detwinning plateau, where the SMA wire experiences high axial strains at almost constant stress. This research also indicates that the SMA wire is detwinned during the *in situ* pull-out μ CT test (Figure 21, Figure 26, Figure 38 and Figure 39) and exhibits a maximum axial strain in the delaminated area of over 6 % in the ROI. Thus, the interfacial strength depend on the force transfer via the interface itself and the limitations defined by the chosen polymer matrix system.

The analysis of the global radial strain (Figure 38 and Figure 39) shows that pull-out samples with Structure S1 experience the first interfacial failure at a larger radial contraction of the SMA wire compared with Structure S2. Considering the local strain distribution, it seems that the stiff epoxy polymer matrix can retain the SMA wire with Structure S1 more effectively than Structure S2, so only local delamination is possible, depending on the surface structure distribution. To better understand the influence of the applied SMA wire surface structure on the resulting force transfer, the surface pit distribution and size were further analyzed in this research (section 7.1.2, Figure 24). For the SMA wire with a nominal diameter of 1 mm, no influence of the type of applied SMA wire surface structure can be identified using only the force of first failure values (Figure 28). However, looking at the surface-dependent stress values (Table 8), it can be seen that Structure B1 and B2 achieve a better force transfer than Structure B3. This value includes the respective SMA wire diameter and the displacement measured for the sample during the mechanical laboratory pull-out test. Considering the surface-

dependent stress analysis, the best results are achieved for the SMA wire with a nominal diameter of 0.5 mm with the surface Structure S1. The comparability of the two investigated SMA wires (0.5 and 1 mm) with the different structured surfaces is limited because it is not possible to generate an identical surface morphology for different SMA wires. However, the surface shear stress at first failure and the surface-dependent stress analysis show that a smaller SMA wire diameter (0.5 mm) can optimize the interfacial strength. This research demonstrates that surface structuring with small pits and high pit density is desirable and should be applied to an SMA wire with the smallest possible diameter. The applied structuring of the SMA wires results in all cases in an increase of the standard deviations in the two pull-out tests performed. This is related to the small microstructural variations in the distribution of the surface pits. Microscopic analysis reveals that the structure is not homogeneous, which is not apparent in macroscopic analysis. The differences in the local microstructure morphology of the SMA wire surface can be shown by considering the segmentation analysis of the SMA wire cross-section for the ROI (Figure 37). The jagged course of the curve shows that the surface morphology varies locally when viewed microscopically.

The comparison of the tests performed on non-embedded SMA wires with the results of the μ CT *in situ* pull-out test gives a first impression of the influence of the thermo-mechanical clamping of the SMA wire by embedding it in a stiff polymer matrix on the resulting stress-strain characteristics of the SMA wire. As concluded in section 3.6, the influence of the polymer matrix on the SMA wire has been rarely investigated. Through the comparison, analytical considerations of SMAHC can be further adjusted. In particular, the deviation in global radial strain suggests that the previously formulated suggestion that the SMA wire is restrained from radial contraction by the polymer matrix is enhanced [135]. This can be attributed to the omega-shaped pits and the mechanical interlocking between the constituents. By considering the local strain distribution for the embedded and non-embedded SMA wire, another influence of the thermomechanical clamping by the polymer matrix is revealed. The polymer matrix imposes a much more homogeneous strain distribution in the axial direction than the non-embedded SMA wire. This also differs from the results shown in [29], in which the microscopic phase transformation of a NiTi tube is demonstrated. The applied axial strain distribution change could result from the improved force transfer between the surface structured SMA wire and the polymer matrix.

This research leads to new insights regarding the interfacial strength, further supported by the schematic representation in Figure 43. Suppose a good interfacial strength is given between the polymer matrix and the SMA wire. In that case, the resulting pull-out curve in the pull-out test will follow the stress-displacement curve of the pure polymer matrix for a stiff system after the free SMA wire is completely detwinned. After the first interfacial failure occurs (marked with a cross), the shape of the pull-out curve changes depending on the remaining interfacial strength. The stronger the bond between the polymer matrix and the SMA wire, the less steep the decrease in the pull-out curve propagation. In addition, the stiffness of the surrounding polymer matrix plays a major role. If a more elastic polymer matrix is used, the pull-out curves show the stress-strain characteristics of the non-embedded SMA wire more clearly, and possibly even the detwinning plateaus can be seen [128]. Therefore, the pull-out curve propagation is less affected by a failure of the interface. The influence of the force transfer is also lower in this case.

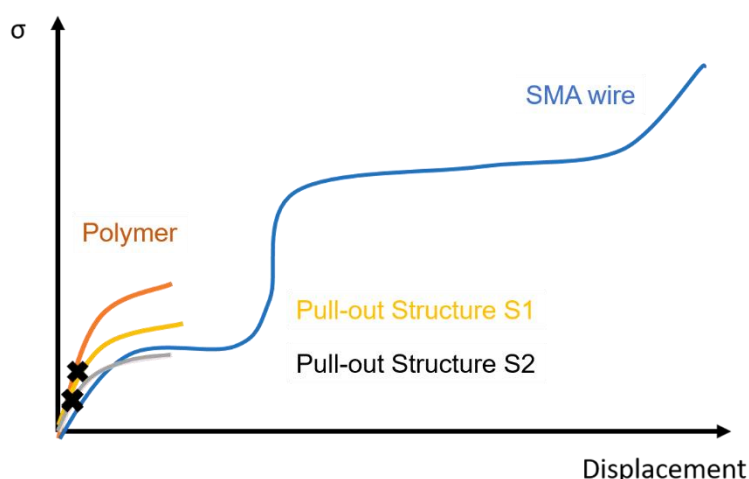


Figure 43: Schematic illustration of the influence of the interfacial strength and the polymer matrix stiffness on the stress-displacement curve propagation observed during the mechanical laboratory pull-out test.

All the results and discussions shown so far allow the conclusion that the first interfacial failure cannot be explained by an interfacial shear stress increase alone. Normal stress generated by the contraction of the SMA wire and the limitation of the polymer matrix concerning the axial maximum strain play an important role and must be considered for improving and characterizing the force transfer between the SMA wire and the polymer matrix.

9 Conclusion & Outlook

In section 4, the aims and strategies of this research were demonstrated. By structuring this research into three main parts, a deeper holistic understanding regarding the influence of the surface treatment used to improve the force transfer on the thermomechanical properties of the SMA wire is generated. This research obtained new insights into the interaction between the SMA wire and the polymer matrix, including a deeper understanding of the progression of interfacial failure in SMAHC. Within this scope, the relationship between surface morphology and optimization of force transmission was also highlighted. Also, the benefit of combining optical methods with micromechanical testing is demonstrated. The influence of the thermomechanical clamping by embedding into a polymer matrix was analyzed by comparing the embedded SMA wire with the non-embedded SMA stress-strain characteristics. The main results can be summarized as follows:

1. Selective electrochemical etching of the SMA wire surface incorporated omega-shaped pits on the SMA wire surface. The outcoming SMA wire surface morphology can be controlled and applied to a macroscopic homogenous and reproducible surface by controlling the etching parameters. The selective electrochemical etching process does not significantly influence the thermomechanical stress-strain characteristics of the SMA wire. Quantifying the applied SMA wire surface morphology helps better understand the influence of the SMA wire surface morphology on the resulting force transfer and the interfacial failure process.
2. By surface structuring the SMA wires, a better force transfer can be achieved mainly caused by the mechanical interlocking between the SMA wire and the polymer matrix, resulting in a superimposed cohesive and adhesive interfacial failure mode. The applied SMA wire surface structure morphology does influence the amount of force transfer. Smaller pit sizes with a high pit density result in better interfacial force transfer. Structuring the SMA wire surface improves the force-bearing capacity after the first interfacial failure and improves force transfer until the whole interface fails. For a better comparison between the different structured SMA wire surface variants and the two different nominal diameters tested in this research, the calculated interfacial shear stress and the self-

defined parameter surface-dependent stress help to compare the measurements and gain a deeper understanding.

3. Using μ CT analysis in combination with stepwise increasing the load during the pull-out test gives deeper insights into the interfacial failure progression during the pull-out test. The growth of the amount of delamination over the volume during the test can be observed and quantified for the entire observed ROI. Moreover, the global and local axial and radial strains for the embedded SMA wire part of the sample can be measured using DVC analysis. Using DVC analysis, it could be shown that the polymer matrix constrains the SMA wire from radial contraction, and the axial strain is in the range of the elongation of break of the polymer matrix. Good interfacial strength between SMA wire and polymer matrix influences the stress-strain characteristics of the SMA wire and a different behavior can be observed. In this part of the research, the number of samples and the analyzed samples were limited. More samples have to be tested to support the findings, and further analyses must be done. However, this research shows the potential of using μ CT *in situ* testing to understand micromechanical failure progression better.

The resulting research questions can be answered by incorporating all results gained from the three parts of this research.

1. **Does selective electrochemical etching of the SMA wire alter its thermo-mechanical properties?** → No, for the tested characteristics, no significant change can be observed.
2. **Does the surface structuring of the SMA wire improve the interfacial strength, and if so, can this improvement be attributed to specific features of the surface morphology?** → The force transfer between SMA wire and polymer matrix can be improved by incorporating a surface structure morphology on the SMA wire surface. The difference between the tests made with the as-delivered and the SMA wires with a structured surface is more prominent for the SMA wires with a nominal diameter of 1 mm for the first interfacial failure by only considering the force of the first interfacial failure as quantity. The self-defined quantity surface-dependent stress helps to compare the different SMA wire diameters considered in this research. The applied surface structure improves the force-bearing capacity after the first interfacial failure, which can be shown for

all tested samples with the mechanical laboratory pull-out test. The best surface-dependent stress transfer can be achieved using a surface structure with small pit sizes and high pit distribution with the SMA wire with a nominal diameter of 0.5 mm.

3. **Can optical quantification and monitoring of the structured surface of the SMA wire, obtained during the mechanical pull-out test, provide a better insight into the micromechanical interfacial failure processes?** → Optical monitoring methods help to gain a deeper understanding by observing the interfacial failure progress. The applied strain and the resulting interfacial failure can be correlated. For all tested samples, additionally, the first and complete interfacial failure can be measured and compared by using optical methods.
4. **Furthermore, does the surface structuring of the SMA wire contribute to a more comprehensive understanding of the interaction between the SMA wire and the polymer matrix and does it reveal whether the failure of the interface is stress- or strain-induced?** → The results of combined methods conclude that the first interfacial failure can have different reasons: the exceeding of the interfacial shear stress, the exceeding of the elongation of break of the polymer matrix or the radial contraction of the SMA wire. It is difficult to assess which factors led to the interface failure in each case. A superimposed interfacial failure behavior is also considered possible.

The statements made in this research are based on the described results (section 7). Time restrictions and the availability of the test set-up and cooperating partners limited the possibilities for performing and analyzing the μ CT *in situ* pull-out tests. However, the conclusions made are supported by the mechanical laboratory pull-out tests. The tests show the potential of such combined investigations. The conclusions drawn require additional investigations and analyses for statistical validation. In particular, further studies focusing on the effects of surface structuring of the SMA wire in a cyclic interface test are required. In addition, the effects of temperature application and the inclusion of phase transformation in the pull-out test need to be investigated. Furthermore, the conclusions should be examined in a real SMAHC during the deformation test.

Some of the questions raised here were already analyzed in a first investigation that was not integrated into this research. A two-way effect SMA wire structured by selective electrochemical etching was compared with the same SMA wire in the as-delivered

surface condition. The mechanical laboratory pull-out test, a thermal-induced pull-out test and a cyclical-induced pull-out test were performed. The results are indicating that the results shown in this research can be transferred to a real SMAHC and that the surface structuring can also increase the durability of the interface.

References

- [1] P. Šittner and R. Stalmans, "Developing hybrid polymer composites with embedded shape-memory alloy wires," *JOM*, vol. 52, no. 10, pp. 15–20, Oct. 2000, doi: 10.1007/s11837-000-0077-1.
- [2] M. Gurka, *The physics of multifunctional materials: concepts, materials, applications*. Lancaster, Pennsylvania: DEStech Publications, Inc., 2019.
- [3] Lagoudas, D. C., *Shape Memory Alloys*, vol. 1. Boston, MA: Springer US, 2008. doi: 10.1007/978-0-387-47685-8.
- [4] G. Faiella, V. Antonucci, F. Daghia, S. Fascia, and M. Giordano, "Fabrication and Thermo-Mechanical Characterization of a Shape Memory Alloy Hybrid Composite," *J. Intell. Mater. Syst. Struct.*, vol. 22, pp. 245–252, Feb. 2011, doi: 10.1177/1045389X10396954.
- [5] D. Baitab, D. L. A. H. A. Majid, E. Abdullah, and M. Hamid, "A review of techniques for embedding shape memory alloy (SMA) wires in smart woven composites," *Int. J. Eng. Technol.*, vol. 7, pp. 129–136, Oct. 2018, doi: 10.14419/ijet.v7i4.13.21344.
- [6] D. J. Hartl and D. C. Lagoudas, "Aerospace applications of shape memory alloys," *Proc. Inst. Mech. Eng. Part G J. Aerosp. Eng.*, vol. 221, no. 4, pp. 535–552, Apr. 2007, doi: 10.1243/09544100JAERO211.
- [7] D. Stoeckel, "Shape memory actuators for automotive applications," *Mater. Des.*, vol. 11, no. 6, pp. 302–307, Dec. 1990, doi: 10.1016/0261-3069(90)90013-A.
- [8] S. Nissle, M. Kaiser, M. Hübler, M. Gurka, and U. Breuer, "Adaptive vortex generators based on active hybrid composites: from idea to flight test," *CEAS Aeronaut. J.*, vol. 9, no. 4, pp. 661–670, Dec. 2018, doi: 10.1007/s13272-018-0316-1.
- [9] Y. Wang, L. Zhou, Z. Wang, H. Huang, and L. Ye, "Analysis of internal stresses induced by strain recovery in a single SMA fiber–matrix composite," *Compos. Part B Eng.*, vol. 42, no. 5, pp. 1135–1143, Jul. 2011, doi: 10.1016/j.compositesb.2011.03.017.
- [10] K. Jonnalagadda, G. E. Kline, and N. R. Sottos, "Local displacements and load transfer in shape memory alloy composites," *Exp. Mech.*, vol. 37, no. 1, pp. 78–86, Mar. 1997, doi: 10.1007/BF02328753.
- [11] Y. Payandeh, F. Meraghni, E. Patoor, and A. Eberhardt, "Effect of martensitic transformation on the debonding propagation in Ni–Ti shape memory wire composite," *Mater. Sci. Eng. A*, vol. 518, no. 1, pp. 35–40, Aug. 2009, doi: 10.1016/j.msea.2009.04.019.
- [12] K. Neuking, A. Abu-Zarifa, and G. Eggeler, "Surface engineering of shape memory alloy/polymer-composites: Improvement of the adhesion between polymers and pseudoelastic shape memory alloys," *Mater. Sci. Eng. A*, vol. 481–482, pp. 606–611, May 2008, doi: 10.1016/j.msea.2007.05.118.
- [13] S. Nissle and M. Gurka, "Characterization of active hybrid structures made of fiber reinforced composites and shape memory alloys-part A: Characterization of the load transfer," *Smart Mater. Struct.*, vol. 28, no. 4, 2019, doi: 10.1088/1361-665X/ab04db.
- [14] S. Marfia and E. Sacco, "Micromechanics and Homogenization of SMA-Wire-Reinforced Materials," *J. Appl. Mech.-Trans. Asme - J APPL MECH*, vol. 72, Mar. 2005, doi: 10.1115/1.1839186.

- [15] J. Mohd Jani, M. Leary, A. Subic, and M. A. Gibson, "A review of shape memory alloy research, applications and opportunities," *Mater. Des. 1980-2015*, vol. 56, pp. 1078–1113, Apr. 2014, doi: 10.1016/j.matdes.2013.11.084.
- [16] J. Van Humbeeck, "Non-medical applications of shape memory alloys," *Mater. Sci. Eng. A*, vol. 273–275, pp. 134–148, Dec. 1999, doi: 10.1016/S0921-5093(99)00293-2.
- [17] F. A. M. Ghazali, M. N. Hasan, T. Rehman, M. Nafea, M. S. M. Ali, and K. Takahata, "MEMS actuators for biomedical applications: a review," *J. Micromechanics Microengineering*, vol. 30, no. 7, p. 073001, May 2020, doi: 10.1088/1361-6439/ab8832.
- [18] M. Leester-Schädel, B. Hoxhold, C. Lesche, S. Demming, and S. Büttgenbach, "Micro actuators on the basis of thin SMA foils," *Microsyst. Technol.*, vol. 14, no. 4, pp. 697–704, Apr. 2008, doi: 10.1007/s00542-008-0600-9.
- [19] M. Sreekumar, T. Nagarajan, M. Singaperumal, M. Zoppi, and R. Molfini, "Critical review of current trends in shape memory alloy actuators for intelligent robots," *Ind. Robot Int. J.*, vol. 34, pp. 285–294, Jun. 2007, doi: 10.1108/01439910710749609.
- [20] H. Rodrigue, W. Wang, M.-W. Han, T. J. Y. Kim, and S.-H. Ahn, "An Overview of Shape Memory Alloy-Coupled Actuators and Robots," *Soft Robot.*, vol. 4, no. 1, pp. 3–15, Mar. 2017, doi: 10.1089/soro.2016.0008.
- [21] M. Hübler, S. Nissle, M. Gurka, and J. Wassenaar, "Active vortex generator deployed on demand by size independent actuation of shape memory alloy wires integrated in fiber reinforced polymers," in *Industrial and Commercial Applications of Smart Structures Technologies 2016*, International Society for Optics and Photonics, 2016, p. 98010G.
- [22] C. Song, "History and Current Situation of Shape Memory Alloys Devices for Minimally Invasive Surgery," *Open Med Dev J*, vol. 2, pp. 24–31, Feb. 2010, doi: 10.2174/1875181401002020024.
- [23] R. B. Zider and J. F. Krumme, "Eyeglass Frame including Shape Memory Elements," 4,772,112, 1988
- [24] D. Stoeckel, A. Pelton, and T. Duerig, "Self-expanding nitinol stents: material and design considerations," *Eur. Radiol.*, vol. 14, no. 2, pp. 292–301, Feb. 2004, doi: 10.1007/s00330-003-2022-5.
- [25] J. Huber, N. Fleck, and M. Ashby, "The selection of mechanical actuators based on performance indices," *Proc. R. Soc. Lond. Ser. Math. Phys. Eng. Sci.*, 1997, doi: 10.1098/rspa.1997.0117.
- [26] P. Chowdhury and H. Sehitoglu, "Deformation physics of shape memory alloys – Fundamentals at atomistic frontier," *Prog. Mater. Sci.*, vol. 88, pp. 49–88, Jul. 2017, doi: 10.1016/j.pmatsci.2017.03.003.
- [27] F. Barrie, D. B. Futch, D. H. D. Hsu, and M. V. Manuel, "Effect of phase on debond strength in shape memory alloy reinforced composites," *Mater. Des.*, vol. 57, pp. 98–102, May 2014, doi: 10.1016/j.matdes.2013.11.062.
- [28] M. Sinapius, *Adaptronik: Prinzipie - Funktionswerkstoffe - Funktionselemente - Zielfelder mit Forschungsbeispielen*. Berlin [Heidelberg]: Springer Vieweg, 2018.
- [29] N. J. Bechle and S. Kyriakides, "Localization in NiTi tubes under bending," *Int. J. Solids Struct.*, vol. 51, no. 5, pp. 967–980, Mar. 2014, doi: 10.1016/j.ijsolstr.2013.11.023.
- [30] S. Miyazaki and K. Otsuka, "Deformation and transition behavior associated with the R-phase in Ti-Ni alloys," *Metall. Trans. A*, vol. 17, no. 1, pp. 53–63, Jan. 1986, doi: 10.1007/BF02644442.

- [31] K. Otsuka, Ed., *Shape memory materials*, 1. paperback ed. (with corr.), Transferred in digital print. Cambridge: Cambridge University Press, 2002.
- [32] L. T. Drzal and M. Madhukar, "Fibre-matrix adhesion and its relationship to composite mechanical properties," *J. Mater. Sci.*, vol. 28, no. 3, pp. 569–610, Feb. 1993, doi: 10.1007/BF01151234.
- [33] F. Teklal, A. Djebbar, S. Allaoui, G. Hivet, Y. Joliff, and B. Kacimi, "A review of analytical models to describe pull-out behavior – Fiber/matrix adhesion," *Compos. Struct.*, vol. 201, pp. 791–815, Oct. 2018, doi: 10.1016/j.compstruct.2018.06.091.
- [34] S. A. Toro, A. Ridruejo, C. González, and J. P. Fernández Blázquez, "Effect of Fiber-Matrix Interface on the Mechanical Response of a Woven Carbon Fiber/PEEK Composite Material," *Materials*, vol. 15, no. 20, p. 7340, Oct. 2022, doi: 10.3390/ma15207340.
- [35] B. Pukánszky, "Influence of interface interaction on the ultimate tensile properties of polymer composites," *Composites*, vol. 21, no. 3, pp. 255–262, May 1990, doi: 10.1016/0010-4361(90)90240-W.
- [36] Z. J. Wu, J. Q. Ye, and J. G. Cabrera, "3D analysis of stress transfer in the micromechanics of fiber reinforced composites by using an eigen-function expansion method," *J. Mech. Phys. Solids*, vol. 48, no. 5, pp. 1037–1063, May 2000, doi: 10.1016/S0022-5096(99)00058-7.
- [37] L. T. Drzal, M. J. Rich, and P. F. Lloyd, "Adhesion of Graphite Fibers to Epoxy Matrices: I. The Role of Fiber Surface Treatment," *J. Adhes.*, vol. 16, no. 1, pp. 1–30, Jul. 1983, doi: 10.1080/00218468308074901.
- [38] S. Huang, Q. Fu, L. Yan, and B. Kasal, "Characterization of interfacial properties between fibre and polymer matrix in composite materials – A critical review," *J. Mater. Res. Technol.*, vol. 13, pp. 1441–1484, Jul. 2021, doi: 10.1016/j.jmrt.2021.05.076.
- [39] J. Vogtmann, A. Klingler, T. Rief, and M. Gurka, "3D X-ray Microscopy as a Tool for in Depth Analysis of the Interfacial Interaction between a Single Carbon Fiber and an Epoxy Matrix after Mechanical Loading," *J. Compos. Sci.*, vol. 5, no. 5, Art. no. 5, May 2021, doi: 10.3390/jcs5050121.
- [40] W. Beckert and B. Lauke, "Critical discussion of the single-fibre pull-out test: does it measure adhesion?," *Compos. Sci. Technol.*, vol. 57, no. 12, pp. 1689–1706, Jan. 1998, doi: 10.1016/S0266-3538(97)00107-3.
- [41] M. J. Lodeiro, S. Maudgal, L. N. McCartney, R. Morrell, and B. Roebuck, "Critical Review of Interface Testing Methods for Composites".
- [42] A. Kelly and W. R. Tyson, "Tensile properties of fibre-reinforced metals: Copper/tungsten and copper/molybdenum," *J. Mech. Phys. Solids*, vol. 13, no. 6, pp. 329–350, Dec. 1965, doi: 10.1016/0022-5096(65)90035-9.
- [43] B. Miller, P. Muri, and L. Rebenfeld, "A microbond method for determination of the shear strength of a fiber/resin interface," *Compos. Sci. Technol.*, vol. 28, no. 1, pp. 17–32, Jan. 1987, doi: 10.1016/0266-3538(87)90059-5.
- [44] G. P. Tandon and N. J. Pagano, "Micromechanical analysis of the fiber push-out and re-push test," *Compos. Sci. Technol.*, vol. 58, no. 11, pp. 1709–1725, Nov. 1998, doi: 10.1016/S0266-3538(98)00037-2.
- [45] L. J. Broutman, "Glass-resin joint strength and their effect on failure mechanisms in reinforced plastics," *Polym. Eng. Sci.*, vol. 6, no. 3, pp. 263–272, Jul. 1966, doi: 10.1002/pen.760060316.

- [46] L. S. Penn and E. R. Bowler, "A new approach to surface energy characterization for adhesive performance prediction," *Surf. Interface Anal.*, vol. 3, no. 4, pp. 161–164, Aug. 1981, doi: 10.1002/sia.740030405.
- [47] J. Beter, B. Schritteser, B. Maroh, E. Sarlin, P. F. Fuchs, and G. Pinter, "Comparison and Impact of Different Fiber Debond Techniques on Fiber Reinforced Flexible Composites," *Polymers*, vol. 12, no. 2, Art. no. 2, Feb. 2020, doi: 10.3390/polym12020472.
- [48] B. F. Sørensen and H. Lilholt, "Fiber pull-out test and single fiber fragmentation test - analysis and modelling," *IOP Conf. Ser. Mater. Sci. Eng.*, vol. 139, p. 012009, Jul. 2016, doi: 10.1088/1757-899X/139/1/012009.
- [49] S. Nissle, "Zur Kraftübertragung zwischen NiTi-Formgedächtnislegierungen und Faserkunststoffverbunden in aktiven Hybridstrukturen," 2019.
- [50] L. B. Greszczuk, "Theoretical Studies of the Mechanics of the Fiber-Matrix Interface in Composites," in *Interfaces in Composites*, Committee D-30, Ed., 100 Barr Harbor Drive, PO Box C700, West Conshohocken, PA 19428-2959: ASTM International, 1969, pp. 42-42–17. doi: 10.1520/STP44699S.
- [51] L.-M. Zhou, J.-K. Kim, and Y.-W. Mai, "On the single fibre pull-out problem: effect of loading method," *Compos. Sci. Technol.*, vol. 45, no. 2, pp. 153–160, Jan. 1992, doi: 10.1016/0266-3538(92)90037-4.
- [52] H. Fathi, M. M. Shokrieh, and A. Saeedi, "Effect of tensile loading rate on interfacial properties of SMA/polymer composites," *Compos. Part B Eng.*, vol. 183, p. 107730, Feb. 2020, doi: 10.1016/j.compositesb.2019.107730.
- [53] H. V. Ho, E. Choi, and J. W. Kang, "Analytical bond behavior of cold drawn SMA crimped fibers considering embedded length and fiber wave depth," *Rev. Adv. Mater. Sci.*, vol. 60, no. 1, pp. 862–883, Jan. 2021, doi: 10.1515/rams-2021-0066.
- [54] H. Wang, G. Tian, H. Wang, W. Li, and Y. Yu, "Pull-out method for direct measuring the interfacial shear strength between short plant fibers and thermoplastic polymer composites (TPC)," *Holzforschung*, vol. 68, Jan. 2014, doi: 10.1515/hf-2013-0052.
- [55] C. Ageorges, K. Friedrich, T. Schüller, and B. Lauke, "Single-fibre Broutman test: fibre–matrix interface transverse debonding," *Compos. Part Appl. Sci. Manuf.*, vol. 30, no. 12, pp. 1423–1434, Dec. 1999, doi: 10.1016/S1359-835X(99)00045-7.
- [56] S. Zhandarov, "Characterization of fiber/matrix interface strength: applicability of different tests, approaches and parameters," *Compos. Sci. Technol.*, vol. 65, no. 1, pp. 149–160, Jan. 2005, doi: 10.1016/j.compscitech.2004.07.003.
- [57] H. L. Cox, "The elasticity and strength of paper and other fibrous materials," *Br. J. Appl. Phys.*, vol. 3, no. 3, p. 72, Mar. 1952, doi: 10.1088/0508-3443/3/3/302.
- [58] J. A. Nairn and D. A. Mendels, "On the use of planar shear-lag methods for stress-transfer analysis of multilayered composites," *Mech. Mater.*, vol. 33, no. 6, pp. 335–362, Jun. 2001, doi: 10.1016/S0167-6636(01)00056-4.
- [59] J. O. Outwater and M. C. Murphy, "Fracture energy of unidirectional laminates.," vol. Modern Plastics, no. September Issue, pp. 160–168, 1970.
- [60] P.-F. Liu, X.-Z. Yu, Y.-M. Guo, and W.-M. Tao, "Interface debonding criteria in SiC fiber-reinforced composites," *Zhejiang Daxue Xuebao Gongxue Ban Journal Zhejiang Univ. Eng. Sci.*, vol. 40, pp. 1883–1888, Nov. 2006.
- [61] C.-H. Hsueh, "Stress Transfer from Axially Loaded Fiber to Matrix in a Microcomposite," *MRS Proc.*, vol. 365, p. 217, 1994, doi: 10.1557/PROC-365-217.

- [62] G. P. Tandon, R. Y. Kim, S. G. Warriar, and B. S. Majumdar, "Influence of free edge and corner singularities on interfacial normal strength: application in model unidirectional composites," *Compos. Part B Eng.*, vol. 30, no. 2, pp. 115–134, Mar. 1999, doi: 10.1016/S1359-8368(98)00046-8.
- [63] F. C. Antico, P. D. Zavattieri, L. G. Hector Jr, A. Mance, W. R. Rodgers, and D. A. Okonski, "Adhesion of nickel–titanium shape memory alloy wires to thermoplastic materials: theory and experiments," *Smart Mater. Struct.*, vol. 21, no. 3, p. 035022, Mar. 2012, doi: 10.1088/0964-1726/21/3/035022.
- [64] S.-Y. Fu, C.-Y. Yue, X. Hu, and Y.-W. Mai, "Analyses of the micromechanics of stress transfer in single- and multi-fiber pull-out tests," *Compos. Sci. Technol.*, vol. 60, no. 4, pp. 569–579, Mar. 2000, doi: 10.1016/S0266-3538(99)00157-8.
- [65] S. C. Garcea, Y. Wang, and P. J. Withers, "X-ray computed tomography of polymer composites," *Compos. Sci. Technol.*, vol. 156, pp. 305–319, Mar. 2018, doi: 10.1016/j.compscitech.2017.10.023.
- [66] O. Brunke, "High-resolution CT-based defect analysis and dimensional measurement," *Insight*, vol. 52, pp. 91–93, Feb. 2010, doi: 10.1784/insi.2010.52.2.91.
- [67] A. Singhal, J. C. Grande, and Y. Zhou, "Micro/Nano-CT for Visualization of Internal Structures," *Microsc. Today*, vol. 21, no. 2, pp. 16–22, Mar. 2013, doi: 10.1017/S1551929513000035.
- [68] J. Glinz, S. Zabler, J. Kastner, and S. Senck, "Metal Artifacts in Attenuation and Phase Contrast X-Ray Microcomputed Tomography: A Comparative Study," *Exp. Mech.*, vol. 62, no. 5, pp. 837–847, Jun. 2022, doi: 10.1007/s11340-022-00835-9.
- [69] A. Rashidi, T. Olfatbakhsh, B. Crawford, and A. S. Milani, "A Review of Current Challenges and Case Study toward Optimizing Micro-Computed X-Ray Tomography of Carbon Fabric Composites," *Materials*, vol. 13, no. 16, p. 3606, Aug. 2020, doi: 10.3390/ma13163606.
- [70] B. Leszczynski, J. Skrzat, M. Kozerska, A. Wrobel, and J. Walocha, "Three dimensional visualisation and morphometry of bone samples studied in microcomputed tomography (micro-CT)," *Folia Morphol.*, vol. 73, pp. 422–428, Dec. 2014, doi: 10.5603/FM.2014.0064.
- [71] N. Ida and N. Meyendorf, Eds., *Handbook of Advanced Nondestructive Evaluation*. Cham: Springer International Publishing, 2019. doi: 10.1007/978-3-319-26553-7.
- [72] J. Hsieh, *Computed Tomography: Principles, Design, Artifacts, and Recent Advances*. SPIE Press, 2003.
- [73] E. Van de Casteele, "Model-based approach for beam hardening correction and resolution measurements in microtomography," Jan. 2004.
- [74] L. Gjestebj et al., "Metal Artifact Reduction in CT: Where Are We After Four Decades?," *IEEE Access*, vol. 4, pp. 5826–5849, 2016, doi: 10.1109/ACCESS.2016.2608621.
- [75] M. C. Seghini, F. Touchard, F. Sarasini, L. Chocinski-Arnault, D. Mellier, and J. Tirillò, "Interfacial adhesion assessment in flax/epoxy and in flax/vinylester composites by single yarn fragmentation test: Correlation with micro-CT analysis," *Compos. Part Appl. Sci. Manuf.*, vol. 113, pp. 66–75, 2018, doi: 10.1016/j.compositesa.2018.07.015.
- [76] "Microscale 3D Strain Mapping at Fiber-Matrix Interface using Synchrotron Computed Tomography and Digital Volume Correlation - KU Leuven." Accessed: Apr. 14, 2023. [Online]. Available: https://kuleuven.limo.libis.be/discovery/fulldisplay/lirias3971086/32KUL_KUL:Lirias

- [77] S. C. Garcea, I. Sinclair, and S. M. Spearing, "In situ synchrotron tomographic evaluation of the effect of toughening strategies on fatigue micromechanisms in carbon fibre reinforced polymers," *Compos. Sci. Technol.*, vol. 109, pp. 32–39, Mar. 2015, doi: 10.1016/j.compscitech.2015.01.012.
- [78] S. Yu, Y. H. Hwang, J. Y. Hwang, and S. H. Hong, "Analytical study on the 3D-printed structure and mechanical properties of basalt fiber-reinforced PLA composites using X-ray microscopy," *Compos. Sci. Technol.*, vol. 175, pp. 18–27, May 2019, doi: 10.1016/j.compscitech.2019.03.005.
- [79] C. Becker, J. Hausmann, J. Krummenacker, and N. Motsch-Eichmann, "First Conclusions on Damage Behaviour of Recycled Carbon Staple Fibre Yarn Using X-ray and Acoustic Emission Techniques," *Materials*, vol. 16, no. 13, p. 4842, Jul. 2023, doi: 10.3390/ma16134842.
- [80] C. B. Churchill, J. A. Shaw, and M. A. Iadicola, "Tips and tricks for characterizing shape memory alloy wire: part 2-fundamental isothermal responses," *Exp. Tech.*, vol. 33, no. 1, pp. 51–62, Jan. 2009, doi: 10.1111/j.1747-1567.2008.00460.x.
- [81] J. A. Shaw, C. B. Churchill, and M. A. Iadicola, "Tips and tricks for characterizing shape memory alloy wire: part 2-fundamental isothermal responses: part 1 differential scanning calorimetry and basic phenomena," *Exp. Tech.*, vol. 32, no. 5, pp. 55–62, Sep. 2008, doi: 10.1111/j.1747-1567.2008.00410.x.
- [82] C. B. Churchill, J. A. Shaw, and M. A. Iadicola, "Tips and tricks for characterizing shape memory alloy wire: part 3- localization and propagation phenomena," *Exp. Tech.*, vol. 33, no. 5, pp. 70–78, Sep. 2009, doi: 10.1111/j.1747-1567.2009.00558.x.
- [83] O. Benafan *et al.*, "Shape memory alloy actuator design: CASMART collaborative best practices and case studies," *Int. J. Mech. Mater. Des.*, vol. 10, no. 1, pp. 1–42, Mar. 2014, doi: 10.1007/s10999-013-9227-9.
- [84] G. Faiella, V. Antonucci, F. Daghia, S. Fascia, and M. Giordano, "Fabrication and Thermo-Mechanical Characterization of a Shape Memory Alloy Hybrid Composite," *J. Intell. Mater. Syst. Struct.*, vol. 22, no. 3, pp. 245–252, Feb. 2011, doi: 10.1177/1045389X10396954.
- [85] M. Hübler, *Methodik zur Auslegung und Herstellung von aktiven SMA-FKV-Hybridverbunden*, Als Manuskript gedruckt. in IVW-Schriftenreihe, no. Band 118. Kaiserslautern: Institut für Verbundwerkstoffe GmbH, 2015.
- [86] A. Pequegnat, A. Michael, J. Wang, K. Lian, Y. Zhou, and M. I. Khan, "Surface characterizations of laser modified biomedical grade NiTi shape memory alloys," *Mater. Sci. Eng. C*, vol. 50, pp. 367–378, May 2015, doi: 10.1016/j.msec.2015.01.085.
- [87] M. Hübler, M. Gurka, and U. P. Breuer, "From attached shape memory alloy wires to integrated active elements, a small step? Impact of local effects on direct integration in fiber reinforced plastics," *J. Compos. Mater.*, vol. 49, no. 15, pp. 1895–1905, Jun. 2015, doi: 10.1177/0021998314550494.
- [88] D. Favier, H. Louche, P. Schlosser, L. Orgéas, P. Vacher, and L. Debove, "Homogeneous and heterogeneous deformation mechanisms in an austenitic polycrystalline Ti–50.8at.% Ni thin tube under tension. Investigation via temperature and strain fields measurements," *Acta Mater.*, vol. 55, no. 16, pp. 5310–5322, Sep. 2007, doi: 10.1016/j.actamat.2007.05.027.

- [89] C. L. Moore and H. A. Bruck, "A fundamental investigation into large strain recovery of one-way shape memory alloy wires embedded in flexible polyurethanes," *Smart Mater. Struct.*, vol. 11, no. 1, pp. 130–139, Feb. 2002, doi: 10.1088/0964-1726/11/1/315.
- [90] B. K. Bay, T. S. Smith, D. P. Fyhrie, and M. Saad, "Digital volume correlation: Three-dimensional strain mapping using X-ray tomography," *Exp. Mech.*, vol. 39, no. 3, pp. 217–226, Sep. 1999, doi: 10.1007/BF02323555.
- [91] Z. Wang *et al.*, "In situ synchrotron X-ray diffraction analysis of two-way shape memory effect in Nitinol," *Mater. Sci. Eng. A*, vol. 878, p. 145226, Jun. 2023, doi: 10.1016/j.msea.2023.145226.
- [92] X. Kong *et al.*, "In-situ high energy X-ray diffraction study of microscopic deformation behavior of martensite variant reorientation in NiTi wire," *Appl. Mater. Today*, vol. 22, p. 100904, Mar. 2021, doi: 10.1016/j.apmt.2020.100904.
- [93] M. Kaiser, "Transient electro-thermomechanical modeling of shape adaptive Shape Memory Alloy Hybrid Composites under influence of ambient temperature and static external load," Rheinland-Pfälzische Technische Universität Kaiserslautern-Landau, 2023. doi: 10.26204/KLUEDO/7520.
- [94] S. J. Furst and S. Seelecke, "Modeling and experimental characterization of the stress, strain, and resistance of shape memory alloy actuator wires with controlled power input," *J. Intell. Mater. Syst. Struct.*, vol. 23, no. 11, pp. 1233–1247, Jul. 2012, doi: 10.1177/1045389X12445036.
- [95] S. Qiu, B. Clausen, S. A. Padula, R. D. Noebe, and R. Vaidyanathan, "On elastic moduli and elastic anisotropy in polycrystalline martensitic NiTi," *Acta Mater.*, vol. 59, no. 13, pp. 5055–5066, Aug. 2011, doi: 10.1016/j.actamat.2011.04.018.
- [96] N. Hatcher, O. Yu. Kontsevoi, and A. J. Freeman, "Role of elastic and shear stabilities in the martensitic transformation path of NiTi," *Phys. Rev. B*, vol. 80, no. 14, p. 144203, Oct. 2009, doi: 10.1103/PhysRevB.80.144203.
- [97] S. Spinner and A. G. Rozner, "Elastic Properties of NiTi as a Function of Temperature," *J. Acoust. Soc. Am.*, vol. 40, no. 5, pp. 1009–1015, Jul. 2005, doi: 10.1121/1.1910180.
- [98] A. Stebner, X. Gao, D. W. Brown, and L. C. Brinson, "Neutron diffraction studies and multivariant simulations of shape memory alloys: Empirical texture development–mechanical response relations of martensitic nickel–titanium," *Acta Mater.*, vol. 59, no. 7, pp. 2841–2849, Apr. 2011, doi: 10.1016/j.actamat.2011.01.023.
- [99] M. F. Ashby and Y. J. M. Bréchet, "Designing hybrid materials," *Acta Mater.*, vol. 51, no. 19, pp. 5801–5821, Nov. 2003, doi: 10.1016/S1359-6454(03)00441-5.
- [100] M. Neitzel, P. Mitschang, and U. Breuer, *Handbuch Verbundwerkstoffe: Werkstoffe, Verarbeitung, Anwendung*. Carl Hanser Verlag GmbH Co KG, 2014.
- [101] AVK – Industrievereinigung Verstärkte Kunststoffe e. V., Ed., *Handbuch Faser-verbundkunststoffe/Composites*. Wiesbaden: Springer Fachmedien Wiesbaden, 2013. doi: 10.1007/978-3-658-02755-1.
- [102] A. Cohades and V. Michaud, "Shape memory alloys in fibre-reinforced polymer composites," *Adv. Ind. Eng. Polym. Res.*, vol. 1, no. 1, pp. 66–81, Oct. 2018, doi: 10.1016/j.aiepr.2018.07.001.
- [103] J. Bhaskar, A. Kumar Sharma, B. Bhattacharya, and S. Adhikari, "A review on shape memory alloy reinforced polymer composite materials and structures," *Smart Mater. Struct.*, vol. 29, no. 7, p. 073001, Jul. 2020, doi: 10.1088/1361-665X/ab8836.

- [104] B. Lester, T. Baxevanis, Y. Chemisky, and D. Lagoudas, "Review and Perspectives: Shape Memory Alloy Composite Systems," *Acta Mech.*, vol. 226, Jul. 2015, doi: 10.1007/s00707-015-1433-0.
- [105] J. Paine, W. Jones, and C. Rogers, "Nitinol actuator to host composite interfacial adhesion in adaptive hybrid composites," in *33rd Structures, Structural Dynamics and Materials Conference*, Dallas, TX, U.S.A.: American Institute of Aeronautics and Astronautics, Apr. 1992. doi: 10.2514/6.1992-2405.
- [106] Z. G. Wei, R. Sandstrom, and S. Miyazaki, "Shape memory materials and hybrid composites for smart systems: Part II Shape-memory hybrid composites," *J. Mater. Sci.*, vol. 33, no. 15, pp. 3763–3783, Aug. 1998, doi: 10.1023/A:1004674630156.
- [107] N. Pattar and S. F. Patil, "Review on fabrication and mechanical characterization of shape memory alloy hybrid composites," *Adv. Compos. Hybrid Mater.*, vol. 2, no. 4, pp. 571–585, Dec. 2019, doi: 10.1007/s42114-019-00119-2.
- [108] F. Daghia, D. J. Inman, F. Ubertini, and E. Viola, "Shape Memory Alloy Hybrid Composite Plates for Shape and Stiffness Control," *J. Intell. Mater. Syst. Struct.*, vol. 19, no. 5, pp. 609–619, May 2008, doi: 10.1177/1045389X07077901.
- [109] M. Kaiser, M. Kunzler, and M. Gurka, "Experimentally characterization and theoretical modeling of the electro-thermomechanical coupling of unimorph Shape Memory Active Hybrid composites," no. Composites Science and Technology, Aug. 2023, doi: 10.1016/j.compscitech.2023.110186.
- [110] Z. Chaudhry and C. A. Rogers, "Bending and Shape Control of Beams Using SMA Actuators," *J. Intell. Mater. Syst. Struct.*, vol. 2, no. 4, pp. 581–602, Oct. 1991, doi: 10.1177/1045389X9100200410.
- [111] C. Poon, K. Lau, and L. Zhou, "Design of pull-out stresses for prestrained SMA wire/polymer hybrid composites," *Compos. Part B Eng.*, vol. 36, no. 1, pp. 25–31, Jan. 2005, doi: 10.1016/j.compositesb.2004.04.002.
- [112] Y. Payandeh, F. Meraghni, E. Patoor, and A. Eberhardt, "Study of the martensitic transformation in NiTi–epoxy smart composite and its effect on the overall behavior," *Mater. Des.*, vol. 39, pp. 104–110, Aug. 2012, doi: 10.1016/j.matdes.2012.02.041.
- [113] M. Merlin, M. Scoponi, C. Soffritti, A. Fortini, R. Rizzoni, and G. L. Garagnani, "On the improved adhesion of NiTi wires embedded in polyester and vinylester resins," *Frat. Ed Integrità Strutt.*, vol. 9, no. 31, pp. 127–137, Dec. 2014, doi: 10.3221/IGF-ESIS.31.10.
- [114] N. A. Smith, G. G. Antoun, A. B. Ellis, and W. C. Crone, "Improved adhesion between nickel–titanium shape memory alloy and a polymer matrix via silane coupling agents," *Compos. Part Appl. Sci. Manuf.*, vol. 35, no. 11, pp. 1307–1312, Nov. 2004, doi: 10.1016/j.compositesa.2004.03.025.
- [115] S. Rossi, F. Deflorian, A. Pegoretti, D. D’Orazio, and S. Gialanella, "Chemical and mechanical treatments to improve the surface properties of shape memory NiTi wires," *Surf. Coat. Technol.*, vol. 202, no. 10, pp. 2214–2222, Feb. 2008, doi: 10.1016/j.surfcoat.2007.09.013.
- [116] Z. Wang, Y. Liu, H. Lv, and B. Yang, "Enhancement of interface performance between shape memory alloy fiber and polymer matrix using silane coupling agent KH550 and Al₂O₃ nanoparticles," *Polym. Compos.*, vol. 39, no. 9, pp. 3040–3047, Sep. 2018, doi: 10.1002/pc.24308.
- [117] S. Samal *et al.*, "Study of Interfacial Adhesion between Nickel-Titanium Shape Memory Alloy and a Polymer Matrix by Laser Surface Pattern," *Appl. Sci.*, vol. 10, no. 6, p. 2172, Mar. 2020, doi: 10.3390/app10062172.

- [118] B. Gabry, F. Thiebaud, and C. LExcellent, "Topographic Study of Shape Memory Alloy Wires Used as Actuators in Smart Materials," *J. Intell. Mater. Syst. Struct.*, vol. 11, no. 8, pp. 592–603, Aug. 2000, doi: 10.1106/XA96-8NV4-DBQ1-2C8G.
- [119] H. C. Man and N. Q. Zhao, "Enhancing the adhesive bonding strength of NiTi shape memory alloys by laser gas nitriding and selective etching," *Appl. Surf. Sci.*, vol. 253, no. 3, pp. 1595–1600, Nov. 2006, doi: 10.1016/j.apusc.2006.02.057.
- [120] B. K. Jang and T. Kishi, "Adhesive strength between TiNi fibers embedded in CFRP composites," *Mater. Lett.*, vol. 59, no. 11, pp. 1338–1341, May 2005, doi: 10.1016/j.matlet.2005.01.006.
- [121] V. Murkute, A. Gupta, D. G. Thakur, R. Harshe, and M. Joshi, "Improvisation of Interfacial Bond Strength in Shape Memory Alloy Hybrid Polymer Matrix Composites," *Procedia Mater. Sci.*, vol. 6, pp. 316–321, 2014, doi: 10.1016/j.mspro.2014.07.040.
- [122] L. Zhao, X. Feng, X. Mi, Y. Li, H. Xie, and X. Yin, "The interfacial strength improvement of SMA composite using ZnO with electrochemical deposition method," *Appl. Surf. Sci.*, vol. 320, pp. 670–673, Nov. 2014, doi: 10.1016/j.apusc.2014.09.125.
- [123] Y. Zhang and C. Mi, "Strengthening bonding strength in NiTi SMA fiber-reinforced polymer composites through acid immersion and Nanosilica coating," *Compos. Struct.*, vol. 239, p. 112001, May 2020, doi: 10.1016/j.compstruct.2020.112001.
- [124] A. Nagaoka, K. Yokoyama, and J. Sakai, "Evaluation of hydrogen absorption behaviour during acid etching for surface modification of commercial pure Ti, Ti–6Al–4V and Ni–Ti superelastic alloys," *Corros. Sci.*, vol. 52, no. 4, pp. 1130–1138, Apr. 2010, doi: 10.1016/j.corsci.2009.12.029.
- [125] Y. L. Wang, Z. Q. Wang, L. M. Zhou, and H. T. Huang, "Influence of Silane Coupling Agent on Interfacial Strength of SMA Composite," *Adv. Mater. Res.*, vol. 143–144, pp. 933–937, Oct. 2010, doi: 10.4028/www.scientific.net/AMR.143-144.933.
- [126] Y. Payandeh, F. Meraghni, E. Patoor, and A. Eberhardt, "Debonding initiation in a NiTi shape memory wire–epoxy matrix composite. Influence of martensitic transformation," *Mater. Des.*, vol. 31, no. 3, pp. 1077–1084, Mar. 2010, doi: 10.1016/j.matdes.2009.09.048.
- [127] K. D. Jonnalagadda, N. R. Sottos, M. A. Qidwai, and D. C. Lagoudas, "In situ displacement measurements and numerical predictions of embedded SMA transformation," *Smart Mater. Struct.*, vol. 9, no. 5, pp. 701–710, Oct. 2000, doi: 10.1088/0964-1726/9/5/315.
- [128] K. J. Urschel, "Untersuchung der Grenzflächeneigenschaften von hybriden Verbundwerkstoffen auf Basis von Formgedächtnislegierungen (FGL)," I, IVW, 23–032, Jul. 2023.
- [129] C.-H. Hsueh, "Strength versus energy debonding criteria at fiber/matrix interfaces," *Compos. Eng.*, vol. 2, no. 8, pp. 665–675, Jan. 1992, doi: 10.1016/0961-9526(92)90024-Z.
- [130] A. Gapeeva *et al.*, "Electrochemical Surface Structuring for Strong SMA Wire–Polymer Interface Adhesion," p. 12, 2021.
- [131] C. Poon, L. Zhou, W. Jin, and S. Shi, "Interfacial debond of shape memory alloy composites," *Smart Mater. Struct.*, vol. 14, no. 4, pp. N29–N37, Aug. 2005, doi: 10.1088/0964-1726/14/4/N05.

- [132] L. C. Brinson, "One-dimensional constitutive behavior of shape memory alloys: Thermomechanical derivation with non-constant material functions and redefined martensite internal variable," *J. Intell. Mater. Syst. Struct.*, vol. 4, no. 2, pp. 229–242, 1993, doi: 10.1177/1045389X9300400213.
- [133] S. H. Goodman, "6 - Epoxy Resins," in *Handbook of Thermoset Plastics (Second Edition)*, S. H. Goodman, Ed., Westwood, NJ: William Andrew Publishing, 1998, pp. 193–268. doi: 10.1016/B978-081551421-3.50009-6.
- [134] J.-E. Bidaux, L. Bataillard, J.-A. Manson, and R. Gotthardt, "Phase transformation behavior of thin shape memory alloy wires embedded in a polymer matrix composite," *J. Phys. IV*, vol. 03, no. C7, pp. C7-564, Nov. 1993, doi: 10.1051/jp4:1993793.
- [135] K.-T. Lau, A. W.-L. Chan, S.-Q. Shi, and L.-M. Zhou, "Debond induced by strain recovery of an embedded NiTi wire at a NiTi/epoxy interface: micro-scale observation," p. 6, 2002.
- [136] Y. Wang, L. Zhou, Z. Wang, H. Huang, and L. Ye, "Stress distributions in single shape memory alloy fiber composites," *Mater. Des.*, vol. 32, no. 7, pp. 3783–3789, Aug. 2011, doi: 10.1016/j.matdes.2011.03.039.
- [137] E. B. Murphy, "The return of photoelastic stress measurements: utilizing birefringence to monitor damage and repair in healable materials," *J. Mater. Chem.*, vol. 21, no. 5, pp. 1438–1446, Jan. 2011, doi: 10.1039/C0JM02308F.
- [138] S. Bruns *et al.*, "On the material dependency of peri-implant morphology and stability in healing bone," *Bioact. Mater.*, vol. 28, pp. 155–166, Oct. 2023, doi: 10.1016/j.bioactmat.2023.05.006.
- [139] S. Shabalovskaya, J. Anderegg, and J. Van Humbeeck, "Critical overview of Nitinol surfaces and their modifications for medical applications," *Acta Biomater.*, vol. 4, no. 3, pp. 447–467, May 2008, doi: 10.1016/j.actbio.2008.01.013.
- [140] C. Huang, Y. Xie, L. Zhou, and H. Huang, "Enhanced surface roughness and corrosion resistance of NiTi alloy by anodization in diluted HF solution," *Smart Mater. Struct.*, vol. 18, no. 2, p. 024003, Feb. 2009, doi: 10.1088/0964-1726/18/2/024003.
- [141] S. Cattarin, P. Guerriero, M. Musiani, A. Tuissi, and L. Vázquez-Gómez, "Electrochemical Etching of NiTi Alloy in a Neutral Fluoride Solution," *J. Electrochem. Soc.*, vol. 156, no. 12, p. C428, Oct. 2009, doi: 10.1149/1.3240335.
- [142] Z. Yang, X. Wei, P. Cao, and W. Gao, "surface modification of nitinol by chemical and electrochemical etching," *Mod. Phys. Lett. B*, Jul. 2013, doi: 10.1142/S0217984913410121.
- [143] T. Mineta, Y. Haga, and M. Esashi, "Electrochemical etching of shape memory alloy using new electrolyte solutions," in *Technical Digest. MEMS 2002 IEEE International Conference. Fifteenth IEEE International Conference on Micro Electro Mechanical Systems (Cat. No.02CH37266)*, Las Vegas, NV, USA: IEEE, 2002, pp. 376–379. doi: 10.1109/MEMSYS.2002.984281.
- [144] T. Mineta and E. Makino, "Characteristics of the electrochemical etching of TiNi shape memory alloy in a LiCl–ethanol solution," *J. Micromechanics Microengineering*, vol. 20, no. 12, p. 125012, Dec. 2010, doi: 10.1088/0960-1317/20/12/125012.
- [145] R. Hang *et al.*, "Fabrication of Ni-Ti-O nanotube arrays by anodization of NiTi alloy and their potential applications," *Sci. Rep.*, vol. 4, no. 1, p. 7547, Dec. 2014, doi: 10.1038/srep07547.
- [146] L. D. Xu, X. Y. Sun, P. Wan, X. D. Sun, and Z. Q. Wang, "Surface treatment of interfacial properties of Shape Memory Alloy composites," *Mater. Res. Innov.*,

- vol. 19, no. sup5, pp. S5-734-S5-738, May 2015, doi: 10.1179/1432891714Z.0000000001184.
- [147] Huntsman Araldite® LY5052/ Aradur 5052 Datasheet <https://www.swisscomposite.ch/pdf/t-Araldite-LY5052-Aradur5052-e.pdf> (accessed Jan 13, 2021)
- [148] G. W. Ehrenstein, *Faserverbund-Kunststoffe: Werkstoffe - Verarbeitung - Eigenschaften*. Carl Hanser Verlag GmbH Co KG, 2018.
- [149] C. Li, K. Potter, M. R. Wisnom, and G. Stringer, "In-situ measurement of chemical shrinkage of MY750 epoxy resin by a novel gravimetric method," *Compos. Sci. Technol.*, vol. 64, no. 1, pp. 55–64, Jan. 2004, doi: 10.1016/S0266-3538(03)00199-4.
- [150] Memry Corporation, "Datenblatt Alloy H 1mm." Dec. 18, 2019.
- [151] M. Baytekin-Gerngross, M. D. Gerngross, J. Carstensen, and R. Adelung, "Making metal surfaces strong, resistant, and multifunctional by nanoscale-sculpturing," *Nanoscale Horiz.*, vol. 1, no. 6, pp. 467–472, Oct. 2016, doi: 10.1039/C6NH00140H.
- [152] D. C. Harris, *Lehrbuch der Quantitativen Analyse*. Berlin, Heidelberg: Springer, 2014. doi: 10.1007/978-3-642-37788-4.
- [153] M. Niinomi, *Metals for biomedical devices*. in Woodhead publishing in materials. Cambridge: Woodhead publ, 2010.
- [154] J. Carstensen, R. Prange, and H. Föll, "A Model for Current-Voltage Oscillations at the Silicon Electrode and Comparison with Experimental Results," *J. Electrochem. Soc.*, vol. 146, no. 3, pp. 1134–1140, Mar. 1999, doi: 10.1149/1.1391734.
- [155] J. Jungbluth *et al.*, "Characterization and improvement of SMA-polymer interface in active hybrid composites," presented at the International Conference on Composite Materials ICCM23, Belfast, Nordirland, 07.-04.08 2023.
- [156] M.-C. Wnuk, "Konzeptionierung, Entwicklung und Aufbau eines automatisierten Versuchsstands zur widerstandsbasierten Regelung von Formgedächtnisaktoren," Lehrstuhl für Messtechnik und Sensorik, TU Kaiserslautern, Diplomarbeit, Feb. 2017.
- [157] J. Moosmann *et al.*, "Time-lapse X-ray phase-contrast microtomography for in vivo imaging and analysis of morphogenesis," *Nat. Protoc.*, vol. 9, no. 2, Art. no. 2, Feb. 2014, doi: 10.1038/nprot.2014.033.
- [158] T. Hildebrand and P. Rügsegger, "A new method for the model-independent assessment of thickness in three-dimensional images," *J. Microsc.*, vol. 185, no. 1, pp. 67–75, Jan. 1997, doi: 10.1046/j.1365-2818.1997.1340694.x.
- [159] "Fiji," ImageJ Wiki. Accessed: Nov. 29, 2021. [Online]. Available: <https://imagej.github.io/software/fiji/index>
- [160] J. Jungbluth *et al.*, "Interface failure analysis of embedded NiTi SMA wires using in situ high-resolution X-ray synchrotron tomography," *Mater. Charact.*, p. 113345, Sep. 2023, doi: 10.1016/j.matchar.2023.113345.
- [161] C. Marotzke and L. Qiao, "Interfacial crack propagation arising in single-fiber pull-out tests," *Compos. Sci. Technol.*, vol. 57, no. 8, pp. 887–897, 1997, doi: 10.1016/S0266-3538(96)00179-0.
- [162] S. Y. Kemtchou, "Optimierung der Grenzflächenhaftung bei NiTi, PolymerVerbunden durch Einsatz funktioneller Zwischenschichten," p. 70, 2008.
- [163] J. Moosmann *et al.*, "A load frame for in situ tomography at PETRA III," in *Developments in X-Ray Tomography XII*, SPIE, Sep. 2019, pp. 252–268. doi: 10.1117/12.2530445.

-
- [164] H. Ma *et al.*, "PEEK (Polyether-ether-ketone) and its composite materials in orthopedic implantation," *Arab. J. Chem.*, vol. 14, no. 3, p. 102977, Mar. 2021, doi: 10.1016/j.arabjc.2020.102977.
- [165] H. Farid and E. P. Simoncelli, "Differentiation of Discrete Multidimensional Signals," *IEEE Trans. Image Process.*, vol. 13, no. 4, pp. 496–508, Apr. 2004, doi: 10.1109/TIP.2004.823819.
- [166] I. Arganda-Carreras *et al.*, "Trainable Weka Segmentation: a machine learning tool for microscopy pixel classification," *Bioinformatics*, vol. 33, no. 15, pp. 2424–2426, Aug. 2017, doi: 10.1093/bioinformatics/btx180.
- [167] C. A. Schneider, W. S. Rasband, and K. W. Eliceiri, "NIH Image to ImageJ: 25 years of image analysis," *Nat. Methods*, vol. 9, no. 7, Art. no. 7, Jul. 2012, doi: 10.1038/nmeth.2089.
- [168] J.-K. Kim, L.-M. Zhou, and Y.-W. Mai, "Interfacial debonding and fibre pull-out stresses: Part III Interfacial properties of cement matrix composites," *J. Mater. Sci.*, vol. 28, no. 14, pp. 3923–3930, Jul. 1993, doi: 10.1007/BF00353200.

Appendix

A.1 Reproducibility Test Selective Electrochemical Etching, for Structure B1

The reproducible analysis is already published in [130]. Three non-embedded SMA wires with the surface Structure B1 were analyzed using the 3D Laser Scanning Confocal Microscope VK-X (Keyence Corporation, Osaka, Japan). The measurement length was set the same as the SMA wire surface etch length (10 cm), segmented into five segmentation lengths of 2 cm each. One measurement point in the middle of the segmentation length was scanned in each segmented piece.

The red semiconductor laser with a wavelength of 658 nm was chosen as a light source. The roughness values Ra and Rz were measured for each ROI by averaging the conducted values for 61 lines. To analyze if there are significant differences between all tested values, the one-way ANOVA analysis followed by a Tukey test was performed. The results of the analysis are illustrated in Figure S 1. No significant difference ($p > 0.05$) could be measured, indicating a good reproducibility of the selective electrochemical etching process.

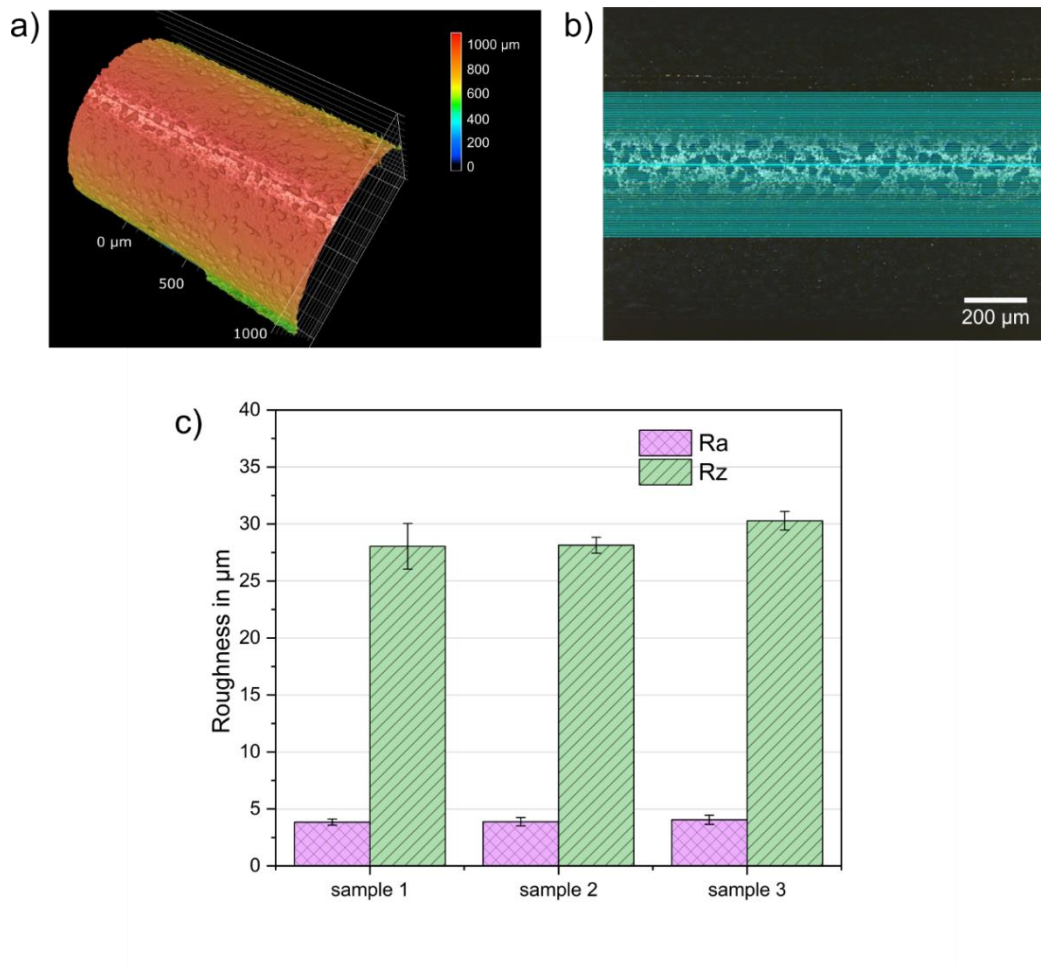


Figure S 1: Reproducibility test of the selective electrochemical etching process on the example of Structure B1 using 3D Laser Scanning Confocal Microscope: a) exemplary 3D image of one ROI, b) exemplary visualization of the multiple line scans, c) measuring results for the

three tested samples, showing the mean values (R_a and R_z) for the five ROI per samples with the calculated standard deviation. [130]

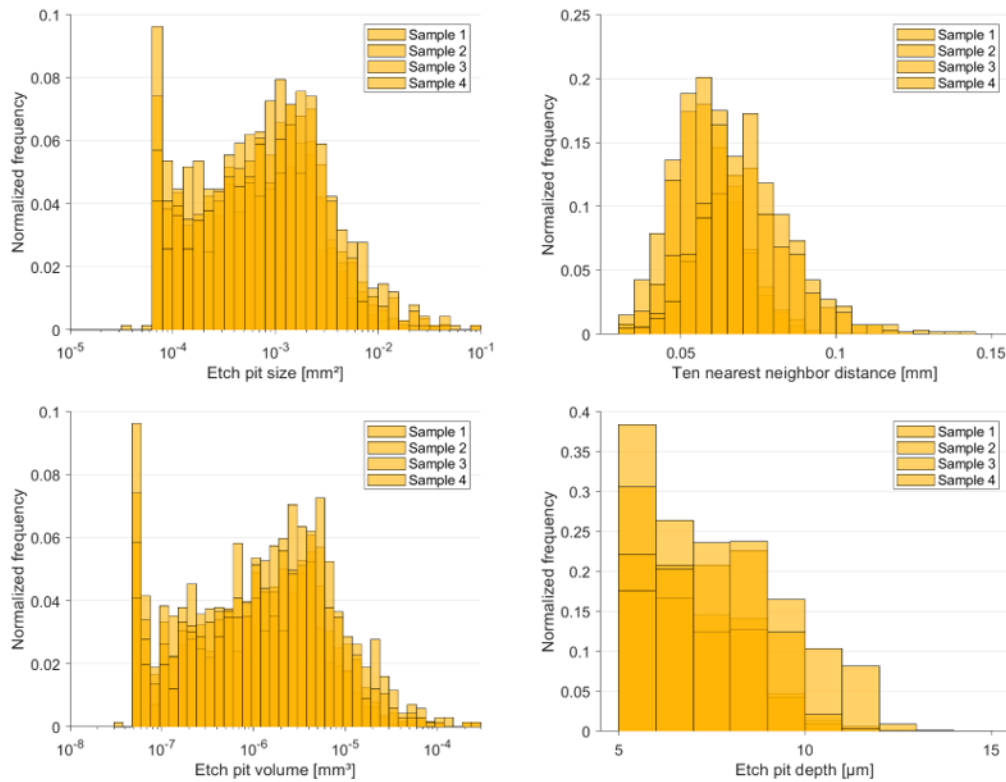


Figure S 2: Surface morphology analysis using μ CT measurement of four structured SMA wires with the same surface Structure S1

A.2 Quality Assurance Measurements

A.2.1 Pull-Out Sample Quality Control

All pull-out samples tested, the mechanical laboratory and the μ CT *in situ* pull-out test, were analyzed for sample quality. All evaluations were done optically by sight control.

Three quality assurance factors are considered:

- Alignment of the embedded SMA wire in the polymer matrix in load direction.
- Void content, especially in the interface between SMA wire and polymer matrix.
- Pre-delamination due to the manufacturing process in the SMA wire and polymer matrix interface.

A.2.2 X-ray Beam-Induced Post Curing Effects of the Polymer Matrix During μ CT Measurements

In order to determine the influence of the X-ray beam emitted by the cold curing epoxy during μ CT *in situ* pull-out test on the measurement results, DSC measurements were performed. The part of the polymer matrix that was exposed to the X-ray beam is brown-colored. Three X-ray exposed epoxy resin samples and three non-X-ray exposed samples were tested. The DSC measurement samples were cut out of different areas of the same representative μ CT *in situ* pull-out sample, which was tested with several load-increments. The DSC measurement was done with the DSC3+ (Mettler Toledo GmbH, Germany). Three heat cycles from 0-220 °C were used with a 2 K/min heating rate for each sample. The comparison of the first heat curves illustrated in Figure S 3 shows no significant change, indicating X-ray beam induced post curing.

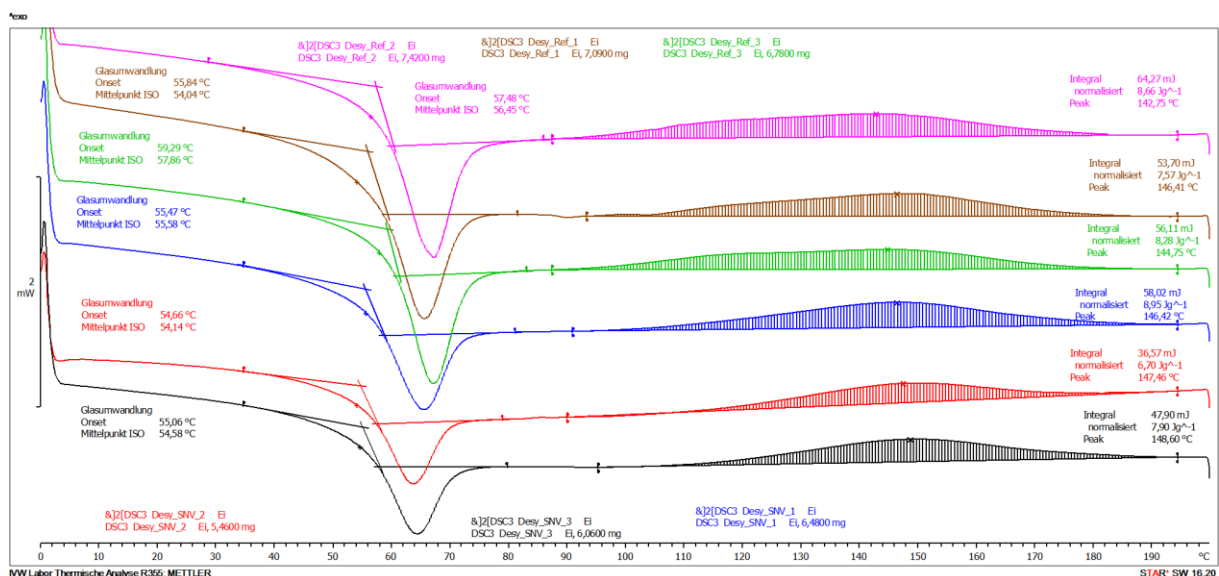


Figure S 3: DSC measurement curves of the first heating cycle for the six tested samples.

In addition, a reference test was performed in which one sample was preloaded with a specific load outside the X-ray beam, followed by a μ CT scan under load. The propagation of delamination was as expected and the interfacial failure was similar to that from the μ CT *in situ* pull-out load-increment tested sample. This test was also used to estimate how much the load-increment testing affects the interfacial failure process in compared to a linear load increase pull-out test. No difference in the interfacial failure progression due to X-ray beam-induced post-curing effects could be observed.

A.2.3 Testing the Bond Quality Between SMA Wire and Polymer Matrix by Ion-Beam Polishing of Cross-Section of a μ CT *In Situ* Pull-Out Sample

SEM imaging evaluated the bond quality between the polymer matrix and an SMA wire with a structured surface (Structure S1). For this purpose, a transverse section of a sample was prepared by ion beam polishing.

The quality of the bonding between SMA wire and polymer matrix SEM images from the cross-section of an μ CT *in situ* pull-out sample with an SMA wire (0.5 mm) with structured surface (Structure S1) were made. It was intended to verify the bond quality of the SMA wire with the surrounding matrix polymer and whether the polymer penetrates within the SMA wire surface pits. The selected μ CT *in situ* sample was cut with a diamond saw. After cutting, the sample was polished with 400 SiC sandpaper. In order to avoid damaging the interface during the polishing process, the specimen was then processed with an AR Ion Sputter system IM5000 (Hitachi, Japan). A stand over of 20 μ m was selected and an accelerating voltage of 5.5 kV. The ionization voltage was 1.5 kV, and the processing angle $\pm 30^\circ$. The polished cross section was analyzed in a SEM type SU5000. The results (Figure S 4) show a good bonding quality between SMA wire and polymer matrix, with the chosen, resolution no gap between the constituents can be found.

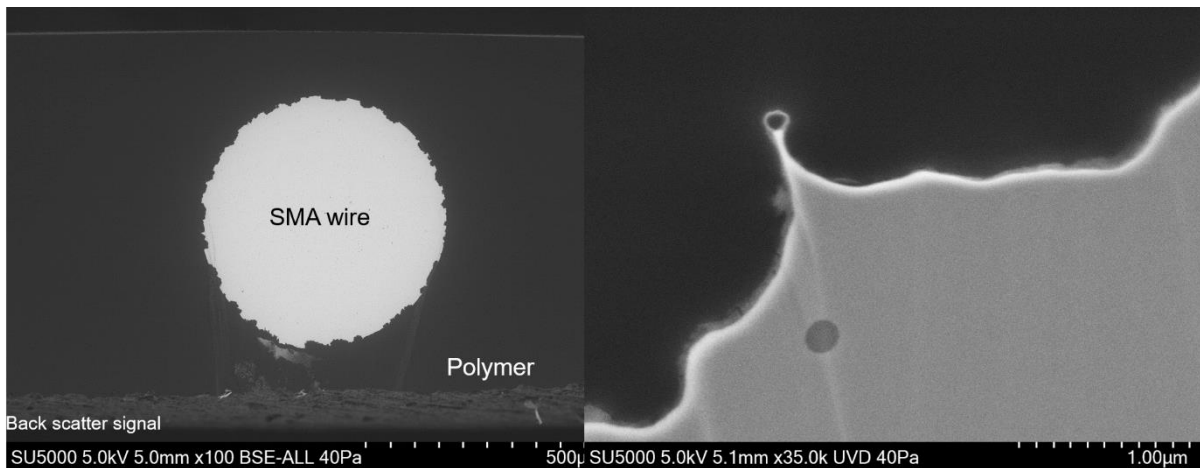


Figure S 4: Ion-beam polished cross-section of a μ CT *in situ* pull-out sample, showing a good bonding between SMA wire and polymer matrix, the SMA wire surface pits are filled with polymer matrix and no gap between the constituents can be found.

A.3 *In Situ* Pull-Out Sample Manufacturing

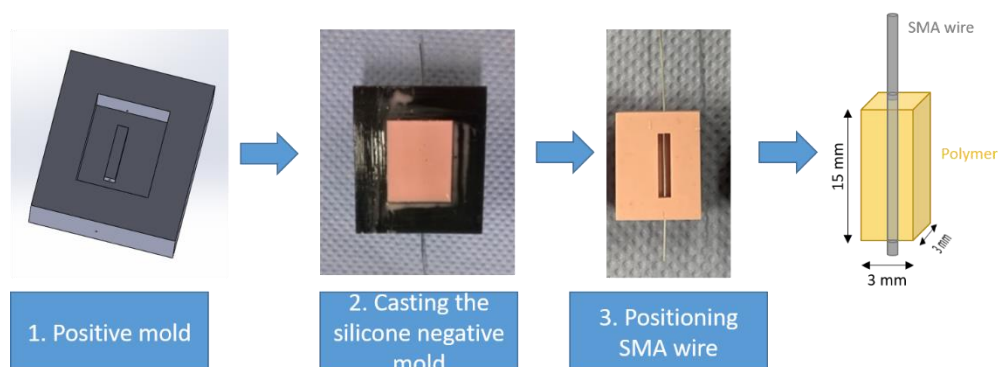


Figure S 5: Showing the *in situ* pull-out sample preparation process, starting with printing the positive mold (1), using this mold for casting a negative silicone mold (2), next step was positioning the cleaned and heat-treated SMA wire in the silicone mold the epoxy polymer matrix is filled in, after curing as described in section 2.2 a pull-out sample can be demolded as schematic demonstrated (right). [160]

A.4 Separation of SMA Wire Surface Pits (μ CT Analysis)

The analysis of the previously shown SMA wire structured surface morphology is strongly influenced by the chosen parameters for SMA wire surface pit definition. To avoid deep etch pits being considered as a single pit and thus falsify the results, the BoneJ thickness plugin in Fiji ImageJ was used. In this process, a sphere was determined for each voxel of an etch pit. In this way, all pits with a size of less than 15 voxels

were excluded (set as a minimum value for the spheres). This is visualized in Figure S 6.

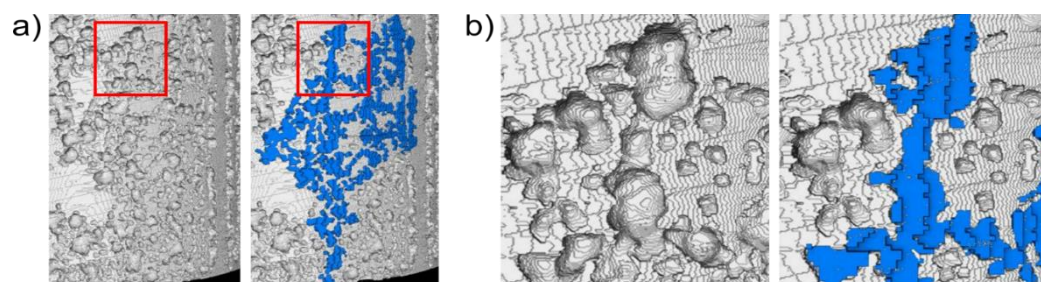


Figure S 6: Example of falsely connected SMA wire surface pits: a) overall view of the SMA wire surface (Structure B2) and the etched volume identified as a pit (in blue), b) detailed view of the area marked in red. [130]

A.5 Stepwise Increasing of Load During μ CT *In Situ* Pull-Out and Straining Test

Table S 1: Showing the load increments that were applied during the entire μ CT *in situ* pull-out experiment for every successfully tested specimen

Step	Structure S1 Sample 1	Structure S1 Sample 2	Structure S1 Sample 3	Structure S2 Sample 1	Structure S2 Sample 2	Structure S2 Sample 3
0	1 N	1 N	1.6 N	3 N	0	1 N
1	3 N	2.1 N	3.4 N	5 N	1.8 N	2 N
2	5 N	3 N	5.3 N	7.2 N	3.8 N	3 N
3	6 N	4.8 N	7 N	9.2 N	5.9 N	4.1 N
4	7 N	11 N	8.7 N	11.1 N	7.9 N	5 N
5	9 N	15 N	10.5 N	13.1 N	10.1 N	6N
6	15.2 N	20.1 N → 1.9%	12.3 N	15.1 N	11.7 N	7.1 N
7	19.1 N → 1.8 %	23 N	14.1 N	17.1 N	13.8 N → 1.9 %	8.2 N
8	24.1 N	25 N	15.9 N	19.1 N	16 N	9.1 N → 0.98 %
9	27 N	27 N	17.7 N	21.1 N → 4.7 %	17.9 N	10 N
10	29 N	29 N	19.4 N → 3.8 %	23.1 N	20 N	11 N
11	31 N	30 N	21.1 N	25.1 N	22 N	12.1 N
12	33 N	32.1 N	22.9 N	27.1 N	24 N	13 N
13	34 N	33 N	23 N	29 N	26 N	14.1 N
14	36 N	34 N	24.7 N	31.1 N	28 N	15.2 N
15	37.1 N	35 N				16.2 N
16	38 N	36.1 N				17.2 N
17		38.1 N				18.2 N
18		40 N				19.1 N
19		45 N				20.2 N
20		50 N				22.1 N

Table S 2: Showing the load increments which were applied during the entire μ CT *in situ* straining experiment for every successfully tested specimen

Step	Structure S1 Sample 1	Structure S1 Sample 2
0	0.6 N	0.1 N
1	1.7 N	2 N
2	3.3 N	4.1 N
3	5 N	6.2 N
4	6.7 N	7.2N
5	8.4 N	8.2 N
6	10.2 N	9.1 N
7	11.7 N	10.2 N
8	13.3 N	11.4 N
9	14.6 N	12.3N
10	16.7 N	14.3 N
11	16.7 N	
12	17.6 N	
13	18.4 N	
14	19.2 N	
15	20.1 N	
16	20.7 N	

A.6 Segmentation of Structure S1 μ CT *In Situ* Pull-Out Test

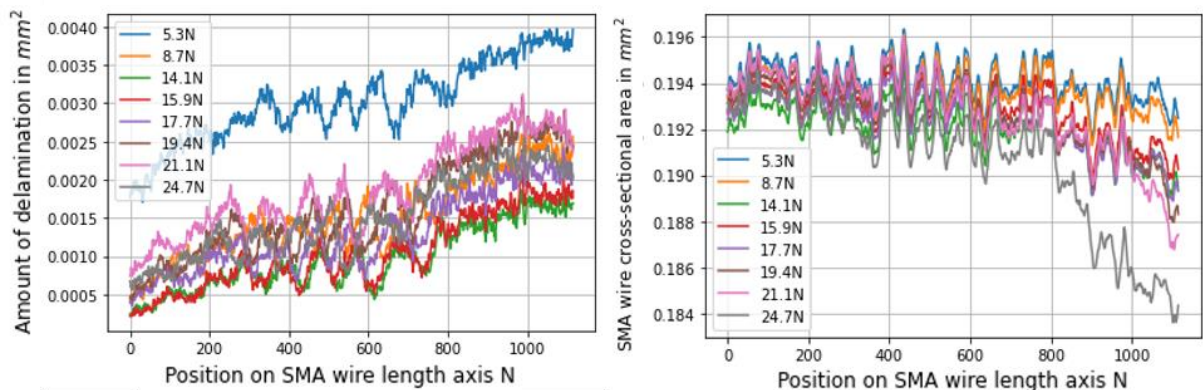


Figure S 7: Development of the amount of delamination a) and the SMA wire cross-sectional area b) for each slice through tomographic reconstruction in z-direction for the load levels, 5.3 N, 8.7 N, 14.1 N, 15.9 N, 17.7 N, 19.4 N, 21.1 N, 24.7 N and 27 N. The segmentation analysis was done for a Structure S1 pull-out sample. The SMA wire length axis position N= 1422 is denoted as the SMA wire entry point.

A.7 Comparison of the Global Axial and Radial Strain Development by Increasing Load for the *In Situ* Pull-Out and Strain Test for One Representative Sample for (Structure S1, S2 (Embedded) and Structure S1 (Non-Embedded))

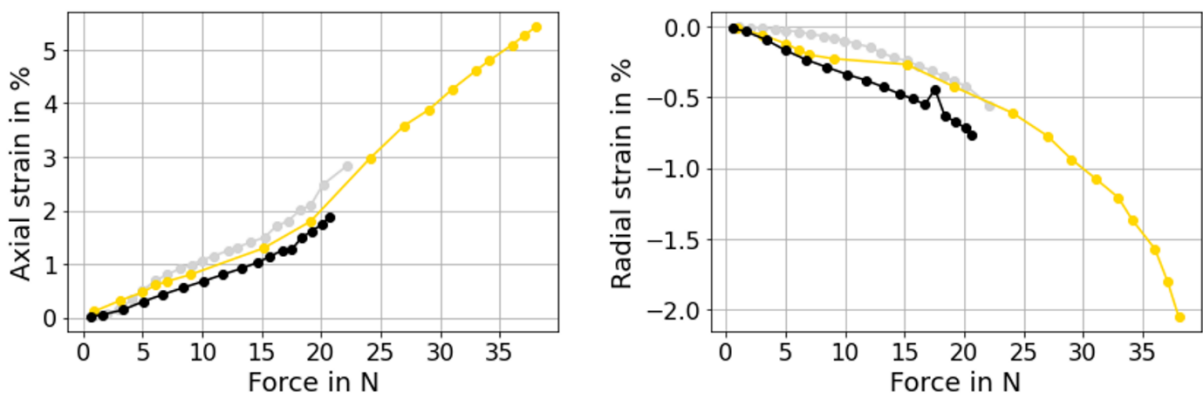


Figure S 8: Global axial (a) and radial (b) strain development of Structure S1 (yellow), Structure S2 (grey) and non-embedded Structure S1 SMA wire (black) by increasing the applied load during μ CT *in situ* pull-out or strain test.

A.8 Force-Time Curve During μ Ct *In Situ* Pull-Out Test

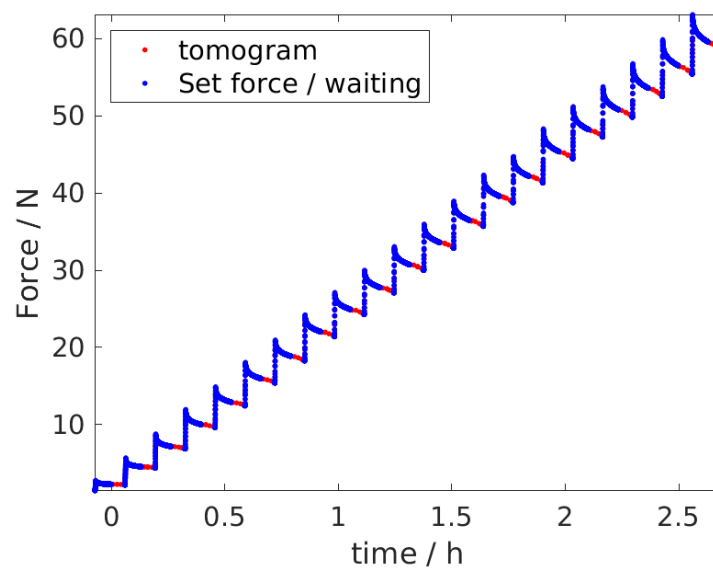


Figure S 9: Representative test procedure for one representative sample tested with the *in situ* μ CT pull-out test, showing the force drop during holding time due to settlement effects.

A.9 Values Used for Calculating the Interfacial Shear Stress

Table S 3: Values for calculating interfacial shear stress according to [50]

Symbol	Used values
F_w : Force of the first failure in the interface	As-delivered (1 mm): 38.95 N Structure B1: 126.85 N Structure B2: 125.5 N Structure B3: 119.92 N As-delivered (1 mm): 28.5 N Structure S1: 42.6 N Structure S2: 32 N
G_m : Shear modulus of the polymer matrix	1240.74 MPa
r : Radius of the SMA wire	As-delivered (1 mm): 0.5069 mm Structure B1: 0.50215 mm Structure B2: 0.5021 mm Structure B3: 0.50155 mm As-delivered (0.5 mm): 0.2500 mm Structure S1: 0.2484 mm Structure S2: 0.2476 mm
D : Radius of the surrounding polymer matrix	Mechanical laboratory: 8 mm μ CT <i>in situ</i> : 2.5 mm
E_w : Tensile modulus of the wire	12776 MPa
E_m : Tensile modulus of the polymer matrix	3350 MPa
L_e : Embedded SMA wire length	Mechanical laboratory: 50 mm μ CT <i>in situ</i> : 15 mm

A.10 Propagation of the Interfacial Failure Observed for a μ CT *In Situ* Pull-Out Tested Sample with Structure S2

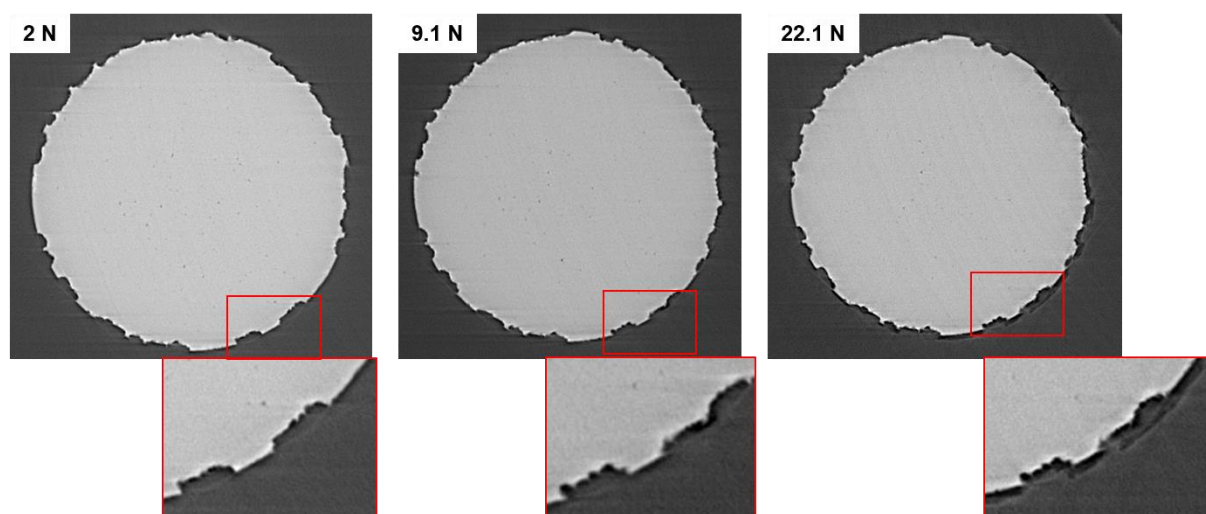


Figure S 10: Three load steps of a representative Structure S2 (0.5 mm diameter) *in situ* pull-out sample, showing the top view slice through tomographic reconstructions of the embedded SMA wire. Approx. the same z-position close to the SMA wire entry point is shown. The advancing delamination is visualized with increasing load steps. The red marked area demonstrates where the delamination starts in the circumferential direction and is therefore shown enlarged.

A.11 Influence of the Polymer Matrix Geometry to the Calculated Interfacial Shear Strength of the Pull-Out Test According to [50]

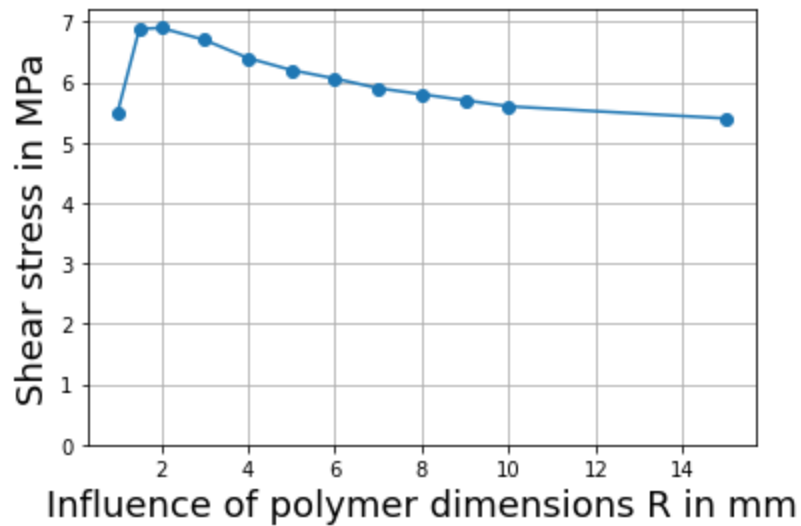


Figure S 11: Estimation of the influence of boundary effects; for this purpose, the size of the matrix is changed for the same parameters and the influence on the resulting interfacial shear stress is estimated using [50].

A.12 Pre-Strain Test Mean Values with Confidence Interval for SMA Wire with a Nominal Diameter of 1 mm

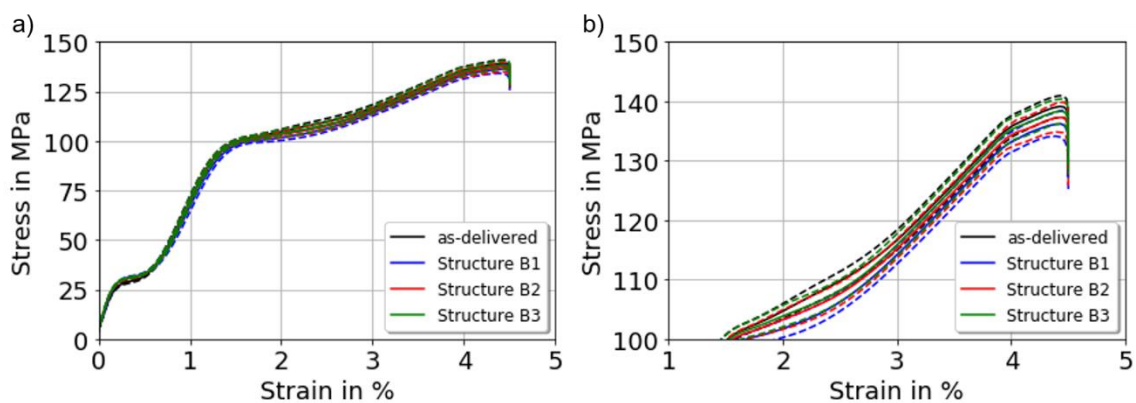


Figure S 12: Calculated mean values with 99 % confidence interval from the tensile test with the SMA wire with nominal diameter of 1 mm for the four SMA wire surface variants: a) the complete pre-strain test, b) enlargement of the relevant area.

Own Publication

Peer Review Paper

A. Gapeeva et al., "Pull-Out Testing of Electrochemically Etched NiTi Shape Memory Alloy Wires in Shape Memory Alloy Hybrid Composites", vol. *Advanced Engineering Materials*, Mar. **2024**, doi: [10.1002/adem.202301912](https://doi.org/10.1002/adem.202301912).

Jungbluth, J.; Bruns, S.; Schmidt, C.; Beckmann, F.; Moosmann, J.; Gapeeva, A.; Carstensen, J.; Adelong, R.; Zeller-Plumhoff, B.; Gurka, M. Interface Failure Analysis of Embedded NiTi SMA Wires Using in Situ High-Resolution X-Ray Synchrotron Tomography. *Materials Characterization* **2023**, *205*, 113345, doi:[10.1016/j.matchar.2023.113345](https://doi.org/10.1016/j.matchar.2023.113345).

Arweiler-Böllert, S.; Liesegang, M.; Beck, T.; Jungbluth, J.; Schmeer, S. Relation Between Interface Geometry and Tensile Shear Strength of Ultrasonically Welded Joints. **2023**, doi:[10.1007/s11665-023-08325-2](https://doi.org/10.1007/s11665-023-08325-2).

Popow, V.; Vogtmann, J.; Gurka, M. In-Situ Characterization of Impact Damage in Carbon Fiber Reinforced Polymers Using Infrared Thermography. *Infrared Physics & Technology* **2022**, *122*, 104074, doi:[10.1016/j.infrared.2022.104074](https://doi.org/10.1016/j.infrared.2022.104074).

Gapeeva, A.; Vogtmann, J.; Zeller-Plumhoff, B.; Beckmann, F.; Gurka, M.; Carstensen, J.; Adelong, R. Electrochemical Surface Structuring for Strong SMA Wire–Polymer Interface Adhesion. **2021**, *12*.

Vogtmann, J.; Klingler, A.; Rief, T.; Gurka, M. 3D X-Ray Microscopy as a Tool for in Depth Analysis of the Interfacial Interaction between a Single Carbon Fiber and an Epoxy Matrix after Mechanical Loading. *J. Compos. Sci.* **2021**, *5*, 121, doi:[10.3390/jcs5050121](https://doi.org/10.3390/jcs5050121).

Conference Paper

M. Gurka, "In-situ synchrotron CT measurements on the Interface between shape memory alloy wire and polymer matrix in hybrid composites under tensile loading," presented at the SPIE Optics & Photonics, San Diego, California, USA, Aug. 2024.

Jungbluth geb. Vogtmann, J.; Schmidt, C.; Gapeeva, A.; Bruns, S.; Beckmann, F.; Moosmann, J.; Zeller-Plum-Hoff, B.; Carstensen, J.; Adelung, R.; Gurka, M. twenty third international conference on composite materials (ICCM23) characterization and improvement of SMA-polymer interface in active hybrid composites.

Yadjjian Harutyun; Vogtmann, J.; Gurka, M. Development of a New Methodology for Automated Quantification of Impact Induced Damage Pattern in CFRP Measured by IRT and X-Ray Radiography.; Lausanne, 30.06 2022.

Kelkel, B.; Vogtmann, J.; Gurka, M. The Influence of Source Depth and Source-to-Sensor Distance on the AE Signal Characteristics of Damaging Events in Thin-Walled CFRP Laminates. 12.

Talks:

In-situ interface characterization of SMA polymer composites, Seminar talk given at TU Delft, 2023

In-situ interface characterization of SMA polymer composites, IVW Colloquium 2023
Development of a new methodology for automated quantification of impact induced damage pattern in CFRP measured by NDT methods, ECCM 2022

3D structural analysis of polymeric composite materials, 7th ZEISS X-Ray Microscopy European Network User Workshop, 30. Oktober 2019, Oberkochen

Student Thesis

1. Benedikt Fols: *Konzeptionierung und Konstruktion einer modularen Prüfmethode zur Charakterisierung von Formgedächtnislegierungen*, IVW Bericht 19-060, Leibniz Institut für Verbundwerkstoffe GmbH, Kaiserslautern, Studienarbeit 2019
2. Michael Young Lee: *Numerische Charakterisierung des Auszugsverhaltens von in Epoxidharz eingebetteten Stahl-Drähten*, IVW Bericht 21-048, Leibniz Institut für Verbundwerkstoffe GmbH, Kaiserslautern, Projektarbeit 2021
3. Paul Bitz: *Ausarbeitung einer Prüfmethode zur Durchführung von zyklischen Grenzflächenuntersuchungen an Hybrid-Verbunden*, IVW Bericht 22-020, Leibniz Institut für Verbundwerkstoffe GmbH, Kaiserslautern, Bachelorarbeit 2022
4. Moritz Wagner: *Bestimmung der Normalkraft zwischen Formgedächtnislegierung und Polymer für funktionale Hybridverbunde*, IVW Bericht 22-006, Leibniz Institut für Verbundwerkstoffe GmbH, Kaiserslautern, Bachelorarbeit 2022
5. Joelle Noumi: *Entwicklung einer Probengeometrie für die makroskopische, dynamische Analyse der Grenzfläche zwischen Stahlfasern und Polymer*, IVW Bericht 23-001, Leibniz Institut für Verbundwerkstoffe GmbH, Kaiserslautern, Projektarbeit 2022
6. Jonas Turos: *Steigerung des Leichtbaupotentials von carbonfaserverstärkten Kunststoffen durch z-Verstärkungen*, Bericht 23- , Leibniz Institut für Verbundwerkstoffe GmbH, Kaiserslautern, Bachelorarbeit 2023 –in Bearbeitung

Curriculum Vitae

Julia Jungbluth

Practical Experience

12/2018 - today	PhD Student at Leibniz-institute for composite materials GmbH
05/2016 - 09/2016	ZF Friedrichshafen AG, Friedrichshafen Mandatory internship in the field of research and development
4/2015 – 10/2018	Chair of Materials Science at the RPTU Scientific assistant

Academic career

10/2011 - 10/2018	Diploma in Mechanical and Process Engineering Technical University of Kaiserslautern
08/2002 - 06/2011	Abitur Albert-Einstein-Gymnasium Böblingen

University work

04/2018 - 10/2018	Diplom thesis at Leibniz institute for composite materials GmbH Investigation of the adhesion promoting effect of organofunctional silanes on innovative glass fibre reinforced polyurea/polysilicate resins.
05/2017 - 03/2018	Student research thesis at institute for composite materials GmbH Investigation of the influence of the source depth on characteristics of the resulting acoustic signal in aluminium and unidirectional CFRP sheets.

10/2015 - 05/2017

Student research thesis at chair of Materials Science at the RPTU

Characterisation of quasi-static material properties of aluminium matrix composites.